



## ATLAS Note

GROUP-2017-XX

6th May 2021



1

# A Deep Learning Approach to Differential Measurements of $t\bar{t}H$ Production in Multilepton Final States

2

3

4

5 The ATLAS Collaboration

6

7

8

9

10

11

12

13

The possibility of performing differential measurements of  $t\bar{t}H$  events with multiple leptons in the final state is investigated. Because of the challenges inherent to reconstructing the Higgs in multilepton final states, a deep learning approach is used to reconstruct the momentum spectrum of the Higgs, which would be altered by the presence of new physics without affecting the overall rate of  $t\bar{t}H$  production. Preliminary results using  $79.8 \text{ fb}^{-1}$ , as well as projected results for  $139 \text{ fb}^{-1}$ , at  $\sqrt{s} = 13 \text{ TeV}$  are presented, providing estimates of the sensitivity to variations in the Higgs  $p_T$  spectrum in this channel.

14 © 2021 CERN for the benefit of the ATLAS Collaboration.

15 Reproduction of this article or parts of it is allowed as specified in the CC-BY-4.0 license.

---

## 16 **Contents**

17	<b>1 Changes and outstanding items</b>	<b>4</b>
18	1.1 Changelog	4
19	<b>2 Introduction</b>	<b>5</b>
20	<b>3 Data and Monte Carlo Samples</b>	<b>6</b>
21	3.1 Data Samples	6
22	3.2 Monte Carlo Samples	6
23	<b>4 Object Reconstruction</b>	<b>9</b>
24	4.1 Trigger Requirements	9
25	4.2 Light Leptons	10
26	4.3 Jets	11
27	4.4 B-tagged Jets	11
28	4.5 Missing Transverse Energy	11
29	4.6 Overlap removal	11
30	<b>5 Higgs Momentum Reconstruction</b>	<b>12</b>
31	5.1 Physics Object Truth Matching	13
32	5.2 Truth Level Studies	13
33	5.3 b-jet Identification	13
34	5.4 Higgs Reconstruction	20
35	5.5 $p_T$ Prediction	31
36	5.6 3l Decay Mode	37
37	<b>6 Signal Region Definitions</b>	<b>39</b>
38	6.1 Pre-MVA Event Selection	39
39	6.2 Event MVA	43
40	6.3 Signal Region Definitions	47
41	<b>7 Systematic Uncertainties</b>	<b>50</b>
42	<b>8 Results</b>	<b>55</b>
43	8.1 Results - $79.8 \text{ fb}^{-1}$	56
44	8.2 Projected Results - $139 \text{ fb}^{-1}$	60
45	<b>9 Conclusion</b>	<b>64</b>
46	<b>I Appendices</b>	<b>68</b>

47	<b>Appendices</b>	<b>68</b>
48	<b>A Non-prompt lepton MVA</b>	<b>68</b>
49	<b>B Machine Learning Models</b>	<b>70</b>
50	B.1 Higgs Reconstruction Model Details	70
51	B.2 Background Rejection MVA Details	93
52	B.3 Truth Level Studies	102
53	B.4 Alternate b-jet Identification Algorithm	103
54	B.5 Binary Classification of the Higgs $p_T$	104
55	B.6 Impact of Alternative Jet Selection	105

<sup>56</sup> **1 Changes and outstanding items**

<sup>57</sup> **1.1 Changelog**

<sup>58</sup> This is version 1

## 59 2 Introduction

60 Since the discovery of a Higgs boson compatible with the Standard Model (SM) in 2012 [1], its  
 61 interactions with other particles have been studied using proton-proton collision data produced by  
 62 the Large Hadron Collider (LHC). The strongest of these interactions is the coupling of the Higgs  
 63 to the top quark, making the Yukawa coupling between these two particles of particular interest  
 64 for study.

65 These interactions can be measured directly by studying the production of a Higgs Boson in  
 66 association with a pair of Top Quarks ( $t\bar{t}H$ ). While this process has been observed by both the  
 67 ATLAS and CMS collaborations, these analyses have focused on measuring the overall rate of  $t\bar{t}H$   
 68 production. There are several theories of physics Beyond the Standard Model (BSM), however,  
 69 that would affect the kinematics involved in  $t\bar{t}H$  production without altering its overall rate [2].

70 An Effective Field Theory approach can be used to model the low energy effects of new, high  
 71 energy physics, by parameterizing BSM effects as dimension-six operators. The addition of these  
 72 operators can be shown to modify the transverse momentum ( $p_T$ ) spectrum of the Higgs Boson  
 73 [3]. Therefore, reconstructing the momentum spectrum of the Higgs provides a means to observe  
 74 new physics in the Higgs sector.

75 This note reports on the feasibility of performing differential measurements in  $t\bar{t}H$  events with  
 76 multiple leptons in the final state, using Monte Carlo (MC) simulations scaled to  $139 \text{ fb}^{-1}$  at an  
 77 energy  $\sqrt{s} = 13 \text{ TeV}$ . Events are separated into channels based on the number of light leptons  
 78 (electrons and muons) in the final state - either two same-sign leptons (2lSS), or three leptons  
 79 (3l), where the 3l channel is split into two based on the decay of the Higgs.

80 The presence of multiple neutrinos in the final state of the multilepton channels introduces an  
 81 ambiguity that prevents the Higgs from being fully reconstructed. This motivates the use of  
 82 sophisticated machine learning techniques to better predict the Higgs  $p_T$  spectrum for these events.  
 83 A deep neural network is used to identify which objects originate from the decay of the Higgs,  
 84 and reconstruct the momentum of the Higgs Boson in each event. This spectrum is fit to data in  
 85 the three decay channels considered in order to extract normalization factors on  $t\bar{t}H$  produced  
 86 with high  $p_T$  ( $> 150 \text{ GeV}$ ) and low  $p_T$  ( $< 150 \text{ GeV}$ ) Higgs.

87 This note is organized as follows: The dataset and Monte Carlo (MC) simulations used in the  
 88 analysis is outlined in Section 3. Section 4 describes the identification and reconstruction of the  
 89 various physics objects. The models used to reconstruct the momentum spectrum of the Higgs  
 90 is discussed in Section 5. The selection and categorisation of events comprises Section 6, and  
 91 the theoretical and experimental systematic uncertainties considered are described in Section 7.  
 92 Finally, the results of the study are summarized in Section 8.

### 93    3 Data and Monte Carlo Samples

94    For both data and Monte Carlo (MC) simulations, samples were prepared in the xAOD format,  
 95    which was used to produce a xAOD based on the HIGG8D1 derivation framework. This framework  
 96    was designed for the main  $t\bar{t}H$  multi-lepton analysis. Because this analysis targets events with  
 97    multiple light leptons, as well as tau hadrons, this framework skims the dataset of any events that  
 98    do not meet at least one of the following requirements:

- 99       • at least two light leptons within a range  $|\eta| < 2.6$ , with leading lepton  $p_T > 15$  GeV and  
 100      subleading lepton  $p_T > 5$  GeV
- 101      • at least one light lepton with  $p_T > 15$  GeV within a range  $|\eta| < 2.6$ , and at least two hadronic  
 102      taus with  $p_T > 15$  GeV.

103    Samples were then generated from these HIGG8D1 derivations using AnalysisBase version  
 104    21.2.127. A ptag of p4133 was used for MC samples, and p4134 for data.

#### 105    3.1 Data Samples

106    The study uses proton-proton collision data collected by the ATLAS detector from 2015 through  
 107    2018, which represents an integrated luminosity of  $139 \text{ fb}^{-1}$  and an energy of  $\sqrt{s} = 13 \text{ TeV}$ . All  
 108    data used in this analysis was included in one of the following Good Run Lists:

- 109       • data15\_13TeV.periodAllYear\_DetStatus-v79-repro20-02\_DQDefects-00-02-02  
 110       \_PHYS\_StandardGRL\_All\_Good\_25ns.xml
- 111       • data16\_13TeV.periodAllYear\_DetStatus-v88-pro20-21\_DQDefects-00-02-04  
 112       \_PHYS\_StandardGRL\_All\_Good\_25ns.xml
- 113       • data17\_13TeV.periodAllYear\_DetStatus-v97-pro21-13\_Unknown\_PHYS\_StandardGRL  
 114       \_All\_Good\_25ns\_Triggerno17e33prim.xml
- 115       • data18\_13TeV.periodAllYear\_DetStatus-v102-pro22-04\_Unknown\_PHYS\_StandardGRL  
 116       \_All\_Good\_25ns\_Triggerno17e33prim.xml

#### 117    3.2 Monte Carlo Samples

118    Several Monte Carlo (MC) generators were used to simulate both signal and background processes.  
 119    For all of these, the effects of the ATLAS detector are simulated in Geant4. The specific event  
 120    generator used for each of these MC samples is listed in Table 1. A Higgs mass of 125 GeV is  
 121    assumed in all simulations.

Table 1: The configurations used for event generation of signal and background processes, including the event generator, matrix element (ME) order, parton shower algorithm, and parton distribution function (PDF).

Process	Event generator	ME order	Parton Shower	PDF
t <small>b</small> H	MG5_AMC (MG5_AMC)	NLO (NLO)	PYTHIA 8 (HERWIG++)	NNPDF 3.0 NLO [4] (CT10 [5])
t <small>b</small> W	MG5_AMC (SHERPA 2.1.1)	NLO (LO multileg)	PYTHIA 8 (SHERPA)	NNPDF 3.0 NLO (NNPDF 3.0 NLO)
t <small>b</small> (Z/ $\gamma^*$ → ll)	MG5_AMC	NLO	PYTHIA 8	NNPDF 3.0 NLO
VV	SHERPA 2.2.2	MEPS NLO	SHERPA	CT10
t <small>b</small>	POWHEG-BOX v2 [6]	NLO	PYTHIA 8	NNPDF 3.0 NLO
t <small>b</small> $\gamma$	MG5_AMC	LO	PYTHIA 8	NNPDF 2.3 LO
tZ	MG5_AMC	LO	PYTHIA 6	CTEQ6L1
tHqb	MG5_AMC	LO	PYTHIA 8	CT10
tHW	MG5_AMC (SHERPA 2.1.1)	NLO (LO multileg)	HERWIG++ (SHERPA)	CT10 (NNPDF 3.0 NLO)
tWZ	MG5_AMC	NLO	PYTHIA 8	NNPDF 2.3 LO
t <small>b</small> t, t <small>b</small> t <small>b</small>	MG5_AMC	LO	PYTHIA 8	NNPDF 2.3 LO
t <small>b</small> W <sup>+</sup> W <sup>-</sup>	MG5_AMC	LO	PYTHIA 8	NNPDF 2.3 LO
s-, t-channel, Wt single top	POWHEG-BOX v1 [7]	NLO	PYTHIA 6	CT10
qqVV, VVV				
Z → l <sup>+</sup> l <sup>-</sup>	SHERPA 2.2.1	MEPS NLO	SHERPA	NNPDF 3.0 NLO

122 The signal sample ( $t\bar{t}H$ ) is modelled at NLO with Powheg-Box v2 using the NNPDF2.0 parton  
 123 distribution function (PDF) [8]. Parton showering and hadronisation were modelled with Pythia  
 124 8.2 [9]. The  $t\bar{t}H$  sample is normalized to a cross-section of  $507^{+35}_{-50}$  fb based on NLO calculations.  
 125 Uncertainties are based on varying the QCD factorisation and renormalisation scale, as well as  
 126 uncertainties in the PDF and  $\alpha_s$ .

127 The  $t\bar{t}W$  background is simulated using Sherpa 2.2.1 with the NNPDF3.0 NLO PDF. The matrix  
 128 element is calculated with up to one additional parton at NLO, and up to two at LO. As explained  
 129 in detail in [10], the  $t\bar{t}W$  contribution predicted by MC is found disagree significantly with  
 130 what is observed in data. While an effort is currently being undertaken to measure  $t\bar{t}W$  more  
 131 accurately, the approach used by the  $79.8 \text{ fb}^{-1}$   $t\bar{t}H$  analysis is used here: A normalization  
 132 factor of 1.68 is applied to the MC estimate of  $t\bar{t}W$  and additional systematic uncertainties on  
 133  $t\bar{t}W$  are included to account for this modelling discrepancy, as outlined in Section 7.

134 The  $t\bar{t}(Z/\gamma^*)$  process is simulated with the MADGRAPH5\_AMC@NLO generator, using NNPDF3.0.  
 135 Diboson processes are generated with SHERPA 2.2.2 at NLO precision for one extra parton, and at  
 136 LO for up to three extra partons.

137 The estimation of the “fake” or non-prompt background - with leptons from hadron decays or  
138 photon conversions - is done primarily using an inclusive  $t\bar{t}$  sample. This sample is generated  
139 using POWHEG, with PYTHIA8 performing the parton shower and fragmentation.

140 While the main  $t\bar{t}H$  analysis is currently refining a data-driven approach for estimating the contribution  
141 of events with non-prompt leptons, at the time of this note this strategy has not been completely developed for the full Run-2 dataset. Therefore, the non-prompt contribution  
142 is estimated with MC, while applying normalization corrections and systematic uncertainties  
143 derived from data driven techniques developed for the  $79.8 \text{ fb}^{-1} t\bar{t}H/t\bar{t}W$  analysis [10]. The primary contribution to the non-prompt lepton background is from  $t\bar{t}$  production, with V+jets  
144 and single-top as much smaller sources. Likelihood fits over several control regions enriched with  
145 these non-prompt backgrounds are fit to data in order to derive normalization factors for these  
146 backgrounds. The specific normalization factors and uncertainties applied to the non-prompt  
147 contributions are listed in Section 7.  
148

149  
150 Other background processes, such as  $tH$ ,  $tZ$ ,  $t\bar{t}WW$  and  $t\bar{t}t\bar{t}$ , are expected to make minor  
151 contributions to the total background. The generators and setting used for these backgrounds are  
152 summarized in Table ??.

153 The specific DSIDs used in the analysis are listed below:

Sample	DSID
tH	345873-5, 346343-5
VV	364250-364254, 364255, 363355-60, 364890
tW	413008
tZ	410156, 410157, 410218-20
low mass tZ	410276-8
Rare Top	410397, 410398, 410399
single Top	410658-9, 410644-5
three Top	304014
four Top	410080
tWW	410081
Z + jets	364100-41
low mass Z + jets	364198-215
W + jets	364156-97
V $\gamma$	364500-35
tZ	410560
tW	410013-4
WtZ	410408
VVV	364242-9
VH	342284-5
WtH	341998
t $\bar{t}\gamma$	410389
t $\bar{t}$	410470

Table 2: List of Monte Carlo samples by data set ID used in the analysis.

## 154 4 Object Reconstruction

155 All analysis channels considered in this note share a common object selection for leptons and jets,  
 156 as well as a shared trigger selection.

### 157 4.1 Trigger Requirements

158 Events are required to be selected by dilepton triggers, as summarized in Table 3.

Dilepton triggers (2015)	
$\mu\mu$ (asymm.)	HLT_mu18_mu8noL1
$ee$ (symm.)	HLT_2e12_lhloose_L12EM10VH
$e\mu, \mu e$ ( $\sim$ symm.)	HLT_e17_lhloose_mu14
Dilepton triggers (2016)	
$\mu\mu$ (asymm.)	HLT_mu22_mu8noL1
$ee$ (symm.)	HLT_2e17_lhvloose_nod0
$e\mu, \mu e$ ( $\sim$ symm.)	HLT_e17_lhloose_nod0_mu14
Dilepton triggers (2017)	
$\mu\mu$ (asymm.)	HLT_mu22_mu8noL1
$ee$ (symm.)	HLT_2e24_lhvloose_nod0
$e\mu, \mu e$ ( $\sim$ symm.)	HLT_e17_lhloose_nod0_mu14
Dilepton triggers (2018)	
$\mu\mu$ (asymm.)	HLT_mu22_mu8noL1
$ee$ (symm.)	HLT_2e24_lhvloose_nod0
$e\mu, \mu e$ ( $\sim$ symm.)	HLT_e17_lhloose_nod0_mu14

Table 3: List of lowest  $p_T$ -threshold, un-prescaled dilepton triggers used for 2015–2018 data taking.

## 4.2 Light Leptons

Electron candidates are reconstructed from energy clusters in the electromagnetic calorimeter that are associated with charged particle tracks reconstructed in the inner detector [11]. Electron candidates are required to have  $p_T > 10$  GeV and  $|\eta_{\text{cluster}}| < 2.47$ . Candidates in the transition region between different electromagnetic calorimeter components,  $1.37 < |\eta_{\text{cluster}}| < 1.52$ , are rejected. A multivariate likelihood discriminant combining shower shape and track information is used to distinguish prompt electrons from nonprompt leptons, such as those originating from hadronic showers. Electron candidate are also required to pass TightLH identification.

To further reduce the non-prompt contribution, the track of each electron is required to originate from the primary vertex; requirements are imposed on the transverse impact parameter significance ( $|d_0|/\sigma_{d_0}$ ) and the longitudinal impact parameter ( $|\Delta z_0 \sin \theta_\ell|$ ).

Muon candidates are reconstructed by combining inner detector tracks with track segments or full tracks in the muon spectrometer [12]. Muon candidates are required to have  $p_T > 10$  GeV and  $|\eta| < 2.5$ . Muons are required to Medium ID requirements.

All leptons are required to pass a non-prompt BDT selection developed by the main  $t\bar{t}H/t\bar{t}W$  analysis, described in detail in [10]. Optimized working points and scale factors for this BDT are taken from that analysis. This BDT and the WPs used are summarized in Appendix A,

---

176 **4.3 Jets**

177 Jets are reconstructed from calibrated topological clusters built from energy deposits in the  
178 calorimeters [13], using the anti- $k_t$  algorithm with a radius parameter  $R = 0.4$ . Particle Flow, or  
179 PFlow, jets are used in the analysis, which are hadronic objects reconstructed using information  
180 from both the tracker and the calorimeter. Jets with energy contributions likely arising from noise  
181 or detector effects are removed from consideration [14], and only jets satisfying  $p_T > 25$  GeV  
182 and  $|\eta| < 2.5$  are used in this analysis. For jets with  $p_T < 60$  GeV and  $|\eta| < 2.4$ , a jet-track  
183 association algorithm is used to confirm that the jet originates from the selected primary vertex,  
184 in order to reject jets arising from pileup collisions [15].

185 **4.4 B-tagged Jets**

186 Each analysis channel used in this analysis includes b-jets in the final state. These are identified  
187 using the DL1r b-tagging algorithm, which uses jet vertex and kinematic information to distinguish  
188 heavy and light flavored jets. These features are used as inputs to a neural network, the output  
189 of which is used to form calibrated working points (WPs) based on how likely a jet is to have  
190 originated from a b-quark. This analysis uses the 70% DL1r WP - implying an efficiency of 70%  
191 for truth b-jets - for selecting b-tagged jets.

192 **4.5 Missing Transverse Energy**

193 Because all  $t\bar{t}H - ML$  channels considered include multiple neutrinos, missing transverse energy  
194 ( $E_T^{\text{miss}}$ ) is present in each event. The missing transverse momentum vector is defined as the  
195 inverse of the sum of the transverse momenta of all reconstructed physics objects as well as  
196 remaining unclustered energy, the latter of which is estimated from low- $p_T$  tracks associated with  
197 the primary vertex but not assigned to a hard object [16].

198 **4.6 Overlap removal**

199 To avoid double counting objects and remove leptons originating from decays of hadrons, overlap  
200 removal is performed in the following order: any electron candidate within  $\Delta R = 0.1$  of another  
201 electron candidate with higher  $p_T$  is removed; any electron candidate within  $\Delta R = 0.1$  of a muon  
202 candidate is removed; any jet within  $\Delta R = 0.3$  of an electron candidate is removed; if a muon  
203 candidate and a jet lie within  $\Delta R = \min(0.4, 0.04 + 10[\text{GeV}] / p_T(\text{muon}))$  of each other, the jet  
204 is kept and the muon is removed.

205 This algorithm is applied to the preselected objects. The overlap removal procedure is summarized  
206 in Table 4.

<b>Keep</b>	<b>Remove</b>	<b>Cone size (<math>\Delta R</math>)</b>
electron	electron (low $p_T$ )	0.1
muon	electron	0.1
electron	jet	0.3
jet	muon	$\min(0.4, 0.04 + 10[\text{GeV}]/p_T(\text{muon}))$
electron	tau	0.2

Table 4: Summary of the overlap removal procedure between electrons, muons, and jets.

## 207 5 Higgs Momentum Reconstruction

208 Reconstructing the momentum of the Higgs boson is a particular challenge for channels with  
 209 leptons in the final state: Because all channels include at least two neutrinos in the final state, the  
 210 Higgs can never be fully reconstructed. However, the momentum spectrum can be well predicted  
 211 by a neural network when provided with the kinematics of the Higgs Boson decay products - as  
 212 verified by studies detailed in Appendix B.3. With this in mind, several layers of MVAs are used  
 213 to reconstruction the Higgs momentum:

214 The first layer is a model designed to select which jets are most likely to be the b-jets that came  
 215 from the top decay, detailed in Section 5.3. As described in Section 5.4, the kinematics of these jets  
 216 and possible Higgs decay products are fed into the second layer, which is designed to identify the  
 217 decay products of the Higgs Boson itself. The kinematics of the particles this layer identifies as  
 218 most likely to have originated from the Higgs decay are then fed into yet another neural-network,  
 219 which predicts the momentum of the Higgs (5.5). For the 3l channel, an additional MVA is used  
 220 to determine the decay mode of the Higgs boson in the 3l channel (5.6).

221 Models are trained on Monte Carlo simulations of  $t\bar{t}H$  events generated using MG5\_AMC.  
 222 Specifically, events DSIDs 346343-5, 345873-5, and 345672-4 are used for training in order to  
 223 increase the statistics of the training sample.

224 For all of these models, the Keras neural network framework, with Tensorflow 2.0 as the backend,  
 225 is used, and the number of hidden layers and nodes are determined using grid search optimization.  
 226 Each neural network uses the LeakyReLU activation function, a learning rate of 0.01, and the  
 227 Adam optimization algorithm, as alternatives are found to either decrease or have no impact on  
 228 performance. Batch normalization is applied after each layer in order to stabilize the model and  
 229 decrease training time. For the classification algorithms (b-jet matching, Higgs reconstruction,  
 230 and 3l decay identification) binary-cross entropy is used as the loss function, while the  $p_T$   
 231 reconstruction algorithm uses MSE.

232 The specific inputs features used for each model are arrived at through a process of trial and error  
 233 - features considered potentially useful are tried, and those that are found to increase performance  
 234 are included. While each model includes a relatively large number of features, some using  
 235 upwards of 30, this inclusive approach is found to maximize the performance of each model while

236 decreasing the variance compared to a reduced number of inputs. Each input feature is validated  
 237 by comparing MC simulations to  $79.8 \text{ fb}^{-1}$  of data, as shown in the sections below.

## 238 **5.1 Physics Object Truth Matching**

239 Machine Learning algorithms are trained to identify the decay products of the Higgs Boson using  
 240 MC simulations of  $t\bar{t}H$  events. The kinematics of the reconstructed physics objects, as well as  
 241 event level variables, are used as inputs, with the parent ID taken from the truth record used to  
 242 label the data. The objects considered include light leptons and jets.

243 Reconstructed physics objects are matched to particle level objects, in order to identify the parent  
 244 particle of these reconstructed objects. Reconstructed jets are matched to truth jets based on  
 245 the requirements that the reco jet and truth jet fall within  $\Delta R < 0.4$ , and the two objects have  
 246 a  $p_T$  that agrees within 10%. Truth level and reco level leptons are required to have the same  
 247 flavor, a  $\Delta R < 0.1$ , and  $p_T$  that agree within 10%. Events where no match can be found between  
 248 the particle level decay products of the Higgs and the reconstructed objects are not included in  
 249 training.

250 Leptons considered as possible Higgs and top decay candidates are required to pass the selection  
 251 described in Section 4.2. For jets, however, it is found that a large fraction that originate from either  
 252 the top decay or the Higgs decay fall outside the selection described in Section 4.3. Specifically,  
 253 jets from the Higgs decay tend to be soft, with 32% having  $p_T < 25 \text{ GeV}$ . Therefore jets with  $p_T$   
 254  $< 15 \text{ GeV}$  are considered as possible candidates in the models described below. By contrast, less  
 255 than 5% of the jets originating from the Higgs fall below this  $p_T$  threshold. The jets are found to  
 256 be well modeled even down to this low  $p_T$  threshold, as shown in Section 6.1. The impact of  
 257 using different  $p_T$  selection for the jet candidates is considered in detail in Section B.6. As they  
 258 are expected to originate from the primary vertex, jets are also required to pass a JVT cut.

## 259 **5.2 Truth Level Studies**

260 Attempts to identify the decay products of the Higgs are motivated by the ability to reconstruct  
 261 the Higgs momentum based on their kinematics. In order to demonstrate that this is case, the  
 262 kinematics of reconstructed objects that are truth matched to the Higgs decay are used as inputs  
 263 to a neural network which is designed to predict the momentum of the Higgs. This is done in  
 264 the 2lSS channel -

## 265 **5.3 b-jet Identification**

266 Including the kinematics of the b-jets that originate from the top decay is found to improve the  
 267 identification of the Higgs decay products, and improve the accuracy with which the Higgs  
 268 momentum can be reconstructed. Because these b-jets are reconstructed by the detector with high

efficiency (just over 90% of the time), and can be identified relatively consistently, the first step in reconstructing the Higgs is selecting the b-jets from the top decay.

Exactly two b-jets are expected in the final state of  $t\bar{t}H - ML$  events. However, in both the 3l and 2lSS channels, only one or more b-tagged jets are required (where the 70% DL1r b-tag working point is used). Therefore, for events which have exactly one, or more than two, b-tagged jets, deciding which combination of jets correspond to the top decay is non-trivial. Further, events with 1 b-tagged jet represent just over half of all  $t\bar{t}H - ML$  events. Of those, both b-jets are reconstructed by the detector 75% of the time. Therefore, rather than adjusting the selection to require exactly 2 b-tagged jets, and losing more than half of the signal events, a neural network is used to predict which pair of jets is most likely to correspond to truth b-jets.

Once the network is trained, all possible pairings of jets are fed into the model, and the pair of jets with the highest output score are taken to be b-jets in successive steps of the analysis.

### 5.3.1 2lSS Channel

For the 2lSS channel, the input features shown in Table 5 are used for training. Here  $j_0$  and  $j_1$  are the two jet candidates, while  $l_0$  and  $l_1$  are the two leptons in the event, both ordered by  $p_T$ . jet DL1r is an integer corresponding to the calibrated b-tagging working points reached by each jet, where 5 represents the tightest working point and 1 represents the loosest. The variables nJets DL1r 60% and nJets DL1r 85% represent the number of jets in the event passing the 60% and 85% b-tag working points, respectively.

jet $p_T$ 0	jet $p_T$ 1	Lepton $p_T$ 0
Lepton $p_T$ 1	jet $\eta$ 0	jet $\eta$ 1
$\Delta R(j_0)(j_1)$	$M(j_0 j_1)$	$\Delta R(l_0)(j_0)$
$\Delta R(l_0)(j_1)$	$\Delta R(l_1)(j_0)$	$\Delta R(l_1)(j_1)$
$M(l_0 j_0)$	$M(l_0 j_1)$	$M(l_1 j_0)$
$M(l_1 j_1)$	jet DL1r 0	jet DL1r 1
nJets OR DL1r 85	nJets OR DL1r 60	$\Delta R(j_0 l_0)(j_1 l_1)$
$\Delta R(j_0 l_1)(j_1 l_0)$	$p_T(j_0 j_1 l_0 l_1 E_T^{\text{miss}})$	$M(j_0 j_1 l_0 l_1 E_T^{\text{miss}})$
$\Delta\phi(j_0)(E_T^{\text{miss}})$	$\Delta\phi(j_1)(E_T^{\text{miss}})$	HT jets
nJets	$E_T^{\text{miss}}$	

Table 5: Input features used in the b-jet identification algorithm for the 2lSS channel

As there are far more incorrect combinations than correct ones, by a factor of more than 20:1, the training set is resampled to reduce the fraction of incorrect combinations. A random sample of 5 million incorrect entries are used for training, along with close 1 million correct entries. 10% of the dataset is set aside for testing, leaving around 5 million datapoints for training.

292 The difference between the distributions for a few of these features for the "correct" (i.e. both jets  
 293 are truth b-jets), and "incorrect" combinations are shown in Figure 5.1. The correct and incorrect  
 294 contributions are scaled to the same integral, so as to better demonstrate the differences in the  
 295 distributions.

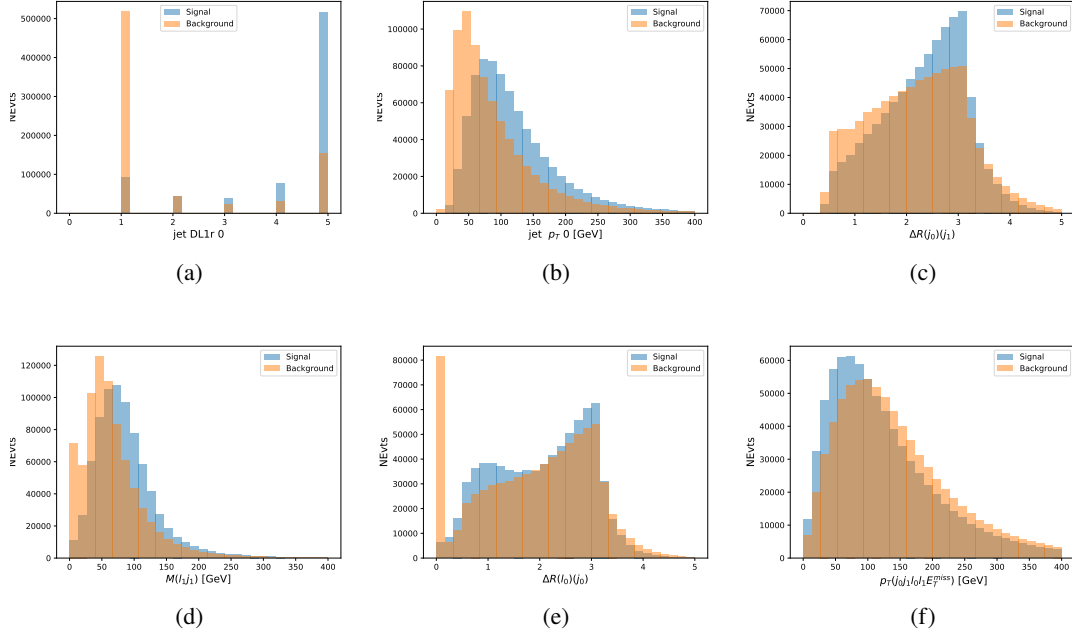


Figure 5.1: Input features for top2ISS training. The signal in blue represents events where both jet candidates are truth b-jets from top decays, and the orange is all other combinations. Each are scaled to the same number of events. (a) shows the DL1r working point of leading jet, (b) shows the  $p_T$  of the leading jet, (c) shows the  $\Delta R$  of the two jets, (d) the invariant mass of lepton 1 and jet 1, (e) the  $\Delta R$  of lepton 0 and jet 0, and (f) the  $p_T$  of both jets, both leptons, and the  $E_T^{\text{miss}}$ .

296 The modeling of these inputs is validated against data, with Figure 5.2 showing good general  
 297 agreement between data and MC. Plots for the complete list of features can be found in Section B.

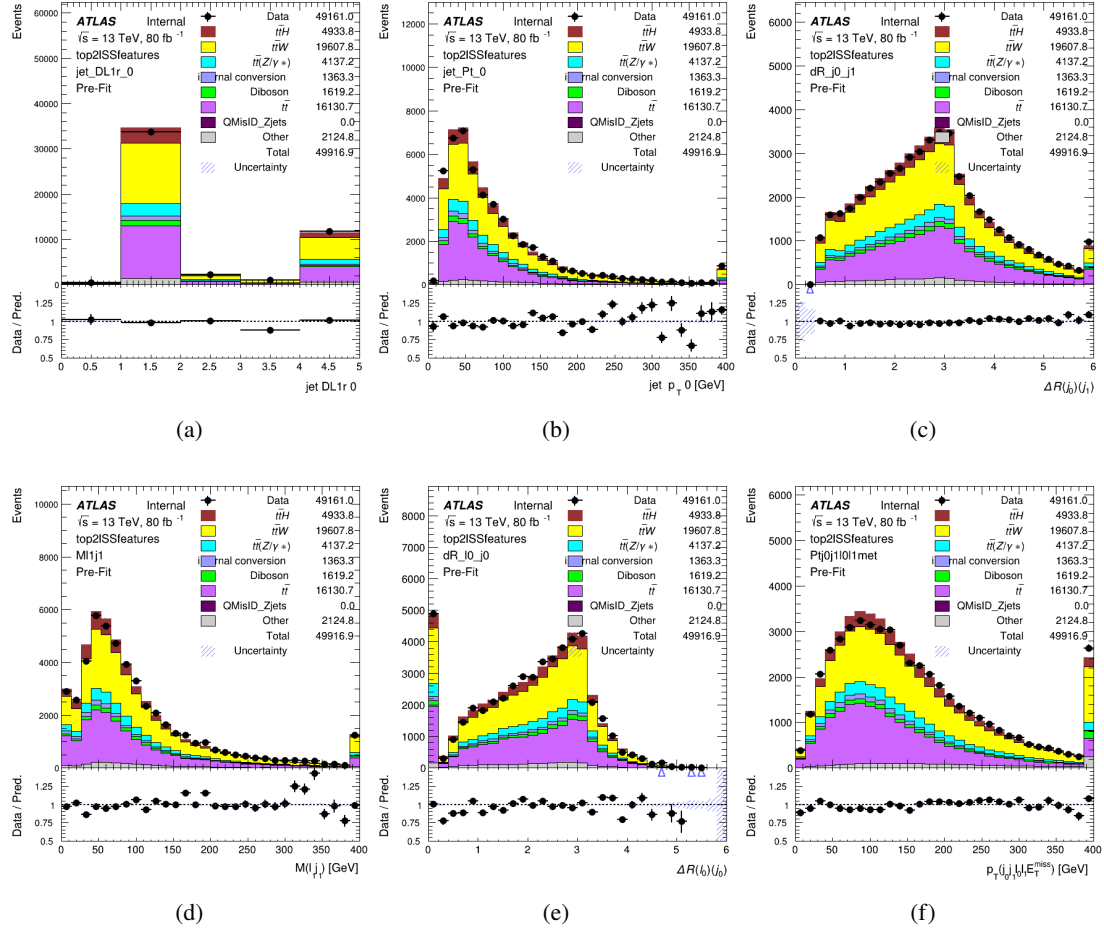


Figure 5.2: Data/MC comparisons of input features for top2ISS training for  $79.8 \text{ fb}^{-1}$  of data. (a) shows the DL1r working point of leading jet, (b) shows the  $p_T$  of the leading jet, (c) shows the  $\Delta R$  of the two jets, (d) the invariant mass of lepton 1 and jet 1, (e) the  $\Delta R$  of lepton 0 and jet 0, and (f) the  $p_T$  of both jets, both leptons, and the  $E_T^{\text{miss}}$ .

Based on the results of grid search evaluation, the optimal architecture is found to include 5 hidden layers with 40 nodes each. No regularizer or dropout is added to the network, as overfitting is found to not be an issue. The output score distribution as well as the ROC curve for the trained model are shown in Figure 5.3.1. The model is found to identify the correct pairing of jets for 73% of 2ISS signal events on test data.

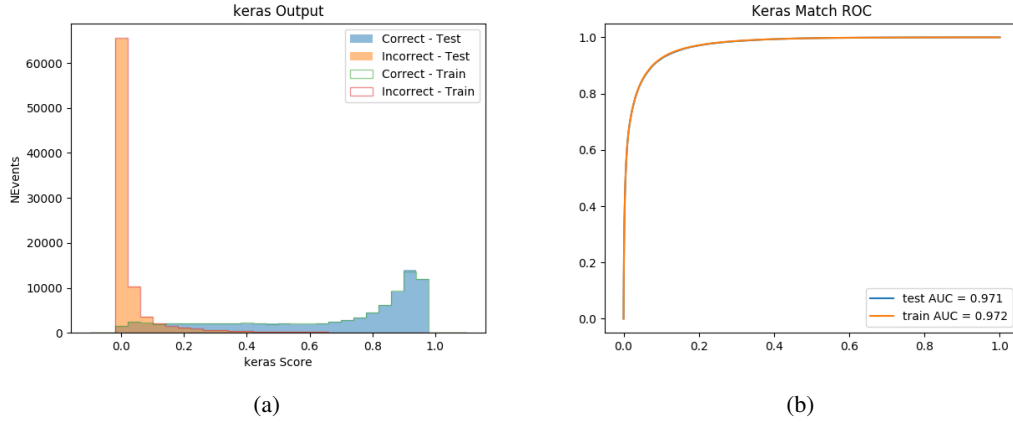


Figure 5.3: Results of the b-jet identification algorithm for the 2lSS channel, showing (a) the output score of the NN for correct and incorrect combinations of jets. (b) the ROC curve of the output, showing background rejection as a function of signal efficiency

303 For point of comparison, a "naive" approach to identify b-jets is used as well: The two jets which  
 304 pass the highest DL1r b-tag working point are assumed to be the b-jets from the top decay. In the  
 305 case that multiple jets meet the same b-tag working point, the jet with higher  $p_T$  is used. This  
 306 method identifies the correct jet pair 65% of the time.

307 The accuracy of the model for different values of n-bjets, compared to this naive approach, is  
 308 shown in Table 6.

b-jet Selection	Neural Network	Naive
1 b-jet	58.6%	42.1%
2 b-jets	88.4%	87.1%
$\geq 3$ b-jets	61.7%	53.3%
Overall	73.9%	67.2%

Table 6: Accuracy of the NN in identifying b-jets from tops in 2lSS events, overall and split by the number of b-tagged jets in the event, compared to the accuracy of taking the two highest b-tagged jets.

### 309 5.3.2 3l Channel

310 The input features used in the 3l channel are listed in Table 7, with the same naming convention  
 311 as the 2lSS channel.

jet $p_T$ 0	jet $p_T$ 1	jet $\eta$ 0
jet $\eta$ 1	Lepton $p_T$ 0	Lepton $p_T$ 1
Lepton $p_T$ 2	$\Delta R(j_0)(j_1)$	$M(j_0 j_1)$
$\Delta R(l_0)(j_0)$	$\Delta R(l_1)(j_0)$	$\Delta R(l_2)(j_0)$
$\Delta R(l_0)(j_1)$	$\Delta R(l_1)(j_1)$	$\Delta R(l_2)(j_1)$
$M(l_0 j_0)$	$M(l_1 j_0)$	$M(l_2 j_0)$
$M(l_0 j_1)$	$M(l_1 j_1)$	$M(l_2 j_1)$
$\Delta R(j_0 l_0)(j_1 l_1)$	$\Delta R(j_0 l_0)(j_1 l_2)$	$\Delta R(j_0 l_1)(j_1 l_0)$
$\Delta R(j_0 l_2)(j_1 l_0)$	jet DL1r 0	jet DL1r 1
$p_T(j_0 j_1 l_0 l_1 l_2 E_T^{\text{miss}})$	$M(t j_0 j_1 l_0 l_1 l_2 E_T^{\text{miss}})$	$\Delta\phi(j_0)(E_T^{\text{miss}})$
$\Delta\phi(j_1)(E_T^{\text{miss}})$	HT Lepton	HT jets
nJets	$E_T^{\text{miss}}$	nJets OR DL1r 85
nJets OR DL1r 60		

Table 7: Input features for the b-jet identification algorithm in the 3l channel.

312 A few of these features are shown in Figure 5.4, comparing the distributions for correct and  
 313 incorrect combinations of jets.

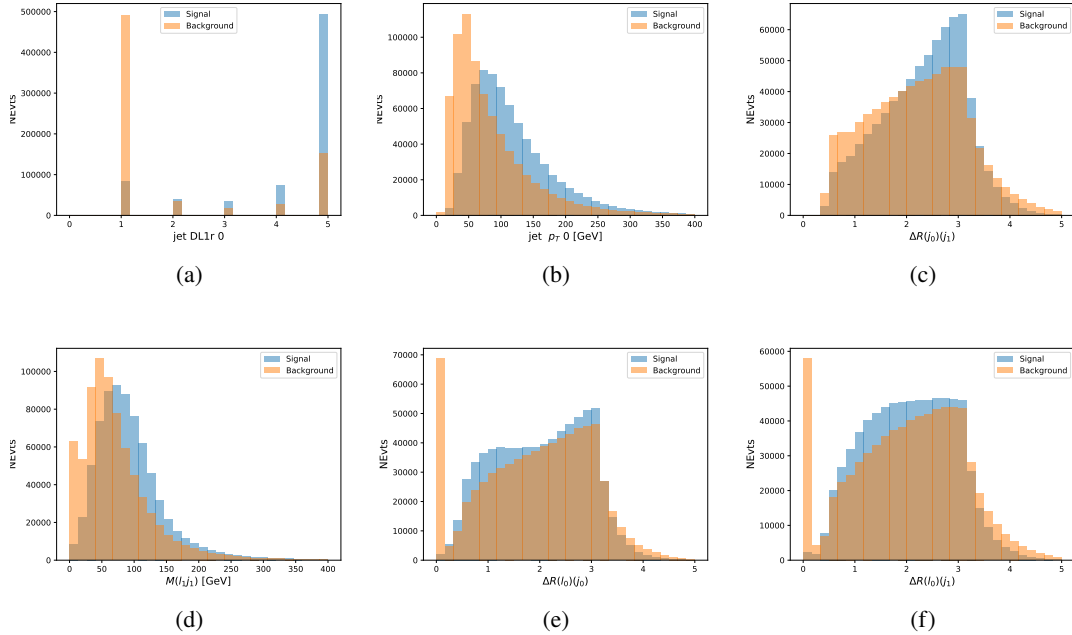


Figure 5.4: Input features for top31 training. The signal in blue represents events where both jet candidates are truth b-jets from top decays, and the orange is all other combinations. Scaled to the same number of events. (a) show the DL1r WP of jet 0, (b) the  $p_T$  of jet 0, (c)  $\Delta R$  between jet 0 and jet 1, (d) the invariant mass of lepton 1 and jet 1, (e)  $\Delta R$  between lepton 0 and jet 0, and (f)  $\Delta R$  between lepton 0 and jet 1

314 The modeling of these inputs is validated against data, with Figure 5.5 showing good general  
 315 agreement between data and MC. Plots for the complete list of features can be found in Section B.

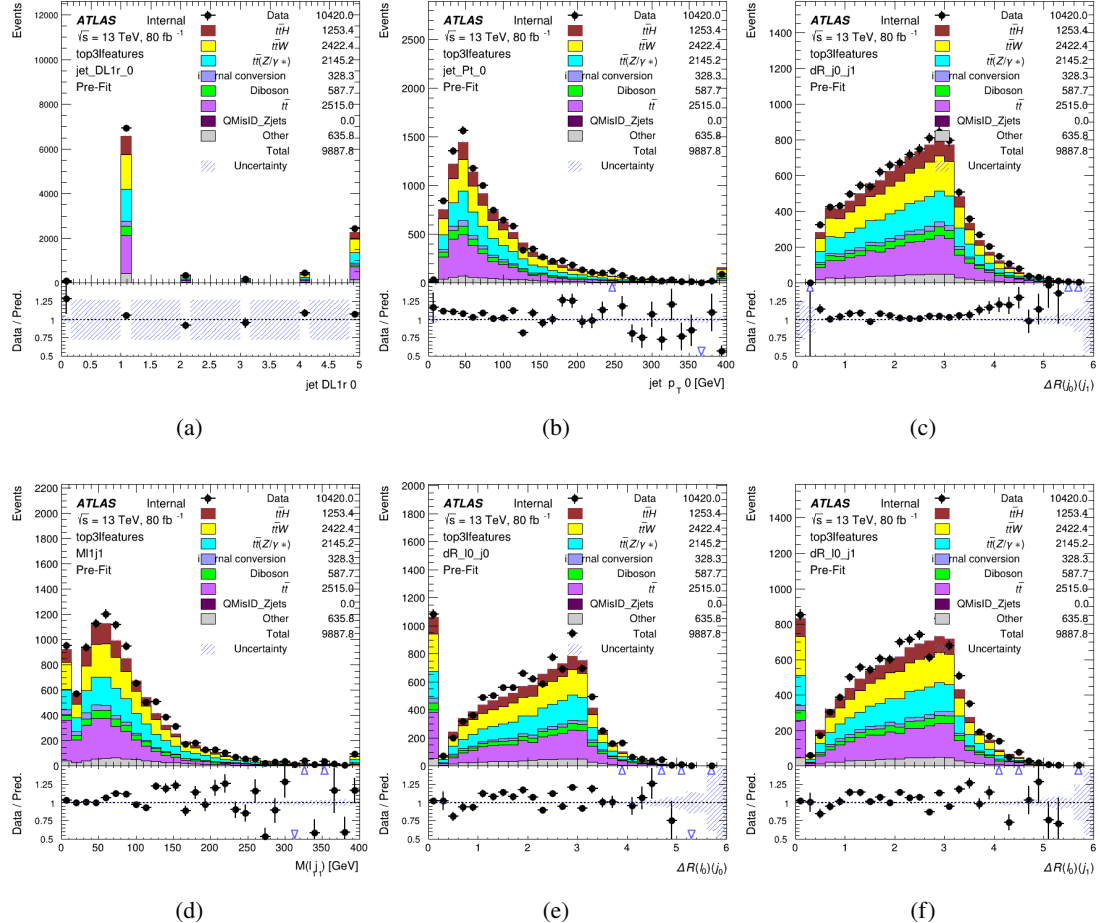


Figure 5.5: Data/MC comparisons of input features for top3l training for  $79.8 \text{ fb}^{-1}$  of data. (a) show the DL1r WP of jet 0, (b) the  $p_T$  of jet 0, (c)  $\Delta R$  between jet 0 and jet 1, (d) the invariant mass of lepton 1 and jet 1, (e)  $\Delta R$  between lepton 0 and jet 0, and (f)  $\Delta R$  between lepton 0 and jet 1

316 Again, the dataset is downsized to reduce the ratio of correct and incorrect combination from 20:1,  
 317 to 5:1. Around 7 million events are used for training, with 10% set aside for testing. Based on the  
 318 results of grid search evaluation, the optimal architecture is found to include 5 hidden layers with  
 319 60 nodes each. The output score distribution as well as the ROC curve for the trained model are  
 320 shown in Figure 5.3.2.

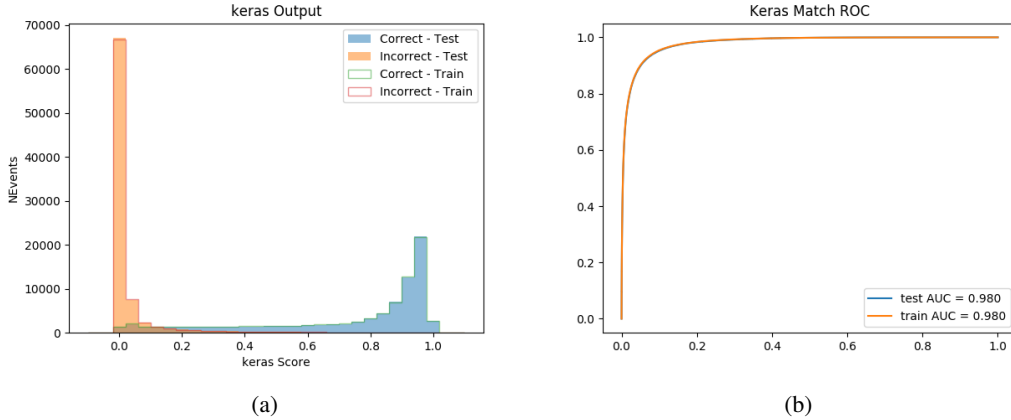


Figure 5.6: Results of the b-jet identification algorithm for the 3l channel, showing (a) the output score of the NN for correct and incorrect combinations of jets. (b) the ROC curve of the output, showing background rejection as a function of signal efficiency

321 This procedure is found to identify the correct pairing of jets for nearly 80% of 3l signal events.  
 322 The accuracy of the model is summarized in Table 8.

Table 8: Accuracy of the NN in identifying b-jets from tops, compared to the naive method of taking the highest b-tagged jets.

	NN	Naive
1 b-jet	69.0%	48.9%
2 b-jets	89.6%	88.3%
$\geq 3$ b-jets	55.7%	52.3%
Overall	79.8%	70.2%

## 323 5.4 Higgs Reconstruction

324 Techniques similar to the b-jet identification algorithms are employed to select the decay products  
 325 of the Higgs: kinematics of all possible combinations of reconstructed objects are fed into a neural  
 326 network to determine which of those is most mostly to be the decay products of the Higgs.

327 Again separate models are used for the 2lSS and 3l channels, while the 3l channel has now been  
 328 split into two:  $t\bar{t}H$  events with three leptons in the final state include both instances where the  
 329 Higgs decays into a lepton (and a neutrino) and a pair of jets, and instances where the Higgs  
 330 decays to two leptons.

331 3l events are therefore categorized as either semi-leptonic (3lS) or fully-leptonic (3lF). In the  
 332 semi-leptonic case the reconstructed decay products consist of two jets and a single leptons. For

333 the fully-leptonic case, the decay products include 2 of the three leptons associated with the  
 334 event. For training the models, events are separated into these two categories using truth level  
 335 information. A separate MVA, described in Section 5.6, is used to make this distinction at reco  
 336 level and determine which model to use.

337 For all channels, the models described in Section 5.3 are used to identify b-jet candidates, whose  
 338 kinematics are used to identify the Higgs decay products. These jets are not considered as possible  
 339 candidates for the Higgs decay, justified by the fact that these models are found to misidentify jets  
 340 from the Higgs decay as jets from the top decay less than 1% of the time.

#### 341 5.4.1 2ISS Channel

342 For the 2ISS channel, the Higgs decay products include one light lepton and two jets. The neural  
 343 network is trained on the kinematics of different combinations of leptons and jets, as well as the  
 344 b-jets identified in Section 5.3, with the specific input features listed in Table 9.

Lepton $p_T$ H	Lepton $p_T$ T	jet $p_T$ 0
jet $p_T$ 1	top $p_T$ 0	top $p_T$ 1
top $\eta$ 0	top $\eta$ 1	jet $\eta$ 0
jet $\eta$ 1	jet Phi 0	jet Phi 1
Lepton $\eta$ H	Lepton heta T	$\Delta R(j_0)(j_1)$
$\Delta R(l_H)(j_0)$	$\Delta R(l_H)(j_1)$	$M(j_0 j_1)$
$M(l_H j_0)$	$M(l_H j_1)$	$\Delta R(l_H)(b_0)$
$\Delta R(l_H)(b_1)$	$\Delta R(l_T)(b_0)$	$\Delta R(l_T)(b_1)$
$\Delta R(j_0 j_1)(l_H)$	$\Delta R(j_0 j_1)(l_T)$	$\Delta R(j_0 j_1)(b_0)$
$\Delta R(j_0 j_1)(b_1)$	$\Delta R(j_0)(b_0)$	$\Delta R(j_0)(b_1)$
$\Delta R(j_1)(b_0)$	$\Delta R(j_1)(b_1)$	$M(j_0 j_1 l_H)$
$p_T(j_0 j_1 l_H l_T b_0 b_1 E_T^{\text{miss}})$	topScore	$E_T^{\text{miss}}$
nJets	HT jets	

Table 9: Input features used to identify the Higgs decay products in 2ISS events

345 Here  $j_0$  and  $j_1$ , and  $l_H$  are the jet and lepton decay candidates, respectively. The other lepton in  
 346 the event is labeled  $l_T$ , as it is assumed to have come from the decay of one of the top quarks.  $b_0$   
 347 and  $b_1$  are the two b-jets identified by the b-jet identification algorithm. The b-jet Reco Score is  
 348 the output of the b-jet reconstruction algorithm.

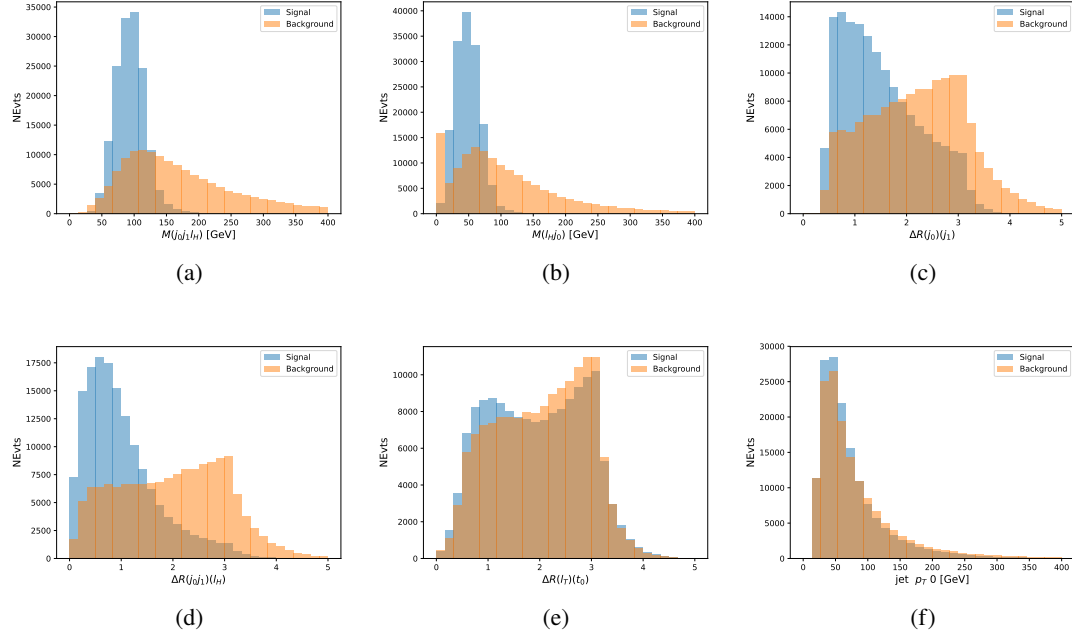


Figure 5.7: Input features for higgs2lSS training. The signal in blue represents events where both jet candidates are truth b-jets from top decays, and the orange is all other combinations. Scaled to the same number of events. (a) shows the invariant mass of the two jet candidates and the lepton candidate, (b) the invariant mass of jet 0 and the lepton candidate, (c)  $\Delta R$  between the jet candidates, (d)  $\Delta R$  between jet 0 + jet 1 and the lepton candidate, (e)  $\Delta R$  between the lepton from the top and the leading b-jet, (f) the  $p_T$  of jet 0.

349 The modeling of these inputs is validated against data, with Figure 5.2 showing good general  
 350 agreement between data and MC. Plots for the complete list of features can be found in Section B.

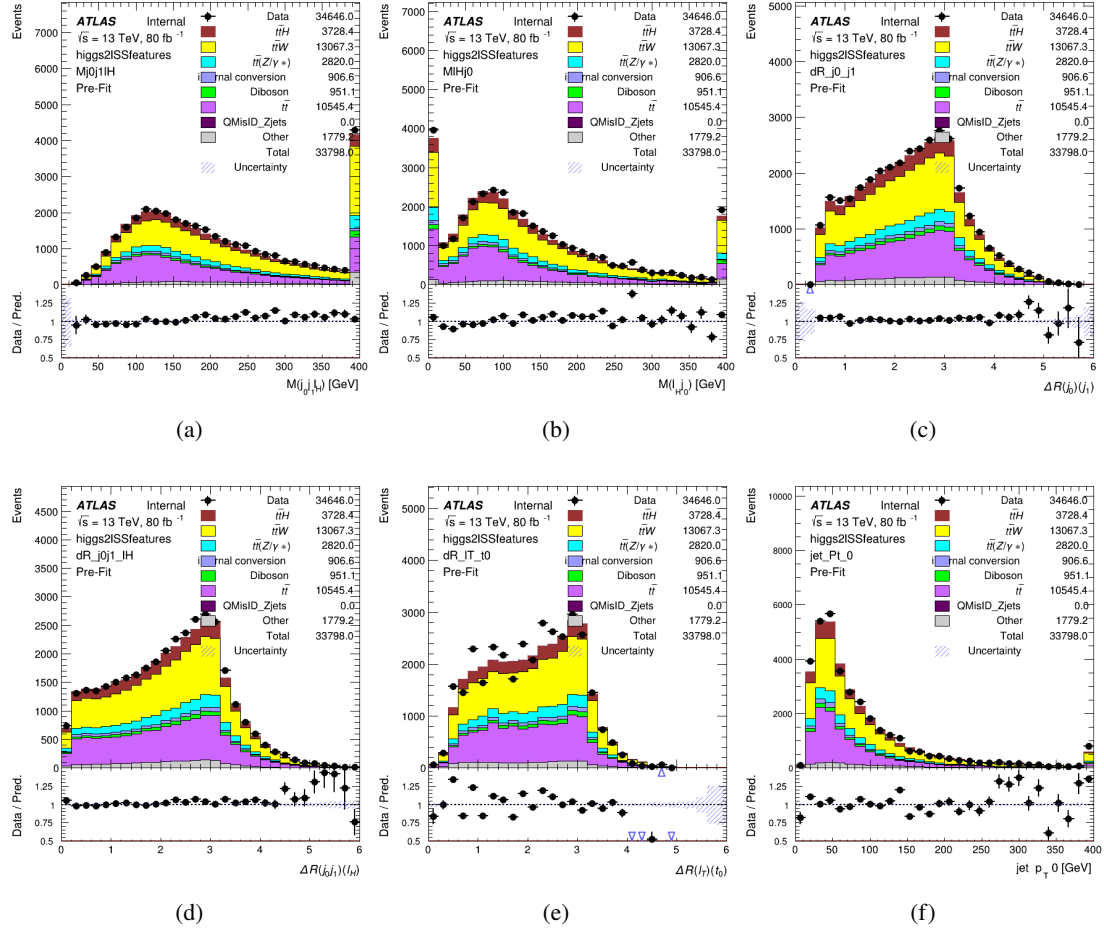


Figure 5.8: Data/MC comparisons of input features for higgs2lSS training for  $79.8 \text{ fb}^{-1}$  of data. (a) shows the invariant mass of the two jet candidates and the lepton candidate, (b) the invariant mass of jet 0 and the lepton candidate, (c)  $\Delta R$  between the jet candidates, (d)  $\Delta R$  between jet 0 + jet 1 and the lepton candidate, (e)  $\Delta R$  between the lepton from the top and the leading b-jet, (f) the  $p_T$  of jet 0.

351 A neural network consisting of 7 hidden layers with 60 nodes each is trained on around 2 million  
 352 events, with an additional 200,000 reserved for testing the model. In order to compensate for  
 353 large number of incorrect combinations, these have been downsampled such that the correct  
 354 combinations represent over 10% of the training set. The output of the NN is summarized in  
 355 Figure 5.4.1.

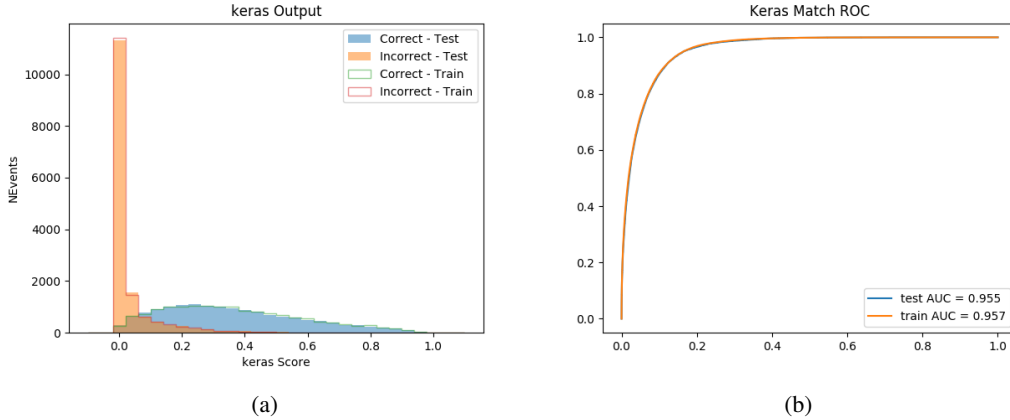


Figure 5.9: Result of the Higgs reconstruction algorithm in the 2lSS channel, showing (a) the output score of the NN for correct and incorrect combinations of jets scaled to an equal number of events, and (b) the ROC curve of the output, showing background rejection as a function of signal efficiency

356 The neural network identifies the correct combination 55% of the time. It identifies the correct  
 357 lepton 85% of the time, and selects the correct lepton and at least one of the correct jets 81% of  
 358 the time.

#### 359 5.4.2 3l Semi-leptonic Channel

360 For 3l  $t\bar{t}H$  where the Higgs decay semi-leptonically, the decay products include one of the three  
 361 leptons and two jets. In this case, the other two leptons originated from the decay of the tops,  
 362 meaning the opposite-sign (OS) lepton cannot have come from the Higgs. This leaves only the two  
 363 same-sign (SS) leptons as possible Higgs decay products.

Lepton $p_T H$	Lepton $p_T T_0$	Lepton $p_T T_1$
jet $p_T 0$	jet $p_T 1$	top $p_T 0$
top $p_T 1$	jet $\eta 0$	jet $\eta 1$
jet $\phi 0$	jet $\phi 1$	$\Delta R(j_0)(j_1)$
$M(j_0 j_1)$	$\Delta R(l_H)(j_0)$	$\Delta R(l_H)(j_1)$
$\Delta R(j_0 j_1)(l_H)$	$\Delta R(j_0 j_1)(l_{T_1})$	$\Delta R(l_{T_0})(l_{T_1})$
$\Delta R(l_H)(l_{T_1})$	$M(j_0 j_1 l_{T_0})$	$M(j_0 j_1 l_{T_1})$
$M(j_0 j_1 l_H)$	$\Delta R(j_0 j_1 l_H)(l_{T_0})$	$\Delta R(j_0 j_1 l_H)(l_{T_1})$
$\Delta\phi(j_0 j_1 l_H)(E_T^{\text{miss}})$	$p_T(j_0 j_1 l_H l_{T_0} l_{T_1} b_0 b_1 E_T^{\text{miss}})$	$M(j_0 j_1 b_0)$
$M(j_0 j_1 b_1)$	$\Delta R(l_{T_0})(b_0)$	$\Delta R(l_{T_0})(b_1)$
$\Delta R(l_{T_1})(b_0)$	$\Delta R(l_{T_1})(b_1)$	$\Delta R(j_0)(b_0)$
$\Delta R(j_0)(b_1)$	$\Delta R(j_1)(b_0)$	$\Delta R(j_1)(b_1)$
topScore	MET	HT jets
nJets		

Table 10: Input features used to identify the Higgs decay products in 31 semi-leptonic events

364 Here  $j_0$  and  $j_1$ , and  $l_H$  are the jet and lepton decay candidates, respectively. The other two  
 365 leptons in the event are labeled as  $l_{T_0}$  and  $l_{T_1}$ .  $b_0$  and  $b_1$  are the two b-jets identified by the  
 366 b-jet identification algorithm. The b-jet Reco Score is the output of the Higgs reconstruction  
 367 algorithm.

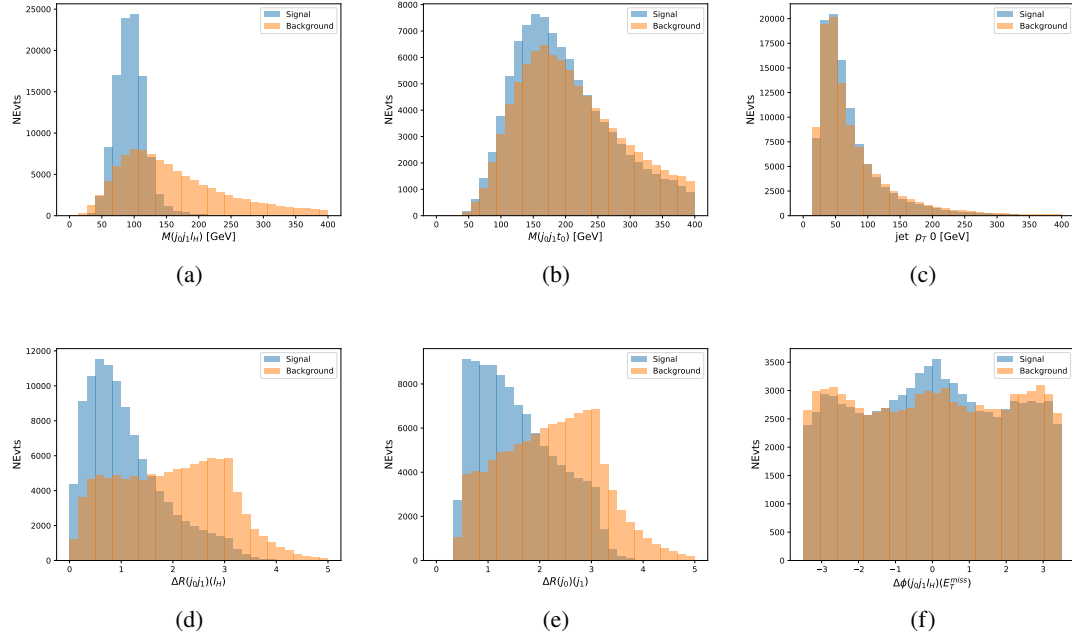


Figure 5.10: Input features for higgs3lS training. The signal in blue represents events where both jet candidates are truth b-jets from top decays, and the orange is all other combinations. Scaled to the same number of events.

368 The modeling of these inputs is validated against data, with Figure 5.11 showing good general  
 369 agreement between data and MC. Plots for the complete list of features can found in appendix  
 370 [B.1](#).

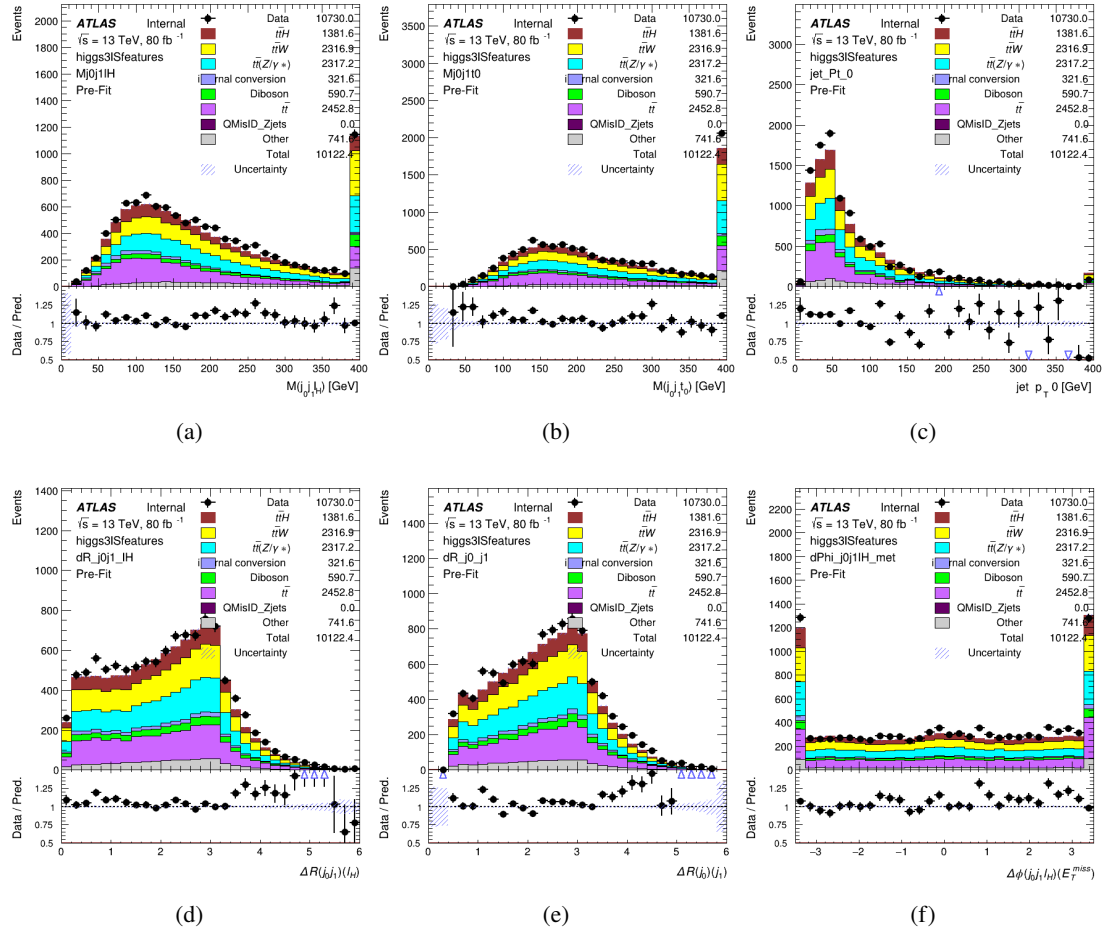


Figure 5.11: Data/MC comparisons of input features for higgs3lS training for  $79.8 \text{ fb}^{-1}$  of data.

371 A neural network of 7 hidden layers with 70 nodes each is trained on 1.8 million events. Once  
 372 again, incorrect combinations are downsampled, such that the correct combinations are around  
 373 10% of the training set. 10% of the dataset is reserved for testing. The output of the NN is  
 374 summarized in Figure 5.4.2.

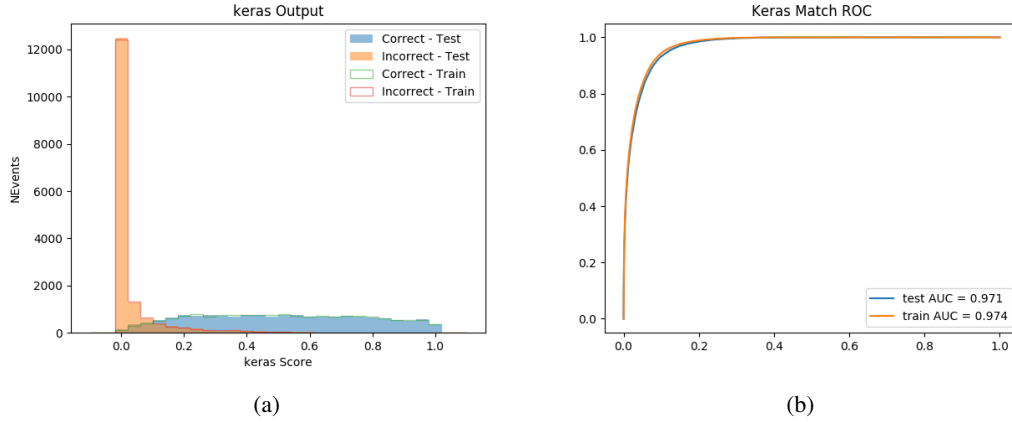


Figure 5.12: Results of the Higgs reconstruction algorithm in the 3lS channel, showing (a) the output score of the NN for correct and incorrect combinations of jets, scaled to an equal number of entries.,. (b) the ROC curve of the output, showing background rejection as a function of signal efficiency

375 The neural network identifies the correct combination 64% of the time. It identifies the correct  
 376 lepton 85% of the time, and selects the correct lepton and at least one of the correct jets 83% of  
 377 the time.

### 378 5.4.3 3l Fully-leptonic Channel

379 In the fully-leptonic 3l case, the goal is identify which two of the three leptons originated from  
 380 the Higgs decay. Since one of these two must be the OS lepton, this problem is reduced to  
 381 determining which of the two SS leptons originated from the Higgs. The kinematics of both  
 382 possibilities are used for training, one where the SS lepton from the Higgs is correctly labeled,  
 383 and one where it is not.

Lepton $p_T H_1$	Lepton $p_T H_0$	Lepton $p_T T$
top $p_T 0$	top $p_T 1$	$\Delta\phi(l_{H_1})(E_T^{\text{miss}})$
$\Delta\phi(l_T)(E_T^{\text{miss}})$	$M(l_{H_0}l_{H_1})$	$M(l_{H_1}l_T)$
$M(l_{H_0}l_T)$	$\Delta R(l_{H_0})(l_{H_1})$	$\Delta R(l_{H_1})(l_T)$
$\Delta R(l_{H_0})(l_T)$	$\Delta R(l_{H_0}l_{H_1})(l_T)$	$\Delta R(l_{H_0}l_T)(l_{H_1})$
$\Delta R(l_{H_0}l_{H_1})(b_0)$	$\Delta R(l_{H_0}l_{H_1})(b_1)$	$\Delta R(l_{H_0}b_0)$
$M(l_{H_0}b_0)$	$\Delta R(l_{H_0}b_1)$	$M(l_{H_0}b_1)$
$\Delta R(l_{H_1}b_0)$	$M(l_{H_1}b_0)$	$\Delta R(l_{H_1}b_1)$
$M(l_{H_1}b_1)$	$E_T^{\text{miss}}$	topScore

Table 11: Input features used to identify the Higgs decay products in 3lF events

Table 12: Input features used to identify the Higgs decay products in 3l fully leptonic events

384 Here  $l_{H_0}$  and  $l_{H_1}$  are the Higgs decay candidates. The other lepton in the event is labeled  $l_T$ .  $b_0$   
 385 and  $b_1$  are the two b-jets identified by the b-jet identification algorithm. The b-jet Reco Score is  
 386 the output of the Higgs reconstruction algorithm.

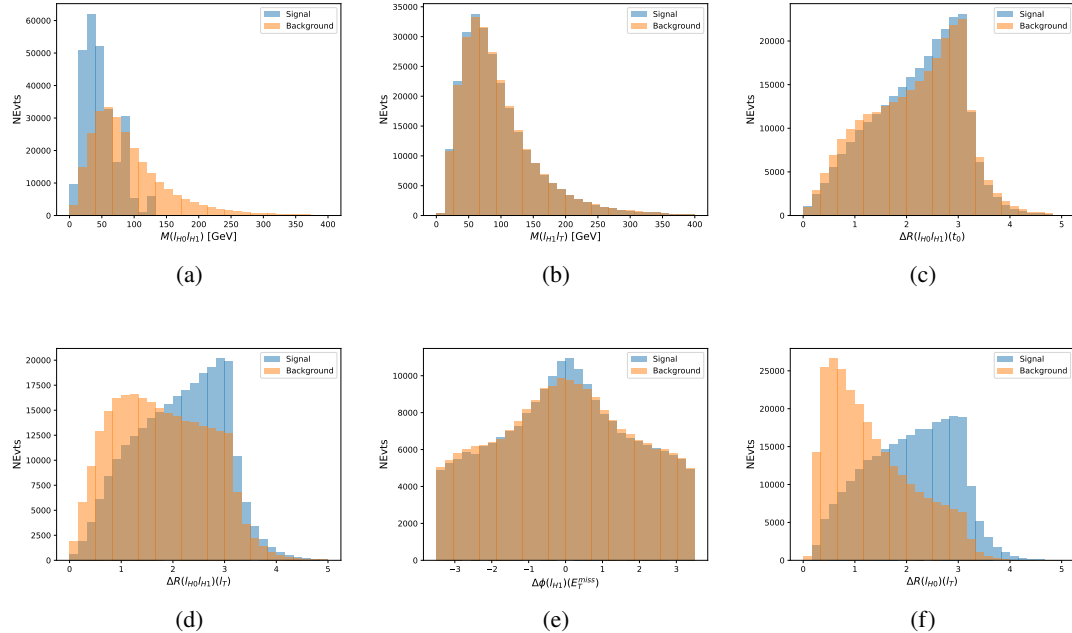


Figure 5.13: Input features for higgs3lF training. The signal in blue represents events where both jet candidates are truth b-jets from top decays, and the orange is all other combinations. Scaled to the same number of events.

387 The modeling of these inputs is validated against data, with Figure 5.14 showing good general  
 388 agreement between data and MC. Plots for the complete list of features can be found in Section B.

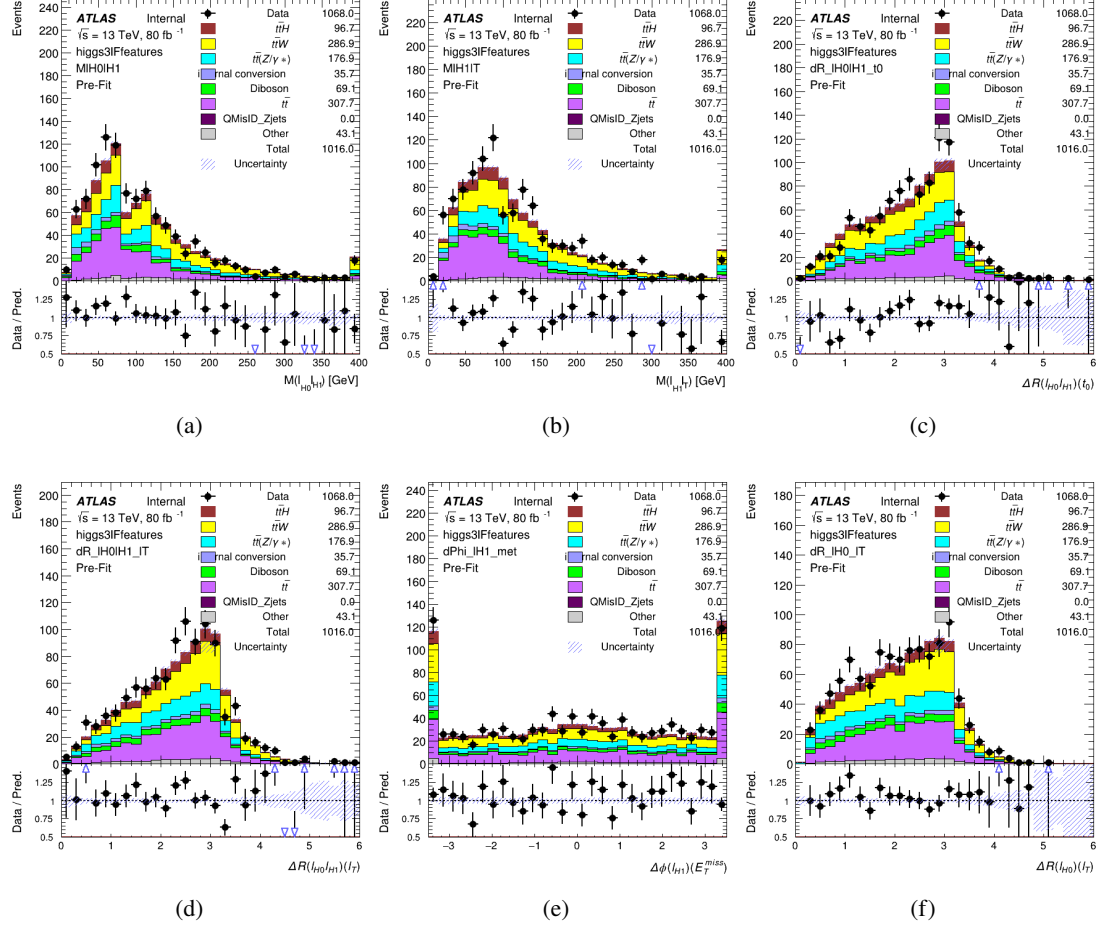


Figure 5.14: Data/MC comparisons of input features for higgs3IF training for  $79.8 \text{ fb}^{-1}$  of data.

389 A neural network consisting of 5 nodes and 60 hidden units is trained on 800,000 events, with  
 390 10% of the dataset reserved for testing. The output of the model is summarized in Figure 5.4.3.

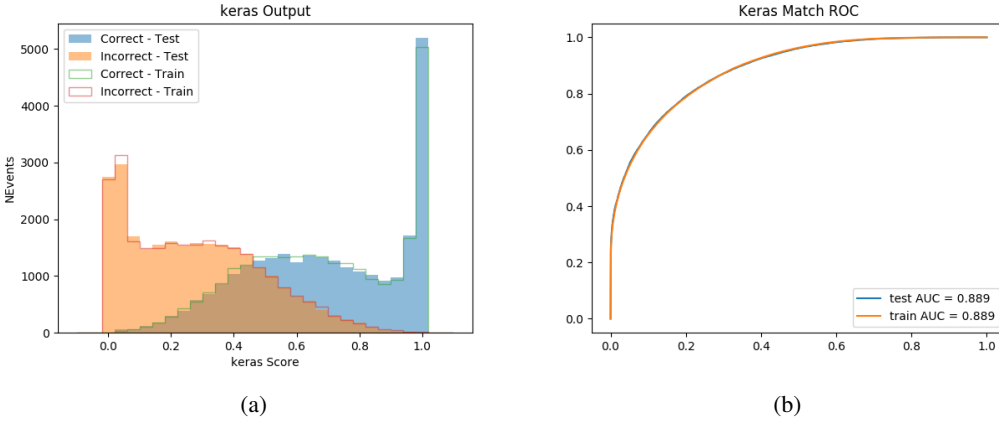


Figure 5.15: (a) the output score of the NN for correct and incorrect combinations of jets. (a) the ROC curve of the output, showing background rejection as a function of signal efficiency

391 The correct lepton is identified by the model for 80% of events in the testing data set.

## 392 5.5 $p_T$ Prediction

393 Once the most probable decay products have been identified, their kinematics are used as inputs  
 394 to a regression model which attempts to predict the momentum of the Higgs Boson. Once again,  
 395 a DNN is used. Input variables representing the b-jets and leptons not from the Higgs decay  
 396 are included as well, as these are found to improve performance. The truth  $p_T$  of the Higgs,  
 397 as predicted by MC, are used as labels. Separate models are built for each channel - 2lSS, 3l  
 398 Semi-leptonic and 3l Fully-leptonic.

399 As a two-bin fit is targeted for the final result, some metrics evaluating the performance of the  
 400 models aim to show how well it distinguishes between "high  $p_T$ " and "low  $p_T$ " events. A cutoff  
 401 point of 150 GeV is used to define these two categories.

402 Because the analysis uses a two bin fit of the Higgs  $p_T$ , the momentum reconstruction could be  
 403 treated as a binary classification problem, rather than a regression problem. This approach is  
 404 explored in detail in Section B.5, and is found not to provide any significant increase in sensitivity.  
 405 The regression approach is used because it provides more flexibility for future analyses, as it is  
 406 independent of the cutoff between high and low  $p_T$ , as well as the number of bins. Further, a  
 407 regression allows the output of the neural network to be more clearly understood, as it can be  
 408 directly compared to a physics observable.

---

409 **5.5.1 2ISS Channel**

410 The input variables listed in Table 13 are used to predict the Higgs  $p_T$  in the 2ISS channel. Here  
411  $j_0$  and  $j_1$  are the two jets identified as Higgs decay products. The lepton identified as originating  
412 from the Higgs is labeled  $l_H$ , while the other lepton is labeled  $l_T$ , as it is assumed to have come  
413 from the decay of one of the top quarks.  $b_0$  and  $b_1$  are the two b-jets identified by the b-jet  
414 identification algorithm. The Higgs Reco Score and b-jet Reco Score are the outputs of the Higgs  
415 reconstruction algorithm, and the b-jet identification algorithm, respectively.

HT	$M(j_0 j_1)$	$M(j_0 j_1 l_H)$
$M(l_H j_0)$	$M(l_H j_1)$	$p_T(b_0 b_1)$
$p_T(j_0 j_1 l_H)$	$\Delta\phi(j_0 j_1 l_H)(E_T^{\text{miss}})$	$\Delta R(j_0)(j_1)$
$\Delta R(j_0 j_1)(l_H)$	$\Delta R(j_0 j_1 l_H)(l_T)$	$\Delta R(j_0 j_1 l_H)(b_0)$
$\Delta R(j_0 j_1 l_H)(b_1)$	$\Delta R(l_H)(j_0)$	$\Delta R(l_H)(b_0)$
$\Delta R(l_H)(b_1)$	$\Delta R(l_T)(b_0)$	$\Delta R(l_T)(b_1)$
$\Delta R(b_0)(b_1)$	Higgs Reco Score	jet $\eta$ 0
jet $\eta$ 1	jet Phi 0	jet Phi 1
jet $p_T$ 0	jet $p_T$ 1	Lepton $\eta$ H
Lepton $\phi$ H	Lepton $p_T$ H	Lepton $p_T$ T
$E_T^{\text{miss}}$	nJets	b-jet Reco Score
b-jet $p_T$ 0	b-jet $p_T$ 1	

Table 13: Input features for reconstructing the Higgs  $p_T$  spectrum for 2ISS events

416 The optimal neural network architecture for this channel is found to consist of 7 hidden layers with  
417 60 nodes each. The input data set includes 1.2 million events, 10% of which is used for testing,  
418 the other 90% for training. Training is found to converge after around 150 epochs.

419 To evaluate the performance of the model, the predicted  $p_T$  spectrum is compared to the truth  
420 Higgs  $p_T$  in Figure 5.16. In order to visualize the model performance more clearly, in (a) of that  
421 figure, the color of each point is determined by Kernel Density Estimation (KDE). The color  
422 shown represents the logarithm of the output from KDE, to counteract the large number of low  
423  $p_T$  events. For that same reason, each column of the histogram shown in (b) of Figure 5.16 is  
424 normalized to unity. This plot therefore demonstrates what the model predicts for each slice of  
425 truth  $p_T$ .

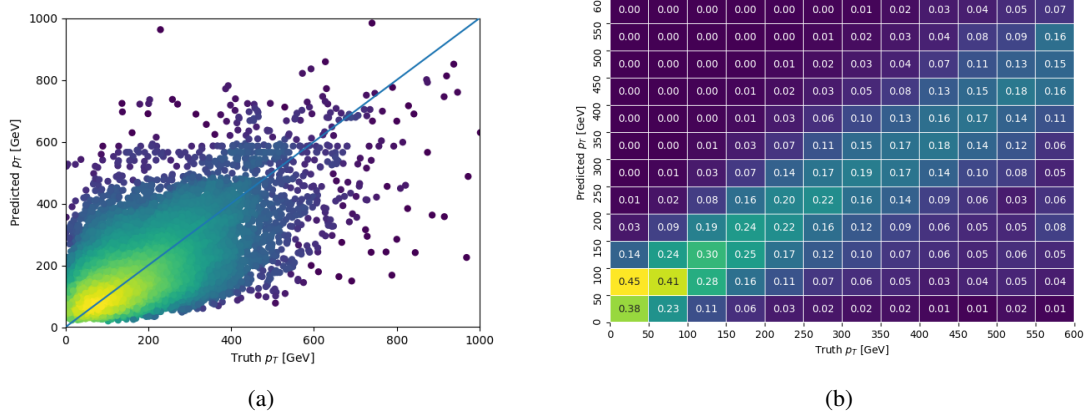


Figure 5.16: The regressed Higgs momentum spectrum as a function of the truth  $p_T$  for 2lSS  $t\bar{t}H$  events in (a) a scatterplot, where the color of each point represents the log of the point density, based on Gaussian Kernal Density Estimation, and (b) a histogram where each column has been normalized to one.

426 We are also interested in how well the model distinguishes between events with  $p_T < 150$  GeV  
 427 and  $> 150$  GeV. Figure 5.17 demonstrates the NN output for high and low  $p_T$  events based on this  
 428 cutoff.

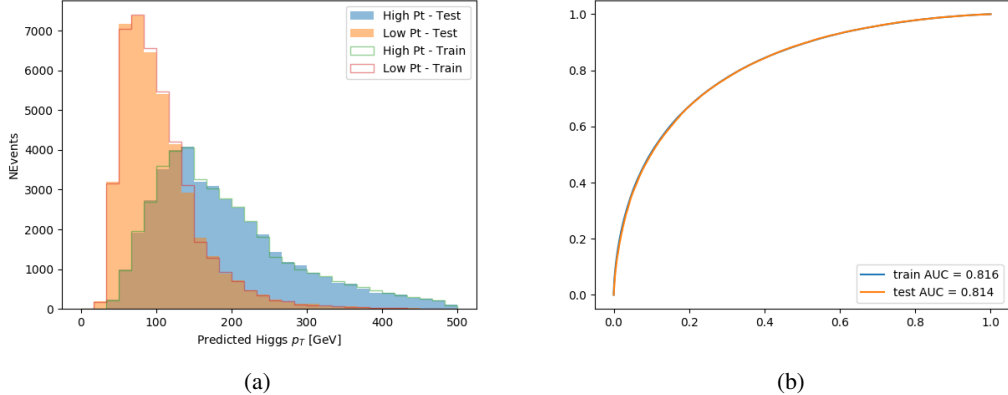


Figure 5.17: (a) shows the reconstructed Higgs  $p_T$  for 2lSS events with truth  $p_T > 150$  GeV and  $< 150$  GeV, while (b) shows the ROC curve for those two sets of events.

### 429 5.5.2 3l Semi-leptonic Channel

430 The following input features are used to predict the Higgs  $p_T$  for events in the 3lS channel:

HT jets	MET	$M(j_0 j_1)$
$M(j_0 j_1 l_H)$	$M(j_0 j_1 l_{T0})$	$M(j_0 j_1 l_{T1})$
$M(j_0 j_1 b_0)$	$M(j_0 j_1 b_1)$	$M(b_0 l_{T0})$
$M(b_0 l_{T1})$	$M(b_1 l_{T0})$	$M(b_1 l_{T1})$
$\Delta\phi(j_0 j_1 l_H)(E_T^{\text{miss}})$	$\Delta R(j_0)(j_1)$	$\Delta R(j_0 j_1)(l_H)$
$\Delta R(j_0 j_1)(l_{T1})$	$\Delta R(j_0 j_1)(b_0)$	$\Delta R(j_0 j_1)(b_1)$
$\Delta R(j_0 j_1 l_H)(l_{T0})$	$\Delta R(j_0 j_1 l_H)(l_{T1})$	$\Delta R(j_0 j_1 l_H)(b_0)$
$\Delta R(j_0 j_1 l_H)(b_1)$	$\Delta R(l_H)(j_0)$	$\Delta R(l_H)(j_1)$
$\Delta R(l_H)(l_{T1})$	$\Delta R(l_{T0})(l_{T1})$	$\Delta R(l_{T0})(b_0)$
$\Delta R(l_{T0})(b_1)$	$\Delta R(l_{T1})(b_0)$	$\Delta R(l_{T1})(b_1)$
higgsScore	jet $\eta$ 0	jet $\eta$ 1
jet $\phi$ 0	jet $\phi$ 1	jet $p_T$ 0
jet $p_T$ 1	Lepton $\eta$ H	Lepton $\phi$ H
Lepton $p_T$ H	Lepton $p_T$ T0	Lepton $p_T$ T1
nJets	topScore	b-jet $p_T$ 0
b-jet $p_T$ 1		

Table 14: Input features for reconstructing the Higgs  $p_T$  spectrum for 3lS events

Again,  $j_0$  and  $j_1$  are the two jets identified as Higgs decay products, ordered by  $p_T$ . The lepton identified as originating from the Higgs is labeled  $l_H$ , while the other two leptons are labeled  $l_{T0}$  and  $l_{T1}$ .  $b_0$  and  $b_1$  are the two b-jets identified by the b-jet identification algorithm. The Higgs Reco Score and b-jet Reco Score are the outputs of the Higgs reconstruction algorithm, and the b-jet identification algorithm, respectively.

The optimal neural network architecture for this channel is found to consist of 7 hidden layers with 80 nodes each. The input data set includes one million events, 10% of which is used for testing, the other 90% for training. Training is found to converge after around 150 epochs.

To evaluate the performance of the model, the predicted  $p_T$  spectrum is compared to the truth Higgs  $p_T$  in Figure 5.18. Once again, (a) of 5.18 shows a scatterplots of predicted vs truth  $p_T$ , where the color of each point corresponds to the log of the relative KDE at that point. Each column of the histogram in (b) is normalized to unity, to better demonstrate the output of the NN for each slice of truth  $p_T$ .

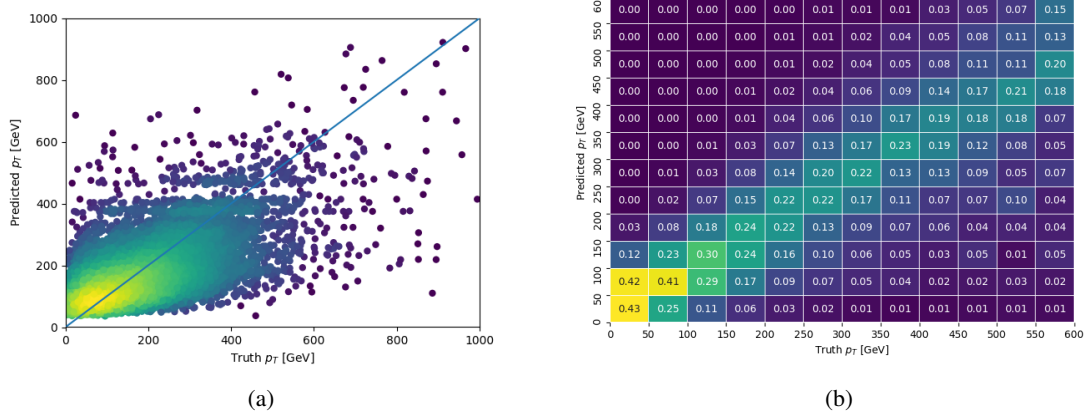


Figure 5.18: The regressed Higgs momentum spectrum as a function of the truth  $p_T$  for 3lS  $t\bar{t}H$  events in (a) a scatterplot, where the color of each point represents the log of the point density, based on Gaussian Kernal Density Estimation, and (b) a histogram where each column has been normalized to one.

444 Figure 5.19 shows (a) the output of the NN for events with truth  $p_T$  less than and greater than  
 445 150 GeV and (b) the ROC curve demonstrating how well the NN distinguishes high and low  $p_T$   
 446 events.

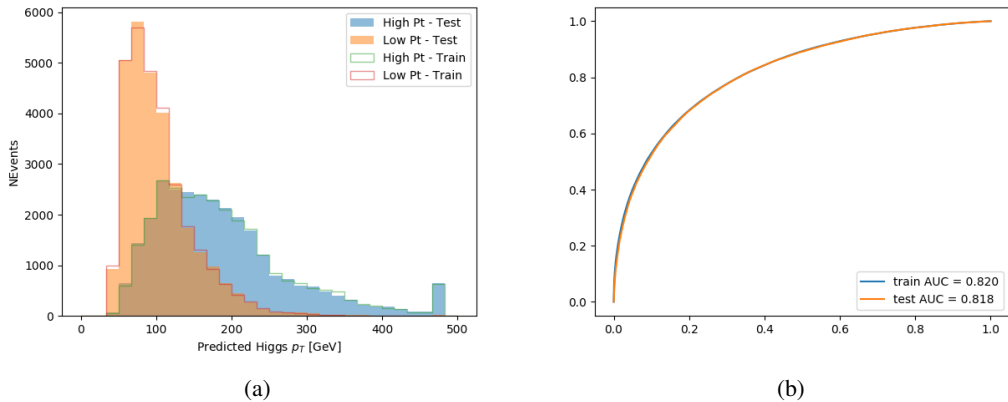


Figure 5.19: (a) shows the reconstructed Higgs  $p_T$  for 3lS events with truth  $p_T > 150$  GeV and  $< 150$  GeV, while (b) shows the ROC curve for those two sets of events.

---

**447 5.5.3 3l Fully-leptonic Channel**

448 The features listed in 15 are used to construct a model for predictin the Higgs  $p_T$  for 3lF events.

HT	$M(l_{H0}l_{H1})$	$M(l_{H0}l_T)$
$M(l_{H0}b_0)$	$M(l_{H0}b_1)$	$M(l_{H1}l_T)$
$M(l_{H1}b_0)$	$M(l_{H1}b_1)$	$\Delta R(l_{H0})(l_{H1})$
$\Delta R(l_{H0})(l_T)$	$\Delta R(l_{H0}l_{H1})(l_T)$	$\Delta R(l_{H0}l_T)(l_{H1})$
$\Delta R(l_{H1})(l_T)$	$\Delta R(l_{H0}b_0)$	$\Delta R(l_{H0}b_1)$
$\Delta R(l_{H1}b_1)$	$\Delta R(l_{H1}b_0)$	higgsScore
Lepton $\eta$ $H_0$	Lepton $\eta$ $H_1$	Lepton $\eta$ T
Lepton $p_T$ $H_0$	Lepton $p_T$ $H_1$	Lepton $p_T$ T
$E_T^{\text{miss}}$	topScore	b-jet $p_T$ 0
b-jet $p_T$ 1		

Table 15: Input features for reconstructing the Higgs  $p_T$  spectrum for 3lF events

449  $l_{H0}$  and  $l_{H1}$  respresent the two leptons identified by the Higgs reconstruction model as originating  
 450 from the Higgs, while  $l_T$  is the other lepton in the event. The Higgs Reco Score and b-jet Reco  
 451 Score are the outputs of the Higgs reconstruction algorithm, and b-jet identification algorithm,  
 452 respectively.

453 The optimal neural network architecture for this channel is found to consist of 5 hidden layers  
 454 with 40 nodes each. The inputdata set includes 400,000 events, 10% of which is used for testing,  
 455 the other 90% for training. Training is found to converge after around 150 epochs.

456 The predicted transverse momentum, as a function of the truth  $p_T$ , is shown in Figure 5.20.

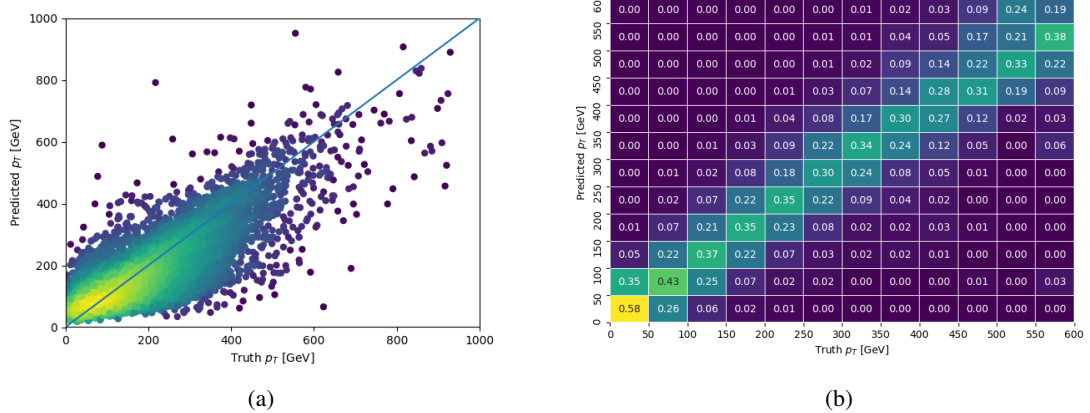


Figure 5.20: The regressed Higgs momentum spectrum as a function of the truth  $p_T$  for 3lF  $t\bar{t}H$  events in (a) a scatterplot, where the color of each point represents the log of the point density, based on Gaussian Kernel Density Estimation, and (b) a histogram where each column has been normalized to one.

457 When split into high and low  $p_T$ , based on a cutoff of 150 GeV, the

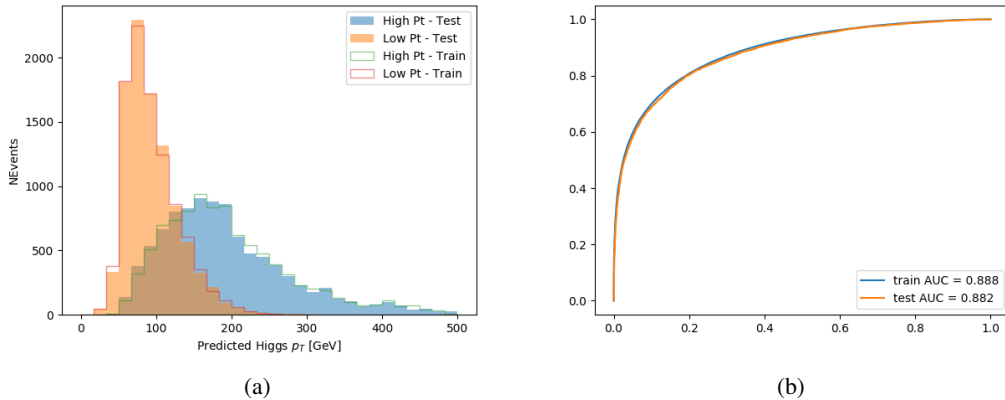


Figure 5.21: (a) shows the reconstructed Higgs  $p_T$  for 3lF events with truth  $p_T > 150$  GeV and  $< 150$  GeV, while (b) shows the ROC curve for those two sets of events.

## 458 5.6 3l Decay Mode

459 In the 3l channel, there are two possible ways for the Higgs to decay, both involving intermediate  
460 W boson pairs: Either both W bosons decay leptonically, in which case the reconstructed decay  
461 consists of two leptons (referred as the fully-leptonic 3l channel), or one W decays leptonically

462 and the other hadronically, giving two jets and one lepton in the final state (referred to as the  
 463 semi-leptonic 3l channel). In order to accurately reconstruct the Higgs, it is necessary to identify  
 464 which of these decays took place for each 3l event.

465 The kinematics of each event, along with the output scores of the Higgs and top reconstruction  
 466 algorithms, are used to distinguish these two possible decay modes. The particular inputs used  
 467 are listed in Table 16.

HT jets	$M(l_0 t_0)$	$M(l_0 t_1)$
$M(l_1 t_0)$	$M(l_1 t_1)$	$M(l_0 l_1)$
$M(l_0 l_2)$	$M(l_1 l_2)$	$\Delta R(l_0 t_0)$
$\Delta R(l_0 t_1)$	$\Delta R(l_1 t_0)$	$\Delta R(l_1 t_1)$
$\Delta R(l_0 l_1)$	$\Delta R(l_0 l_2)$	$\Delta R(l_1 l_2)$
Lepton $\eta$ 0	Lepton $\eta$ 1	Lepton $\eta$ 2
Lepton $\phi$ 0	Lepton $\phi$ 1	Lepton $\phi$ 2
Lepton $p_T$ 0	Lepton $p_T$ 1	Lepton $p_T$ 2
$E_T^{\text{miss}}$	nJets	nJets OR DL1r 60
nJets OR DL1r 85	score3lF	score3lS
topScore	total charge	

Table 16: Input features used to distinguish semi-leptonic and fully-leptonic Higgs decays in the 3l channel.

468 Here  $l_0$  is the opposite charge lepton,  $l_1$  and  $l_2$  are the two SS leptons order by  $\Delta R$  from lepton 0.  
 469 score3lF and score3lS are the outputs of the 3lS and 3lF Higgs reconstruction algorithms, while  
 470 topScore is the output of the b-jet identification algorithm.

471 A neural network with 5 hidden layers, each with 50 nodes, is trained to distinguish these two  
 472 decay modes. The output of the model is summarized in Figure 5.22.

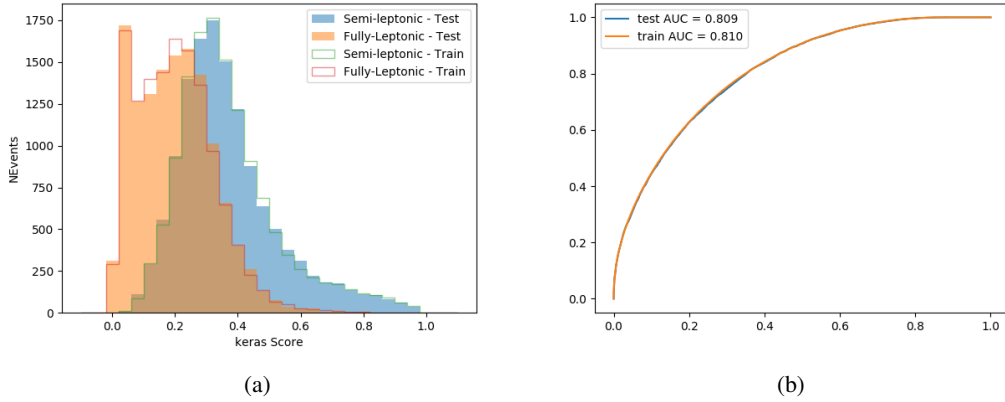


Figure 5.22: (a) shows the output of the decay separation NN for Semi-leptonic (blue) and Fully-leptonic (orange) 3l events, scaled to equal area. (b) shows the ROC curve for those two sets of events.

473 A cutoff of 0.23 is determined to be optimal for separating 3lS and 3lF in the fit.

## 474 6 Signal Region Definitions

475 Events are divided into two channels based on the number of leptons in the final state: one with  
 476 two same-sign leptons, the other with three leptons. The 3l channel includes events where both  
 477 leptons originated from the Higgs boson as well as events where only one of the leptons

### 478 6.1 Pre-MVA Event Selection

479 A preselection is applied to define orthogonal analysis channels based on the number of leptons  
 480 in each event. For the 2lSS channel, the following preselection is used:

- 481 • Two very tight, same-charge, light leptons with  $p_T > 20$  GeV
- 482 •  $\geq 4$  reconstructed jets,  $\geq 1$  b-tagged jets
- 483 • No reconstructed tau candidates

484 The event yield after the 2lSS preselection has been applied, for MC and data at  $79.8 \text{ fb}^{-1}$ , is  
 485 shown in Table 6.1.

Process	Yield
t̄tH high p <sub>T</sub>	41 ± 5
t̄tH low p <sub>T</sub>	71 ± 8
t̄tW	450 ± 70
t̄t(Z/γ*)	91 ± 11
t̄ll low mass	10 ± 6
Rare Top	20 ± 12
VV	42 ± 22
tZ	10 ± 5
QMisID	44.7 ± 2.7
Fakes int. conv	47 ± 26
Fakes ext. conv	46 ± 44
Fakes HF e	45 ± 23
Fakes HF μ	250 ± 50
Three top	2.2 ± 1.1
Four top	5.64 ± 0.31
t̄tWW	10.9 ± 0.6
tW	0.0 ± 0.0
WtZ	9.1 ± 0.8
VVV	0.30 ± 0.05
VH	0.6 ± 1.0
Total	1170 ± 120
Data	1108

Table 17: Yields of the 2lSS preselection region

486 Figure 6.1. Good general agreement is found.

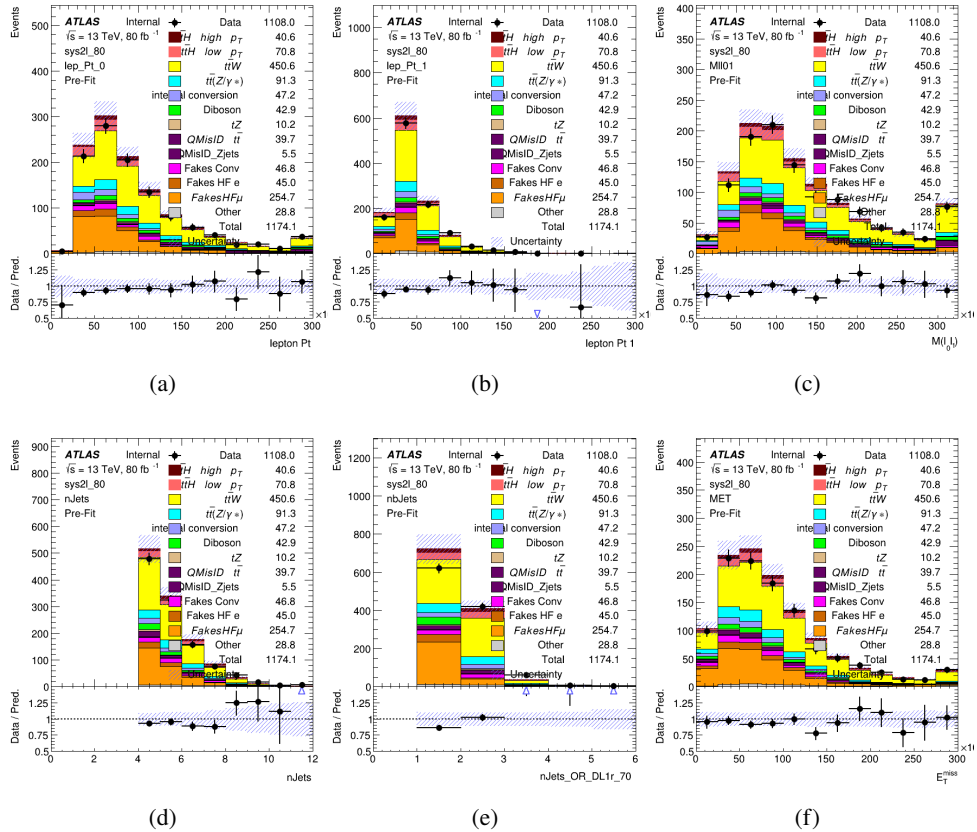


Figure 6.1: Data/MC comparisons of the 2LSS pre-selection region. (a) and (b) show the  $p_T$  of leptons 0 and 1, (c) shows the invariant mass of lepton 0 and 1, (d) shows the jet multiplicity, (e) the b-tagged jet multiplicity, and (f) the missing transverse energy.

For the 3l channel, the following selection is applied:

- Three light leptons with total charge  $\pm 1$
- Same charge leptons are required to be very tight, with  $p_T > 20 \text{ GeV}$
- Opposite charge lepton must be loose, with  $p_T > 10 \text{ GeV}$
- $\geq 2$  reconstructed jets,  $\geq 1$  b-tagged jets
- No reconstructed tau candidates
- $|M(l^+l^-) - 91.2 \text{ GeV}| > 10 \text{ GeV}$  for all opposite-charge, same-flavor lepton pairs

The event yield after the 3l preselection has been applied, for MC and data at  $79.8 \text{ fb}^{-1}$ , is shown in Table 6.1.

Process	Yield
t̄tH high p <sub>T</sub>	20.5 ± 2.3
t̄tH low p <sub>T</sub>	33.6 ± 3.8
t̄tW	138 ± 18
t̄tZ/γ	80 ± 9
t̄tlowmass	3.5 ± 2.0
rareTop	22 ± 12
VV	39 ± 19
tZ	9.2 ± 4.5
QMisID	1.8 ± 0.6
Fakes int. conv	31 ± 17
Fakes ext. conv	14 ± 11
Fakes HF e	20 ± 10
Fakes HF μ	102 ± 22
Three top	0.96 ± 0.48
Four top	6.17 ± 0.35
t̄tWW	5.46 ± 0.33
tW	0.0 ± 0.0
WtZ	8.7 ± 0.6
VVV	0.81 ± 0.11
VH	0.0 ± 0.0
Total	512 ± 48
Data	535

Table 18: Yields of the 3l preselection region.

Table 19: Yields of the 3l preselection region.

<sup>496</sup> Comparisons of kinematic distributions for data and MC in this region are shown in Figure 6.2.

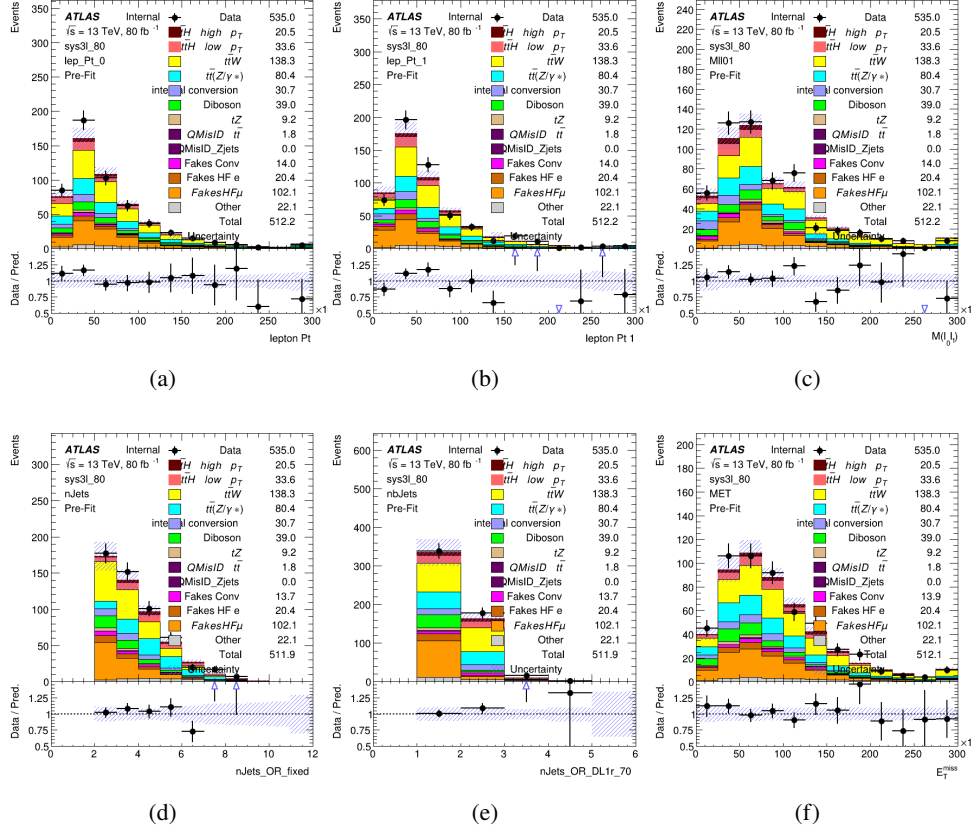


Figure 6.2: Data/MC comparisons of the 3l pre-selection region. (a) and (b) show the  $p_T$  of leptons 0 and 1, (c) shows the invariant mass of lepton 0 and 1, (d) shows the jet multiplicity, (e) the b-tagged jet multiplicity, and (f) the missing transverse energy.

## 6.2 Event MVA

Separate multi-variate analysis techniques (MVAs) are used in order to distinguish signal events from background for each analysis channel - 2lSS, 3l semi-leptonic (3lS), and 3l fully leptonic (3lF). Here events with three leptons are split into 3lS and 3lF based on the model described in 5.6. In particular, Boosted Decision Tree (BDT) algorithms are produced with XGBoost [xgboost] and are trained using the kinematics of signal and background events derived from Monte Carlo simulations. Events are weighted in the BDT training by the weight of each Monte Carlo event.

Because the background composition differs for events with a high reconstructed Higgs  $p_T$  compared to events with low reconstructed Higgs  $p_T$ , separate MVAs are produced for high and low  $p_T$  regions. This is found to provide better significance than attempting to build an inclusive model, as demonstrated in appendix B.2. A cutoff of 150 GeV is used. This gives a total of 6 background rejection MVAs - explicitly, 2lSS high  $p_T$ , 2lSS low  $p_T$ , 3lS high  $p_T$ , 3lS low  $p_T$ , 3lF high  $p_T$ , and 3lF low  $p_T$ .

<sup>510</sup> The following features are used in both the high and low  $p_T$  2lSS BDTs:

HT	$M(\text{lep}, E_T^{\text{miss}})$	$M(l_0 l_1)$
binHiggs $p_T$ 2lSS	$\Delta R(l_0)(l_1)$	diLepton type
higgsRecoScore	jet $\eta$ 0	jet $\eta$ 1
jet $\phi$ 0	jet $\phi$ 1	jet $p_T$ 0
jet $p_T$ 1	Lepton $\eta$ 0	Lepton $\eta$ 1
Lepton $\phi$ 0	Lepton $\phi$ 1	Lepton $p_T$ 0
Lepton $p_T$ 1	$E_T^{\text{miss}}$	$\min \Delta R(l_0)(\text{jet})$
$\min \Delta R(l_1)(\text{jet})$	$\min \Delta R(\text{Lepton})(\text{bjet})$	mjjMax frwdJet
nJets	nJets OR DL1r 60	nJets OR DL1r 70
nJets OR DL1r 85	topRecoScore	

Table 20: Input features used to distinguish signal and background events in the 2lSS channel.

<sup>511</sup> While for each of the 3l BDTs, the features listed below are used for training:

$M(\text{lep}, E_T^{\text{miss}})$	$M(l_0 l_1)$	$M(l_0 l_1 l_2)$
$M(l_0 l_2)$	$M(l_1 l_2)$	binHiggs $p_T$ 3lF
binHiggs $p_T$ 3lS	$\Delta R(l_0)(l_1)$	$\Delta R(l_0)(l_2)$
$\Delta R(l_1)(l_2)$	decayScore	higgsRecoScore3lF
higgsRecoScore3lS	jet $\eta$ 0	jet $\eta$ 1
jet $\phi$ 0	jet $\phi$ 1	jet $p_T$ 0
jet $p_T$ 1	Lepton $\eta$ 0	Lepton $\eta$ 1
Lepton $\eta$ 2	Lepton $\phi$ 0	Lepton $\phi$ 1
Lepton $\phi$ 2	Lepton $p_T$ 0	Lepton $p_T$ 1
Lepton $p_T$ 2	$E_T^{\text{miss}}$	$\min \Delta R(l_0)(\text{jet})$
$\min \Delta R(l_1)(\text{jet})$	$\min \Delta R(l_2)(\text{jet})$	$\min \Delta R(\text{Lepton})(\text{bjet})$
mjjMax frwdJet	nJets	nJets OR DL1r 60
nJets OR DL1r 70	nJets OR DL1r 85	topScore

Table 21: Input features used to distinguish signal and background events in the 3l channel.

<sup>512</sup> Modelling of each of these input features is verified in Appendix B.2 by comparing data and MC for  $79.8 \text{ fb}^{-1}$ . The BDTs are produced with a maximum tree depth of 6, using AUC as the target loss function. The BDT response distribution and ROC curve for each model is shown in Figures [6.3-6.5](#).

## 2LSS

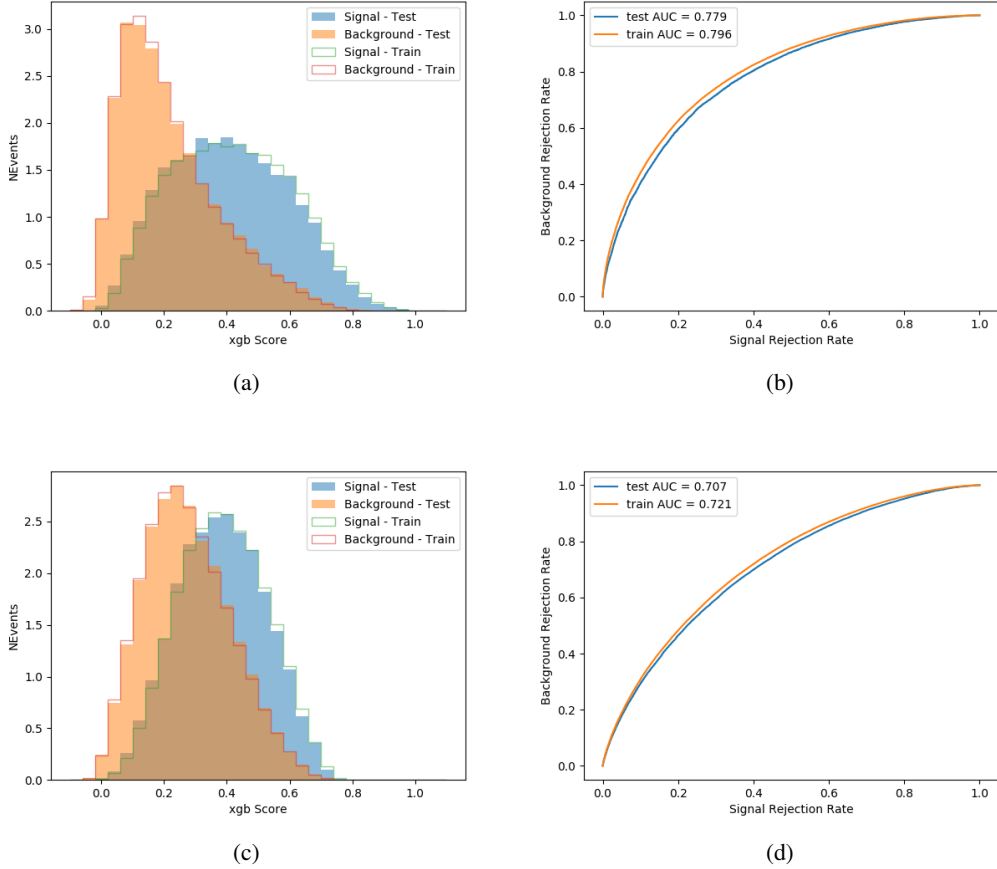


Figure 6.3: Output BDT scores of training and testing data for signal (blue) and background (orange) for 2LSS events with (a) high regressed Higgs  $p_T$  and (b) low regressed Higgs  $p_T$ . (b) and (d) show the ROC curve for the 2LSS high and low  $p_T$  models, respectively.

### 3l - Semileptonic

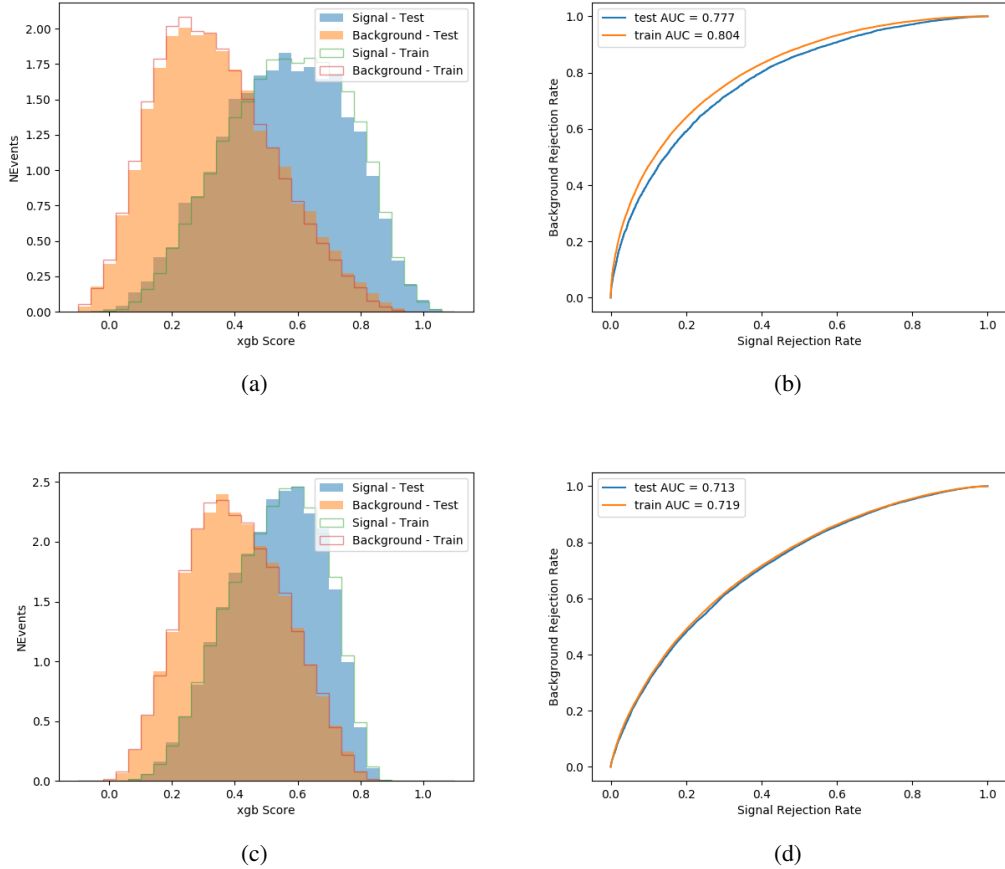


Figure 6.4: Output BDT scores of training and testing data for signal (blue) and background (orange) for 3lS events with (a) high regressed Higgs  $p_T$  and (b) low regressed Higgs  $p_T$ . (b) and (d) show the ROC curve for the 3lS high and low  $p_T$  models, respectively.

### 3l - Fully Leptonic

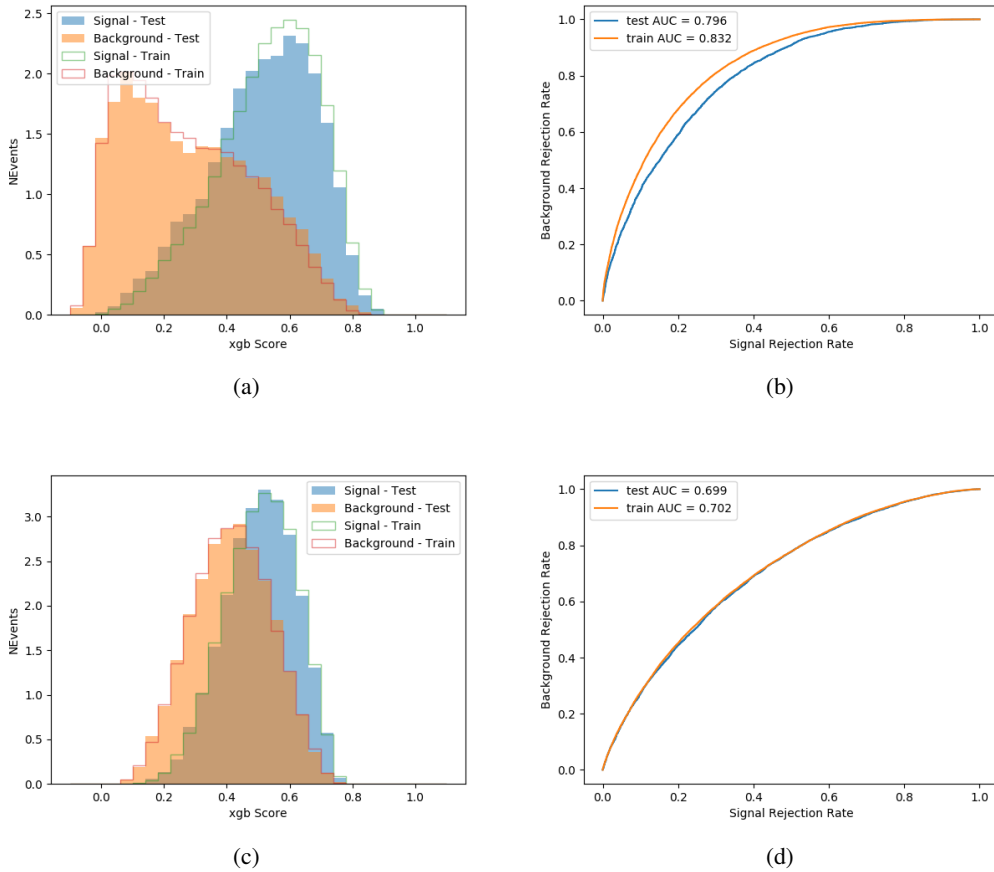


Figure 6.5: Output BDT scores of training and testing data for signal (blue) and background (orange) for 3lF events with (a) high regressed Higgs  $p_T$  and (b) low regressed Higgs  $p_T$ . (b) and (d) show the ROC curve for the 3lF high and low  $p_T$  models, respectively.

516     Output distributions of each MVA, comparing MC predictions to data at  $79.8 \text{ fb}^{-1}$  are shown in  
517     figures 6.6-6.2.

### 518     6.3 Signal Region Definitions

519     Once pre-selection has been applied, channels are further refined based on the MVAs described  
520     above. The output of the model described in Section 5.6 is used to separate the three channel into  
521     two - Semi-leptonic and Fully-leptonic - based on the predicted decay mode of the Higgs boson.  
522     This leaves three orthogonal signal regions - 2lSS, 3lS, and 3lF.

## High $p_T$ Background Rejection BDTs

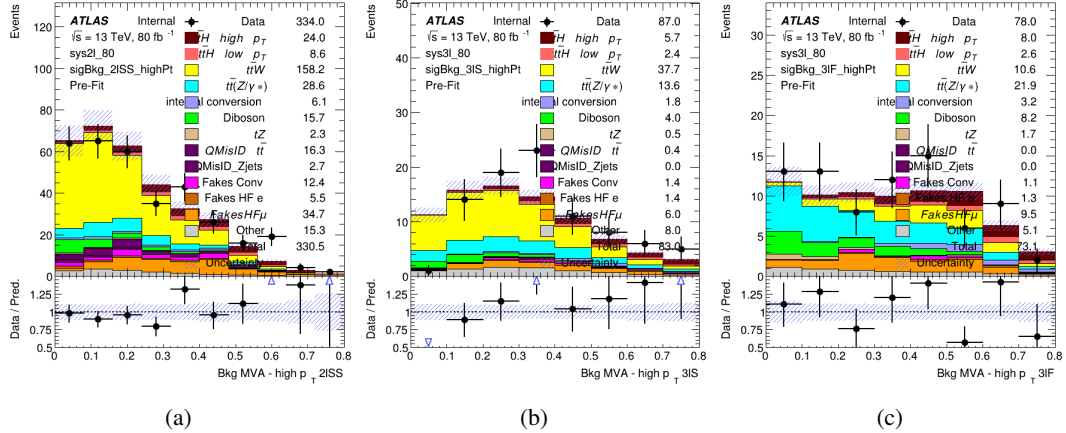


Figure 6.6: Output score of the high  $p_T$  BDTs in the (a) 2lSS, (b) 3lS, and (c) 3lF channels

## Low $p_T$ Background Rejection BDTs

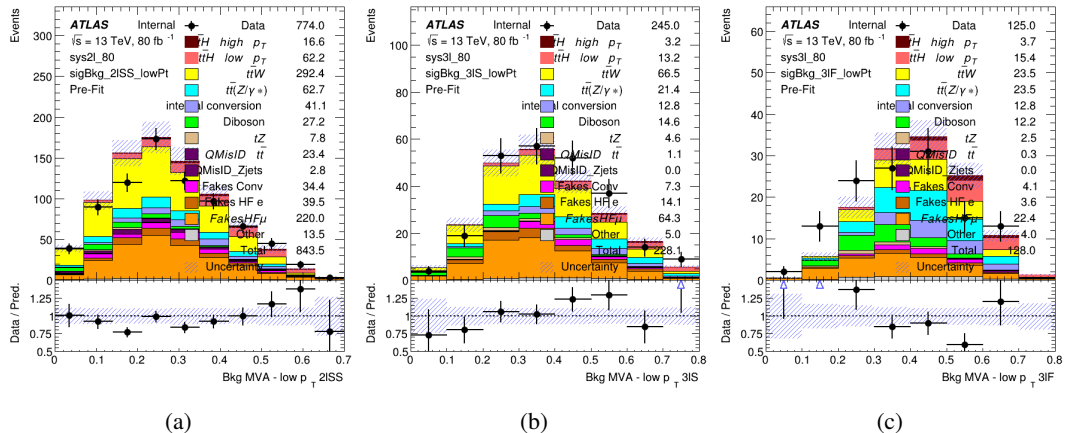


Figure 6.7: Output score of the low  $p_T$  BDTs in the (a) 2lSS, (b) 3lS, and (c) 3lF channels

523 For each event, depending on the number of leptons as well as whether the  $p_T$  of the Higgs is  
 524 predicted to be high ( $> 150$  GeV) or low ( $< 150$  GeV), a cut on the appropriate background  
 525 rejection MVA is applied. The particular cut values, listed in Table 22, are determined by  
 526 maximizing  $S/\sqrt{B}$  in each region.

Channel	BDT Score
2IS high $p_T$	0.36
2IS low $p_T$	0.34
3IS high $p_T$	0.51
3IS low $p_T$	0.43
3IF high $p_T$	0.33
3IF low $p_T$	0.41

Table 22: Cutoff values on background rejection MVA score applied to signal regions.

527 The event preselection and MVA selection listed in Table 22 are used define the three signal  
 528 regions used in the fit. These signal region definitions are summarized in Table 23.

Region	Selection
2IS	Two same charge tight leptons with $p_T > 20$ GeV $N_{\text{jets}} \geq 4$ , $N_{\text{b-jets}} \geq 1$ b-tagged jets Zero $\tau_{\text{had}}$ $H_{p_T}^{\text{pred}} > 150$ GeV and BDT score $> 0.36$ <b>or</b> $H_{p_T}^{\text{pred}} < 150$ GeV and BDT score $> 0.34$
3IS	Three light leptons with total charge $\pm 1$ Two tight SS leptons, $p_T > 20$ GeV One loose OS lepton, $p_T > 10$ GeV $N_{\text{jets}} \geq 2$ , $N_{\text{b-jets}} \geq 1$ b-tagged jets Zero $\tau_{\text{had}}$ $ M(l^+l^-) - 91.2 \text{ GeV}  > 10 \text{ GeV}$ for all OSSF lepton pairs Decay NN Score $< 0.23$ $H_{p_T}^{\text{pred}} > 150$ GeV and BDT score $> 0.51$ <b>or</b> $H_{p_T}^{\text{pred}} < 150$ GeV and BDT score $> 0.43$
3IF	Three light leptons with total charge $\pm 1$ Two tight SS leptons, $p_T > 20$ GeV One loose OS lepton, $p_T > 10$ GeV $N_{\text{jets}} \geq 2$ , $N_{\text{b-jets}} \geq 1$ b-tagged jets Zero $\tau_{\text{had}}$ $ M(l^+l^-) - 91.2 \text{ GeV}  > 10 \text{ GeV}$ for all OSSF lepton pairs Decay NN Score $> 0.23$ $H_{p_T}^{\text{pred}} > 150$ GeV and BDT score $> 0.33$ <b>or</b> $H_{p_T}^{\text{pred}} < 150$ GeV and BDT score $> 0.41$

Table 23: Selection applied to define the three signal regions used in the fit.

529 **7 Systematic Uncertainties**

530 The systematic uncertainties that are considered are summarized in Table 24. These are  
 531 implemented in the fit either as a normalization factors or as a shape variation or both in the signal  
 532 and background estimations. The numerical impact of each of these uncertainties is outlined in  
 533 section 8.

Table 24: Sources of systematic uncertainty considered in the analysis. Some of the systematic uncertainties are split into several components, as indicated by the number in the rightmost column.

Systematic uncertainty	Components
Luminosity	1
Pileup reweighting	1
<b>Physics Objects</b>	
Electron	6
Muon	15
Jet energy scale and resolution	28
Jet vertex fraction	1
Jet flavor tagging	131
$E_T^{\text{miss}}$	3
Total (Experimental)	186
<b>Background Modeling</b>	
Cross section	24
Renormalization and factorization scales	10
Parton shower and hadronization model	2
Shower tune	4
Total (Signal and background modeling)	40
<b>Background Modeling</b>	
Cross section	24
Renormalization and factorization scales	10
Parton shower and hadronization model	2
Shower tune	4
Total (Signal and background modeling)	40
<b>Total (Overall)</b>	226

534 The uncertainty in the combined 2015+2016 integrated luminosity is derived from a calibration  
 535 of the luminosity scale using x-y beam-separation scans performed in August 2015 and May 2016  
 536 [17].

537 The experimental uncertainties are related to the reconstruction and identification of light leptons  
 538 and b-tagging of jets, and to the reconstruction of  $E_T^{\text{miss}}$ . The TOTAL electron ID correlation

539 model is used, corresponding to 1 electron ID systematic. Electron ID is found to be a subleading  
540 systematic that is unconstrained by the fit, making it an appropriate choice for this analysis.

541 The sources which contribute to the uncertainty in the jet energy scale [18] are decomposed into  
542 uncorrelated components and treated as independent sources in the analysis. The CategoryReduction  
543 model is used to account for JES uncertainties, which decomposes the uncertainties into 30  
544 nuisance parameters included in the fit. The SimpleJER model is used to account for jet energy  
545 resolution (JER) uncertainties, and 8 JER uncertainty components included as NPs in the fit.

546 The uncertainties in the b-tagging efficiencies measured in dedicated calibration analyses [19] are  
547 also decomposed into uncorrelated components. The large number of components for b-tagging  
548 is due to the calibration of the distribution of the BDT discriminant.

549 The systematic uncertainties associated with the signal and background processes are accounted  
550 for by varying the cross-section of each process within its uncertainty.

551 The full list of systematic uncertainties considered in the analysis is summarized in Tables 25, 26  
552 and 27.

553

<b>Experimental Systematics on Leptons and <math>E_T^{\text{miss}}</math></b>			
Type	Description	Systematics Name	Application
<b>Trigger</b>			
Scale Factors	Trigger Efficiency	lepSFTrigTight_MU(EL)_SF_Trigger_STAT(SYST)	Event Weight
<b>Muons</b>			
Efficiencies	Reconstruction and Identification	lepSFObjTight_MU_SF_ID_STAT(SYST)	Event Weight
	Isolation	lepSFObjTight_MU_SF_Isol_STAT(SYST)	Event Weight
	Track To Vertex Association	lepSFObjTight_MU_SF_TTVA_STAT(SYST )	Event Weight
$p_T$ Scale	$p_T$ Scale	MUONS_SCALE	$p_T$ Correction
Resolution	Inner Detector Energy Resolution	MUONS_ID	$p_T$ Correction
	Muon Spectrometer Energy Resolution	MUONS_MS	$p_T$ Correction
<b>Electrons</b>			
Efficiencies	Reconstruction	lepSFObjTight_EL_SF_ID	Event Weight
	Identification	lepSFObjTight_EL_SF_Reco	Event Weight
	Isolation	lepSFObjTight_EL_SF_Isol	Event Weight
Scale Factor	Energy Scale	EG_SCALE_ALL	Energy Correction
Resolution	Energy Resolution	EG_RESOLUTION_ALL	Energy Correction
<b><math>E_T^{\text{miss}}</math></b>			
Soft Tracks Terms	Resolution	MET_SoftTrk_ResoPerp	$p_T$ Correction
	Resolution	MET_SoftTrk_ResoPara	$p_T$ Correction
	Scale	MET_SoftTrk_ScaleUp	$p_T$ Correction
	Scale	MET_SoftTrk_ScaleDown	$p_T$ Correction

Table 25: Summary of experimental systematics considered for leptons and  $E_T^{\text{miss}}$ . Includes type, description, name of systematic as used in the fit, and mode of application. The mode of application indicates the systematic evaluation, e.g. as an overall event re-weighting (Event Weight) or rescaling ( $p_T$  Correction).

Experimental Systematics on Jets			
Type	Origin	Systematics Name	Application
Jet Vertex Tagger		JVT	Event Weight
Energy Scale	Calibration Method	JET_21NP_ JET_EffectiveNP_1-19	$p_T$ Correction $p_T$ Correction
	$\eta$ inter-calibration	JET_EtaIntercalibration_Modelling JET_EtaIntercalibration_NonClosure JET_EtaIntercalibration_TotalStat	$p_T$ Correction $p_T$ Correction $p_T$ Correction
	High $p_T$ jets	JET_SingleParticle_HighPt	$p_T$ Correction
	Pile-Up	JET_Pileup_OffsetNPV JET_Pileup_OffsetMu JET_Pileup_PtTerm JET_Pileup_RhoTopology	$p_T$ Correction $p_T$ Correction $p_T$ Correction $p_T$ Correction
	Non Closure	JET_PunchThrough_MC15	$p_T$ Correction
	Flavour	JET_Flavor_Response JET_BJES_Response JET_Flavor_Composition	$p_T$ Correction $p_T$ Correction $p_T$ Correction
Resolution		JET_JER_SINGLE_NP	Event Weight

Table 26: Jet systematics take into account effects of jets calibration method,  $\eta$  inter-calibration, high  $p_T$  jets, pile-up, and flavor response. They are all diagonalised into effective parameters.

Experimental Systematics on b-tagging		
Type	Origin	Systematic Name
Scale Factors	DL1r b-tagger efficiency on b originated jets in bins of $\eta$	DL1r_Continuous_EventWeight_B0-29
	DL1r b-tagger efficiency on c originated jets in bins of $\eta$	DL1r_Continuous_EventWeight_C0-19
	DL1r b-tagger efficiency on light flavoured originated jets in bins of $\eta$ and $p_T$	DL1r_Continuous_EventWeight_Light0-79
	DL1r b-tagger extrapolation efficiency	DL1r_Continuous_EventWeight_extrapolation DL1r_Continuous_EventWeight_extrapolation_from_charm

Table 27: Summary of experimental systematics to be included for b-tagging of jets in the analysis, using the continuous DL1r tagging algorithm. All of the b-tagging related systematics are applied as event weights. From left: type, description, and the name of systematic used in the fit.

554 As mentioned in Section 3.2, a normalization corrections and uncertainties on the estimates of  
 555 non-prompt leptons backgrounds are derived using data driven techniques, described in detail in  
 556 [10]. These are derived from a likelihood fit over various non-prompt enriched control regions,  
 557 targeting several sources of non-prompt light leptons separately: external conversion electrons,  
 558 internal conversion electrons, electrons from heavy flavor decays, and muons from heavy flavor  
 559 decays.

560 The normalization factor and uncertainty applied to each source of non-prompt leptons is  
 561 summarized in Table 7

Processs	Normalization Factor
$NF_e^{\text{ExtCO}}$	$1.70 \pm 0.51$
$NF_e^{\text{IntCO}}$	$0.75 \pm 0.26$
$NF_e^{\text{HF}}$	$1.09 \pm 0.32$
$NF_\mu^{\text{HF}}$	$1.28 \pm 0.17$

Table 28: Normalization factors - with statistical and systematic uncertainties - derived from the fit over fake control regions for each source of non-prompt leptons considered.

562 In addition to those derived from the control regions, several additional uncertainties are assigned  
 563 to the non-prompt lepton background. An additional 25% uncertainty on material conversions is  
 564 assigned, based on the comparison between data and MC in a region where a loose electron fails  
 565 the photon conversion veto. A shape uncertainty of 15% (6%) is assigned to the HF non-prompt

566 electron (muon) background based on a comparison between data and MC where the second  
 567 leading electron (muon) is only required to be loose. As the contribution from light non-prompt  
 568 leptons is small, about 10% percent of the contribution from HF non-prompt leptons, it is derived  
 569 from the agreement between data and simulation in a LF enriched region at low values of the  
 570 non-prompt lepton BDT. The resulting uncertainty is 100%, and is taken to be uncorrelated  
 571 between internal and material conversions.

572 Theoretical uncertainties applied to MC predictions, including cross section, PDF, and scale  
 573 uncertainties are taken from theory calculations for the predominate prompt backgrounds.  
 574 Following the nominal  $t\bar{t}H$  – ML analysis, a 50% uncertainty is applied to Diboson to account  
 575 for the large uncertainty in estimating  $VV + \text{heavy flavor}$ . The other “rare” background processes  
 576 - including  $tZ$ , rare top processes,  $ttWW$ ,  $WtZ$ ,  $VVV$ ,  $tHjb$  and  $WtH$  - are assigned an overall  
 577 50% normalization uncertainty as well. The theory uncertainties applied to the MC estimates are  
 578 summarized in Table 29.

Process	X-section [%]
$t\bar{t} H$ (aMC@NLO+Pythia8)	QCD Scale: $^{+5.8}_{-9.2}$ PDF( $+\alpha_S$ ): $\pm 3.6$
$t\bar{t} Z$ (aMC@NLO+Pythia8)	QCD Scale: $^{+9.6}_{-11.3}$ PDF( $+\alpha_S$ ): $\pm 4$
$t\bar{t} W$ (aMC@NLO+Pythia8)	QCD Scale: $^{+12.9}_{-11.5}$ PDF( $+\alpha_S$ ): $\pm 3.4$
$tHjb$ (aMC@NLO+Pythia8)	QCD Scale: $^{+6.5}_{-14.9}$ PDF( $+\alpha_S$ ): $\pm 3.7$
$WtH$ (aMC@NLO+Pythia8)	QCD Scale: $^{+5.0}_{-6.7}$ PDF( $+\alpha_S$ ): $\pm 6.3$
$VV$ (Sherpa 2.2.1)	$\pm 50$
Others	$\pm 50$

Table 29: Summary of theoretical uncertainties for MC predictions in the analysis.

579 Additional uncertainties to account for  $t\bar{t}W$  mismodelling are also applied. These include a  
 580 “Generator” uncertainty, based on a comparison between the nominal Sherpa 2.2.5 sample, and  
 581 the formerly used aMC@NLO sample, and an “Extra radiation” uncertainty, which includes  
 582 renormalisation and factorisation scale variations of the Sherpa 2.2.5 sample.

## 583 8 Results

584 A maximum likelihood fit is performed simultaneously over the reconstructed Higgs  $p_T$  spectrum  
 585 in the three signal regions, 2IS, 3IS, and 3IF. The signal is split into high and low  $p_T$  samples,  
 586 based on whether the truth  $p_T$  of the Higgs is above or below 150 GeV. The parameters  $\mu_{t\bar{t}H\text{high}p_T}$   
 587 and  $\mu_{t\bar{t}H\text{low}p_T}$ , where  $\mu = \sigma_{\text{observed}}/\sigma_{\text{SM}}$ , are extracted from the fit, signifying the difference

588 between the observed value and the theory prediction. Unblinded results are shown for the 79.8  
 589  $\text{fb}^{-1}$  data set, as well as MC only projections of results using the full Run-2, 139  $\text{fb}^{-1}$  dataset.

590 As described in Section 7, there are 229 systematic uncertainties that are considered as NPs in the  
 591 fit. These NP s are constrained by Gaussian or log-normal probability density functions. The  
 592 latter are used for normalisation factors to ensure that they are always positive. The expected  
 593 number of signal and background events are functions of the likelihood. The prior for each NP is  
 594 added as a penalty term, decreasing the likelihood as it is shifted away from its nominal value.

## 595 8.1 Results - $79.8 \text{ fb}^{-1}$

596 As the data collected from 2015-2017 has been unblinded for  $t\bar{t}H$ -ML channels, representing 79.8  
 597  $\text{fb}^{-1}$ , those events are unblinded. The predicted Higgs  $p_T$  spectrum is fit to data simultaneously  
 598 in each of the three signal regions shown in Figure 8.1.

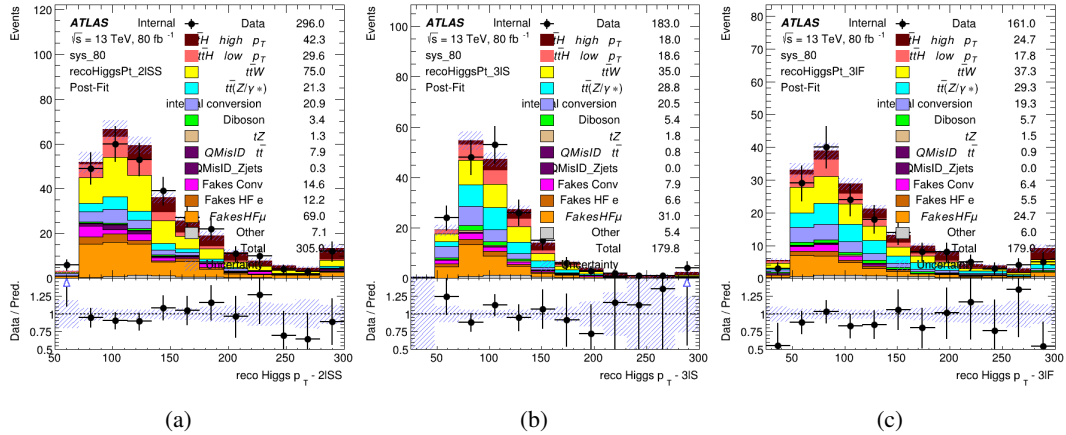


Figure 8.1: Post-fit distributions of the reconstructed Higgs  $p_T$  in the three signal regions, (a) 2ISS, (b) 3IS, and (c) 3IF, for  $79.8 \text{ fb}^{-1}$  of MC

599 A post-fit summary of the fitted regions is shown in Figure 8.2.

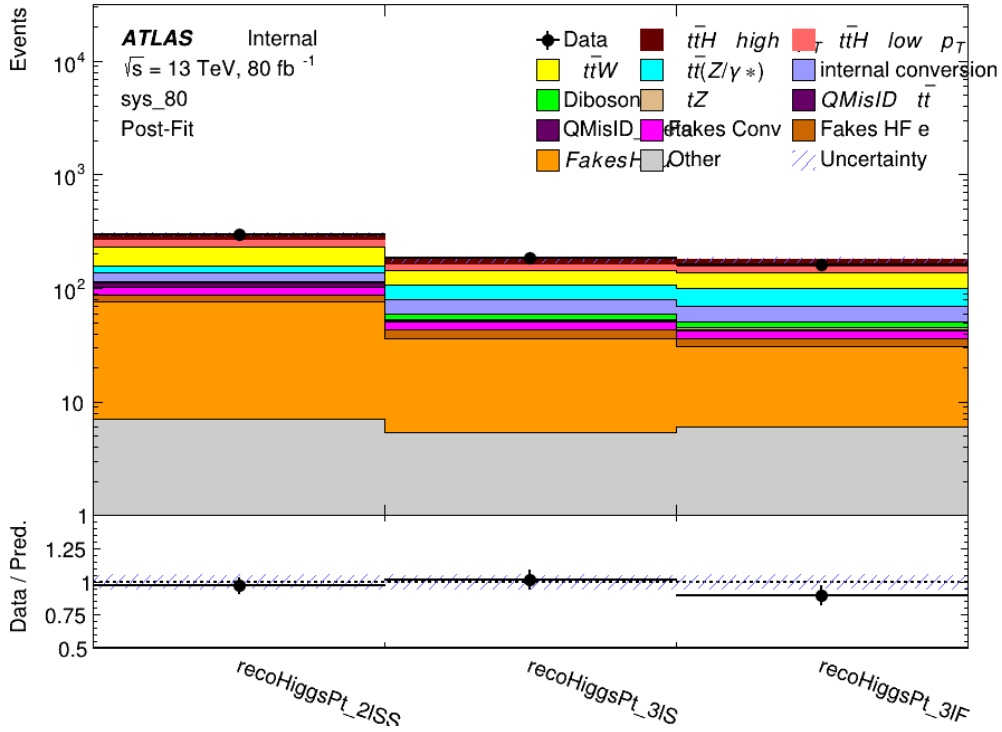


Figure 8.2: Post-fit summary of the yields in each signal region.

600 The measured  $\mu$  values for high and low  $p_T$  Higgs production obtained from the fit are  
 601 shown in 30. A significance of  $1.7\sigma$  is observed for  $t\bar{t}H$  high  $p_T$ , and  $2.1\sigma$  is measured for  
 602  $t\bar{t}H$  low  $p_T$ .

$$\mu_{t\bar{t}H \text{ high } p_T} = 2.1^{+0.62}_{-0.59} (\text{stat})^{+0.40}_{-0.43} (\text{sys})$$

$$\mu_{t\bar{t}H \text{ low } p_T} = 0.83^{+0.39}_{-0.40} (\text{stat})^{+0.51}_{-0.53} (\text{sys})$$

Table 30: Best fit  $\mu$  values for  $t\bar{t}H$  high  $p_T$  and  $t\bar{t}H$  low  $p_T$ , where  $\mu = \sigma_{\text{obs}}/\sigma_{\text{pred}}$

603 The most prominent sources of systematic uncertainty, as measured by their impact on  $\mu_{t\bar{t}H \text{ high } p_T}$ ,  
 604 are summarized in Table 31.

Uncertainty Source	$\Delta\mu$	
Jet Energy Scale	0.25	0.23
t̄H cross-section (QCD scale)	-0.11	0.21
Luminosity	-0.13	0.14
Flavor Tagging	0.14	0.13
t̄W cross-section (QCD scale)	-0.12	0.11
Higgs Branching Ratio	-0.1	0.11
t̄H cross-section (PDF)	-0.07	0.08
Electron ID	-0.06	0.06
Non-prompt Muon Normalization	-0.05	0.06
t̄Z cross-section (QCD scale)	-0.05	0.05
Diboson cross-section	-0.05	0.05
Fake muon modelling	-0.04	0.04
Total	0.40	0.43

Table 31: Summary of the most significant sources of systematic uncertainty on the measurement of t̄H high p<sub>T</sub>.

605 The most significant sources of uncertainty on the measurement of t̄H - low p<sub>T</sub> are shown in  
 606 Table 32.

Uncertainty Source	$\Delta\mu$	
Internal Conversions	-0.26	0.26
Luminosity	-0.16	0.17
Non-prompt Muon Normalization	-0.16	0.16
t̄W cross-section (QCD scale)	-0.17	0.15
Jet Energy Scal	0.15	0.15
Non-prompt Electron Modelling	-0.13	0.14
Flavor Tagging	0.13	0.13
Non-prompt Muon Modelling	-0.12	0.13
Non-prompt Electron Normalization	-0.11	0.11
t̄Z cross-section (QCD scale)	-0.08	0.09
Diboson Cross-section	-0.07	0.07
Total	0.51	0.53

Table 32: Summary of the most significant sources of systematic uncertainty on the measurement of t̄H low p<sub>T</sub>.

607 The ranking and impact of those nuisance parameters with the largest contribution to the overall  
 608 uncertainty is shown in Figure 8.3.

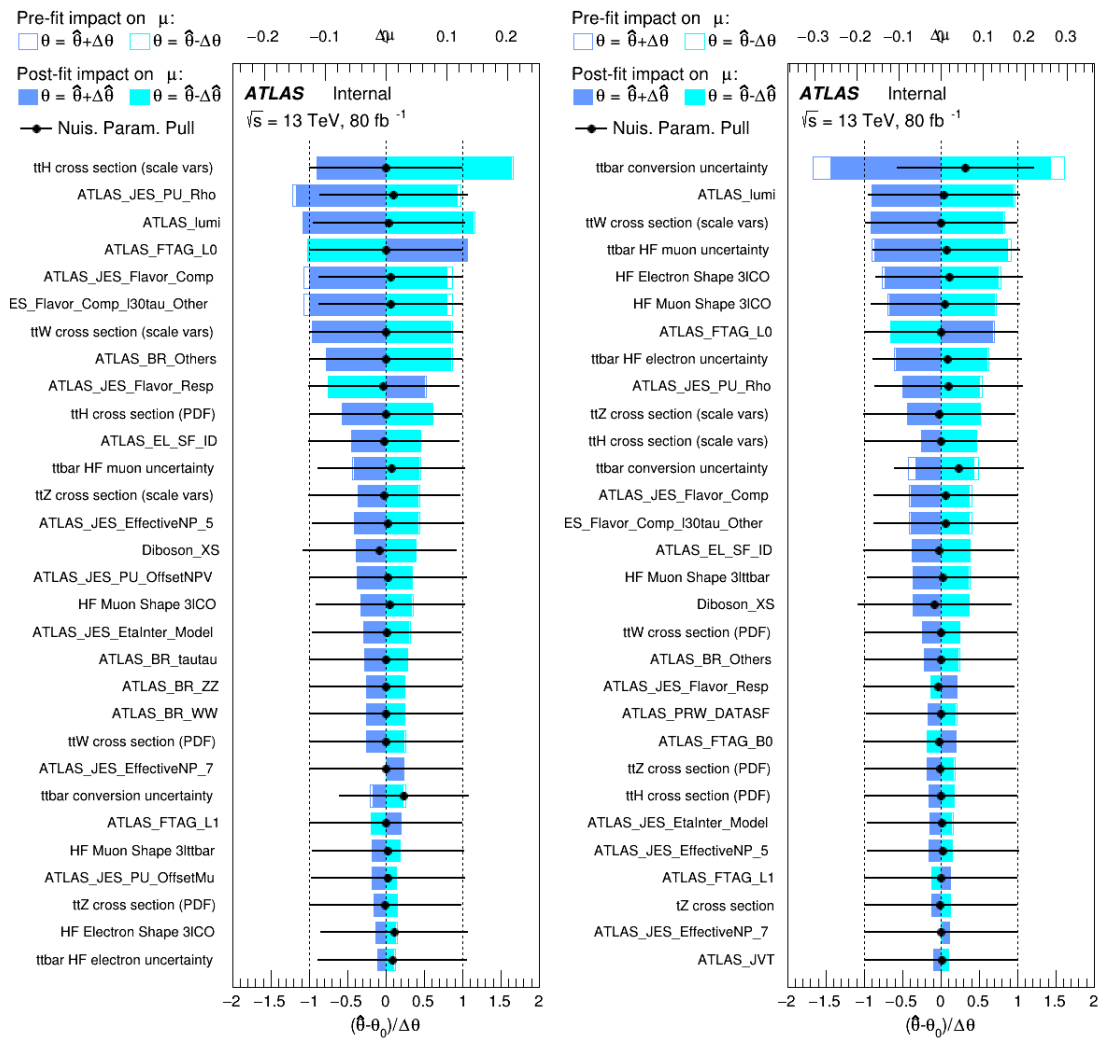


Figure 8.3: Impact of systematic uncertainties on the measurement of high  $p_T$  (left) and low  $p_T$  (right)  $t\bar{t}H$  events

609 The background composition of each of the fit regions is shown in Figure 8.4.

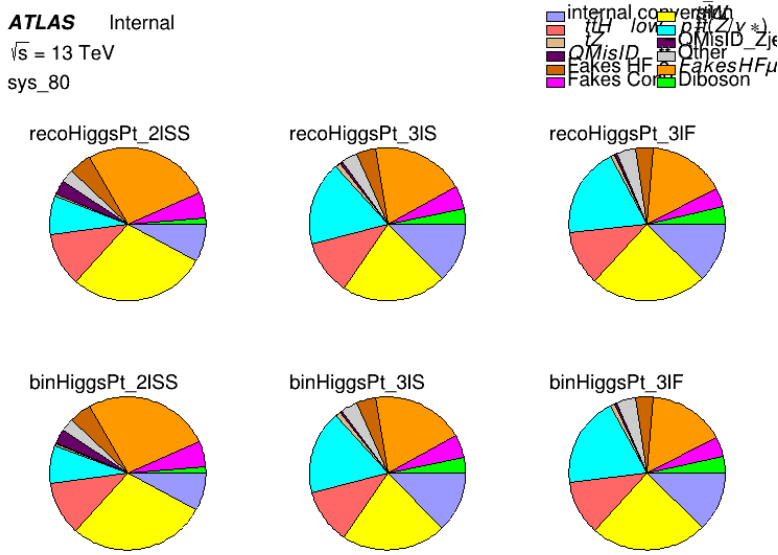
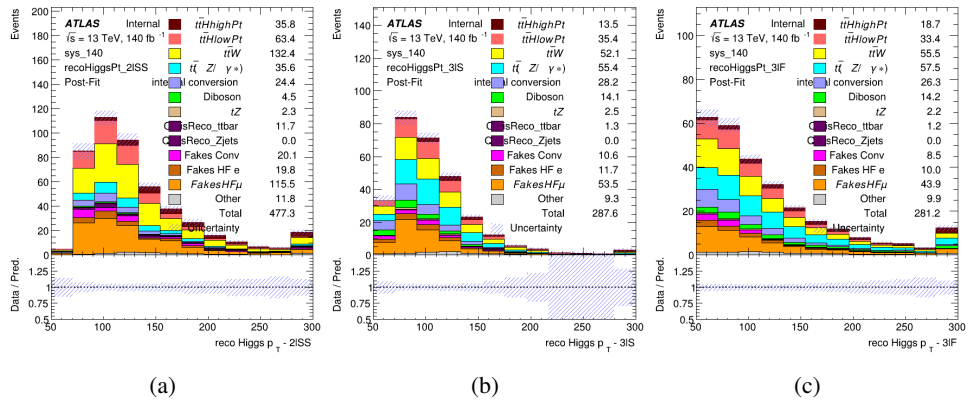


Figure 8.4: Background composition of the fit regions.

## 610 8.2 Projected Results - $139 \text{ fb}^{-1}$

611 As data collected in 2018 has not yet been unblinded for  $t\bar{t}H$  – ML at the time of this note, data  
 612 from that year remains blinded. Instead, an Asimov fit is performed - with the MC prediction  
 613 being used both as the SM prediction as well as the data in the fit - in order to give expected  
 614 results.

Figure 8.5: Blinded post-fit distributions of the reconstructed Higgs  $p_T$  in the three signal regions, (a) 2lSS, (b) 3lS, and (c) 3lF, for  $139 \text{ fb}^{-1}$  of data

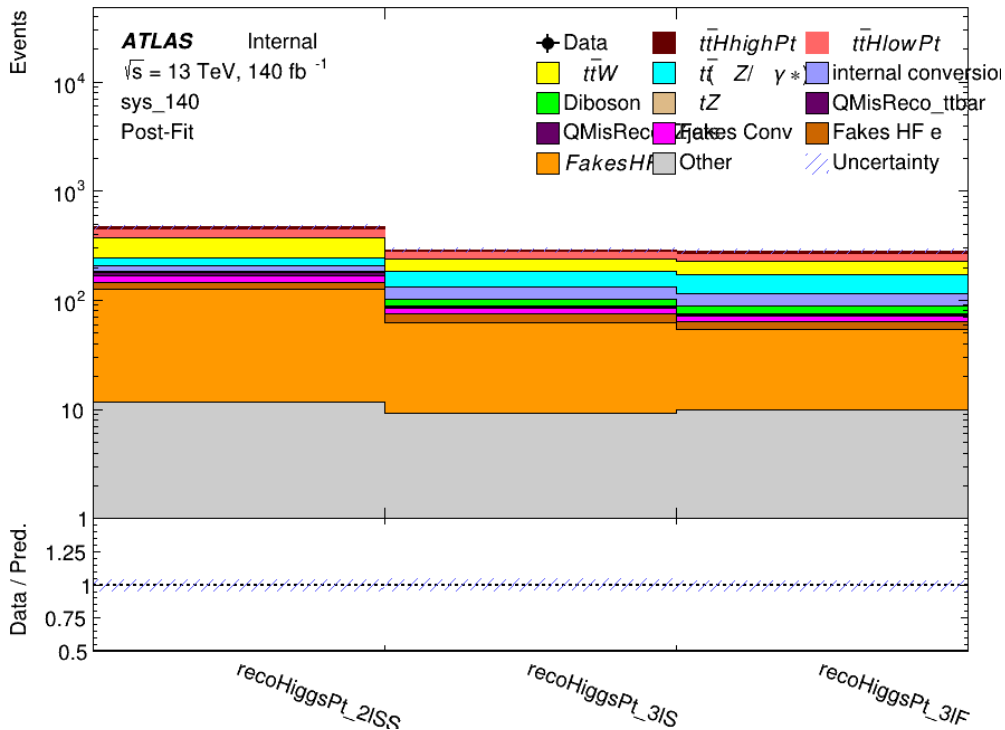


Figure 8.6: Post-fit summary of fit.

615 Projected uncertainties on the  $\mu$  values extracted from the fit for high and low  $p_T$  Higgs are shown  
 616 in 33. A significance of  $2.0\sigma$  is expected for  $t\bar{t}H$  high  $p_T$ , and a projected significance  $2.3\sigma$  is  
 617 extracted for  $t\bar{t}H$  low  $p_T$ .

$$\mu_{t\bar{t}H \text{ high } p_T} = 1.00^{+0.45}_{-0.43} (\text{stat})^{+0.30}_{-0.31} (\text{sys})$$

$$\mu_{t\bar{t}H \text{ low } p_T} = 1.00^{+0.29}_{-0.30} (\text{stat})^{+0.48}_{-0.50} (\text{sys})$$

Table 33: Best fit  $\mu$  values for  $t\bar{t}H$  high  $p_T$  and  $t\bar{t}H$  low  $p_T$ , where  $\mu = \sigma_{\text{obs}}/\sigma_{\text{pred}}$ 

618 The most prominent sources of systematic uncertainty, as measured by their impact on  $\mu_{t\bar{t}H \text{ high } p_T}$ ,  
 619 are summarized in Table 34.

Uncertainty Source	$\Delta\mu$	
Jet Energy Scale	0.19	0.17
t̄W Cross-section (QCD Scale)	-0.12	0.11
Luminosity	-0.1	0.11
Flavor Tagging	0.1	0.1
t̄H Cross-section (QCD Scale)	-0.05	0.1
t̄Z Cross-section (QCD Scale)	-0.05	0.06
Non-prompt Muon Normalization	-0.05	0.05
Higgs Branching Ratio	-0.05	0.05
Diboson Cross-section	-0.04	0.05
Non-prompt Muon Modelling	-0.04	0.04
t̄H Cross-section (PDF)	-0.03	0.04
Electron ID	-0.04	0.04
t̄W Cross-section (PDF)	-0.03	0.03
Total	0.30	0.31

Table 34: Summary of the most significant sources of systematic uncertainty on the measurement of t̄H high p<sub>T</sub>.

620 The most significant sources of systematic uncertainty on t̄H low p<sub>T</sub> are summarized in Table  
 621 [35](#).

Uncertainty Source	$\Delta\mu$	
Internal Conversions	-0.18	0.2
Jet Energy Scale	0.19	0.16
Non-prompt Muon Normalization	-0.16	0.17
Luminosity	-0.15	0.17
t̄W Cross-section (QCD Scale)	-0.17	0.15
Non-prompt Electron Modelling	-0.13	0.14
Non-prompt Muon Modelling	-0.13	0.13
Flavor Tagging	0.13	0.12
Non-prompt Electron Normalization	-0.1	0.11
t̄Z Cross-section (QCD Scale)	-0.07	0.09
t̄H Cross-section (QCD Scale)	-0.05	0.1
Total	0.48	0.50

Table 35: Summary of the most significant sources of systematic uncertainty on the measurement of t̄H low p<sub>T</sub>.

622 The ranking and impact of those nuisance parameters with the largest contribution to the overall  
 623 uncertainty is shown in Figure [8.7](#).

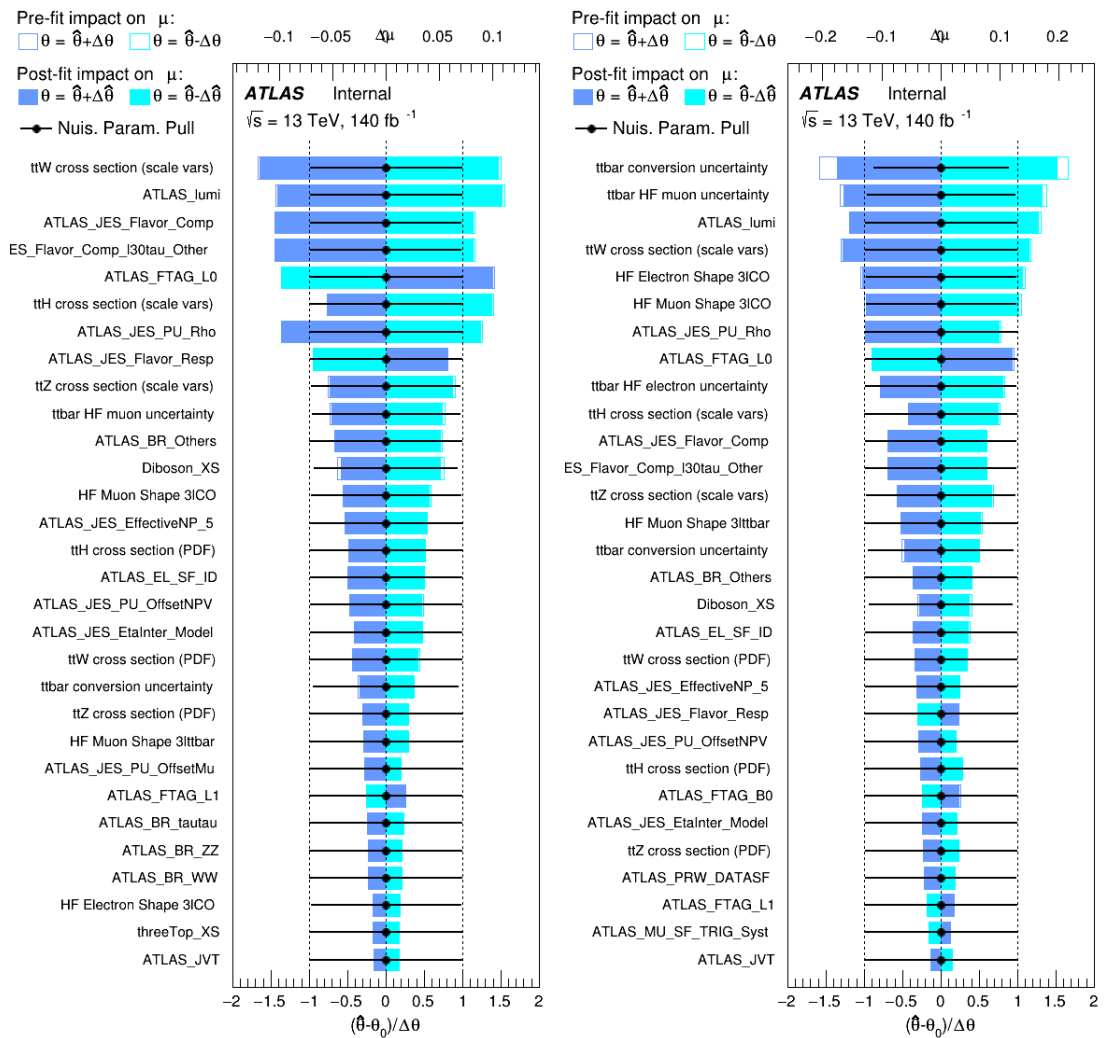


Figure 8.7: Impact of systematic uncertainties on the measurement of high  $p_T$  (left) and low  $p_T$  (right)  $t\bar{t}H$  events

624 The background composition of each of the fit regions is shown in Figure 8.8.

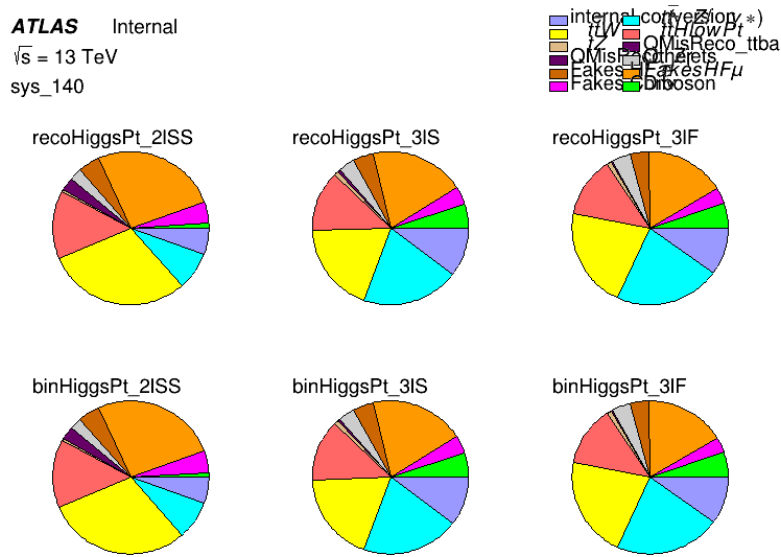


Figure 8.8: Background composition of the fit regions.

## 625 9 Conclusion

626 As search for the effects of dimension-six operators on  $t\bar{t}H$  production is performed. An effective  
 627 field theory approached is used to parametrize the effects of high energy physics on the Higgs  
 628 momentum spectrum. The momentum spectrum is reconstructed using various MVA techniques,  
 629 and the limits on dimension-six operators are limited to X.

## 630 References

- 631 [1] ATLAS Collaboration, *Observation of a new particle in the search for the Standard Model*  
 632 *Higgs boson with the ATLAS detector at the LHC*, *Phys. Lett. B* **716** (2012) 1, arXiv:  
 633 [1207.7214 \[hep-ex\]](https://arxiv.org/abs/1207.7214) (cit. on p. 5).
- 634 [2] B. Dumont, S. Fichet and G. von Gersdorff, *A Bayesian view of the Higgs sector with higher*  
 635 *dimensional operators*, *Journal of High Energy Physics* **2013** (2013), ISSN: 1029-8479,  
 636 URL: [http://dx.doi.org/10.1007/JHEP07\(2013\)065](http://dx.doi.org/10.1007/JHEP07(2013)065) (cit. on p. 5).
- 637 [3] S. Banerjee, S. Mukhopadhyay and B. Mukhopadhyaya, *Higher dimensional operators and*  
 638 *the LHC Higgs data: The role of modified kinematics*, *Physical Review D* **89** (2014), ISSN:  
 639 1550-2368, URL: <http://dx.doi.org/10.1103/PhysRevD.89.053010> (cit. on p. 5).
- 640 [4] R. D. Ball et al., *Parton distributions for the LHC Run II*, *JHEP* **04** (2015) 040, arXiv:  
 641 [1410.8849 \[hep-ph\]](https://arxiv.org/abs/1410.8849) (cit. on p. 7).
- 642 [5] H.-L. Lai et al., *New parton distributions for collider physics*, *Phys. Rev. D* **82** (2010) 074024,  
 643 arXiv: [1007.2241 \[hep-ph\]](https://arxiv.org/abs/1007.2241) (cit. on p. 7).
- 644 [6] S. Frixione, G. Ridolfi and P. Nason, *A positive-weight next-to-leading-order Monte Carlo*  
 645 *for heavy flavour hadroproduction*, *JHEP* **09** (2007) 126, arXiv: [0707.3088 \[hep-ph\]](https://arxiv.org/abs/0707.3088)  
 646 (cit. on p. 7).
- 647 [7] E. Re, *Single-top Wt-channel production matched with parton showers using the POWHEG*  
 648 *method*, *Eur. Phys. J. C* **71** (2011) 1547, arXiv: [1009.2450 \[hep-ph\]](https://arxiv.org/abs/1009.2450) (cit. on p. 7).
- 649 [8] ATLAS Collaboration, *Comparison of Monte Carlo generator predictions from Powheg*  
 650 *and Sherpa to ATLAS measurements of top pair production at 7 TeV*, ATL-PHYS-PUB-  
 651 2015-011, 2015, URL: <https://cds.cern.ch/record/2020602> (cit. on p. 7).
- 652 [9] ATLAS Collaboration, *ATLAS tunes of PYTHIA 6 and Pythia 8 for MC11*, ATL-PHYS-  
 653 PUB-2011-009, 2011, URL: <https://cds.cern.ch/record/1363300> (cit. on p. 7).
- 654 [10] *Evidence for the associated production of the Higgs boson and a top quark pair with*  
 655 *the ATLAS detector*, tech. rep. ATLAS-CONF-2017-077, CERN, 2017, URL: <https://cds.cern.ch/record/2291405> (cit. on pp. 7, 8, 10, 54).
- 656 [11] ATLAS Collaboration, *Electron efficiency measurements with the ATLAS detector using*  
 657 *the 2015 LHC proton–proton collision data*, ATLAS-CONF-2016-024, 2016, URL: <https://cds.cern.ch/record/2157687> (cit. on p. 10).
- 658 [12] ATLAS Collaboration, *Measurement of the muon reconstruction performance of the*  
 659 *ATLAS detector using 2011 and 2012 LHC proton–proton collision data*, *Eur. Phys. J. C*  
 660 **74** (2014) 3130, arXiv: [1407.3935 \[hep-ex\]](https://arxiv.org/abs/1407.3935) (cit. on p. 10).
- 661 [13] ATLAS Collaboration, *Jet Calibration and Systematic Uncertainties for Jets Reconstructed*  
 662 *in the ATLAS Detector at  $\sqrt{s} = 13$  TeV*, ATL-PHYS-PUB-2015-015, 2015, URL: <https://cds.cern.ch/record/2037613> (cit. on p. 11).
- 663 [14] ATLAS Collaboration, *Selection of jets produced in 13 TeV proton–proton collisions with*  
 664 *the ATLAS detector*, ATLAS-CONF-2015-029, 2015, URL: <https://cds.cern.ch/record/2037702> (cit. on p. 11).

- 669 [15] ATLAS Collaboration, *Performance of pile-up mitigation techniques for jets in pp collisions*  
670 *at  $\sqrt{s} = 8 \text{ TeV}$  using the ATLAS detector*, Eur. Phys. J. C **76** (2016) 581, arXiv: [1510.03823](https://arxiv.org/abs/1510.03823) [hep-ex] (cit. on p. 11).
- 672 [16] ATLAS Collaboration, *Performance of missing transverse momentum reconstruction*  
673 *with the ATLAS detector in the first proton–proton collisions at  $\sqrt{s} = 13 \text{ TeV}$* , ATL-  
674 PHYS-PUB-2015-027, 2015, URL: <https://cds.cern.ch/record/2037904> (cit. on  
675 p. 11).
- 676 [17] ATLAS Collaboration, *Luminosity determination in pp collisions at  $\sqrt{s} = 7 \text{ TeV}$  using the*  
677 *ATLAS detector at the LHC*, Eur. Phys. J. C **71** (2011) 1630, arXiv: [1101.2185](https://arxiv.org/abs/1101.2185) [hep-ex]  
678 (cit. on p. 50).
- 679 [18] G. Aad, T. Abajyan, B. Abbott and et al, *Jet energy resolution in proton-proton collisions at*  
680  *$\sqrt{s} = 7 \text{ TeV}$  recorded in 2010 with the ATLAS detector*, The European Physical Journal  
681 C **73** (2013) 2306, ISSN: 1434-6052, URL: <https://doi.org/10.1140/epjc/s10052-013-2306-0> (cit. on p. 51).
- 683 [19] A. Collaboration, *Performance of b -jet identification in the ATLAS experiment*, Journal of  
684 Instrumentation **11** (2016) P04008, URL: <http://stacks.iop.org/1748-0221/11/i=04/a=P04008> (cit. on p. 51).
- 686 [20] R. Narayan et al., *Measurement of the total and differential cross sections of a top-quark*  
687 *antiquark pair in association with a W boson in proton-proton collisions at a centre-of-mass*  
688 *energy of 13 TeV with ATLAS detector at the Large Hadron Collider*, tech. rep. ATL-COM-  
689 PHYS-2020-217, CERN, 2020, URL: <https://cds.cern.ch/record/2712986> (cit. on  
690 p. 68).

**691 List of contributions**

692

# 693 Part I

## 694 Appendices

### 695 A Non-prompt lepton MVA

696 A lepton MVA has been developed to better reject non-prompt leptons than standard cut  
 697 based selections based upon impact parameter, isolation and PID. The name of this MVA is  
 698 `PromptLeptonIso`. The full set of studies and detailed explanation can be found in [20].

699 The decays of  $W$  and  $Z$  bosons are commonly selected by the identification of one or two electrons  
 700 or muons. The negligible lifetimes of these bosons mean that the leptons produced in the decay  
 701 originate from the interaction vertex and are thus labelled “prompt”. Analyses using these light  
 702 leptons impose strict reconstruction quality, isolation and impact parameter requirements to  
 703 remove “fake” leptons. A significant source of the fake light leptons are non-prompt leptons  
 704 produced in decays of hadrons that contain bottom (b) or charm (c) quarks. Such hadrons typically  
 705 have microscopically significant lifetimes that can be detected experimentally.

706 These non-prompt leptons can also pass the tight selection criteria. In analyses that involve top (t)  
 707 quarks, which decay almost exclusively into a  $W$  boson and a b quark, non-prompt leptons from  
 708 the semileptonic decay of bottom and charm hadrons can be a significant source of background  
 709 events. This is particularly the case in the selection of same-sign dilepton and multilepton final  
 710 states.

711 The main idea is to identify non-prompt light leptons using lifetime information associated with a  
 712 track jet that matches the selected light lepton. This lifetime information is computed using tracks  
 713 contained within the jet. Typically, lepton lifetime is determined using the impact parameter of  
 714 the track reconstructed by the inner tracking detector which is matched to the reconstructed lepton.  
 715 Using additional reconstructed charged particle tracks increases the precision of identifying the  
 716 displaced decay vertex of bottom or charm hadrons that produced a non-prompt light lepton.  
 717 The MVA also includes information related to the isolation of the lepton to reject non-prompt  
 718 leptons.

719 `PromptLeptonIso` is a gradient boosted BDT. The training of the BDT is performed on leptons  
 720 selected from the PowHEG+PYTHIA6 non-allhad  $t\bar{t}$  MC sample. Eight variables are used to train  
 721 the BDT in order to discriminate between prompt and non-prompt leptons. The track jets that  
 722 are matched to the non-prompt leptons correspond to jets initiated by b or c quarks, and may  
 723 contain a displaced vertex. Consequently, three of the selected variables are used to identify  
 724 b-tag jets by standard ATLAS flavour tagging algorithms. Two variables use the relationship  
 725 between the track jet and lepton: the ratio of the lepton  $p_T$  with respect to the track jet  $p_T$  and  
 726  $\Delta R$  between the lepton and the track jet axis. Finally three additional variables test whether the  
 727 reconstructed lepton is isolated: the number of tracks collected by the track jet and the lepton  
 728 track and calorimeter isolation variables. Table 36 describes the variables used to train the BDT

729 algorithm. The choice of input variables has been extensively discussed with Egamma, Muon,  
 730 Tracking, and Flavour Tagging CP groups.

Variable	Description
$N_{\text{track}} \text{ in track jet}$	Number of tracks collected by the track jet
$\text{IP2 log}(P_b/P_{\text{light}})$	Log-likelihood ratio between the b and light jet hypotheses with the IP2D algorithm
$\text{IP3 log}(P_b/P_{\text{light}})$	Log-likelihood ratio between the b and light jet hypotheses with the IP3D algorithm
$N_{\text{TrkAtVtx}} \text{ SV + JF}$	Number of tracks used in the secondary vertex found by the SV1 algorithm in addition to the number of tracks from secondary vertices found by the JetFitter algorithm with at least two tracks
$p_T^{\text{lepton}} / p_T^{\text{track jet}}$	The ratio of the lepton $p_T$ and the track jet $p_T$
$\Delta R(\text{lepton, track jet})$	$\Delta R$ between the lepton and the track jet axis
$p_T^{\text{VarCone30}} / p_T$	Lepton track isolation, with track collecting radius of $\Delta R < 0.3$
$E_T^{\text{TopoCone30}} / p_T$	Lepton calorimeter isolation, with topological cluster collecting radius of $\Delta R < 0.3$

Table 36: A table of the variables used in the training of `PromptLeptonIso`.

731 The output distribution of the BDT is shown in Figure A.

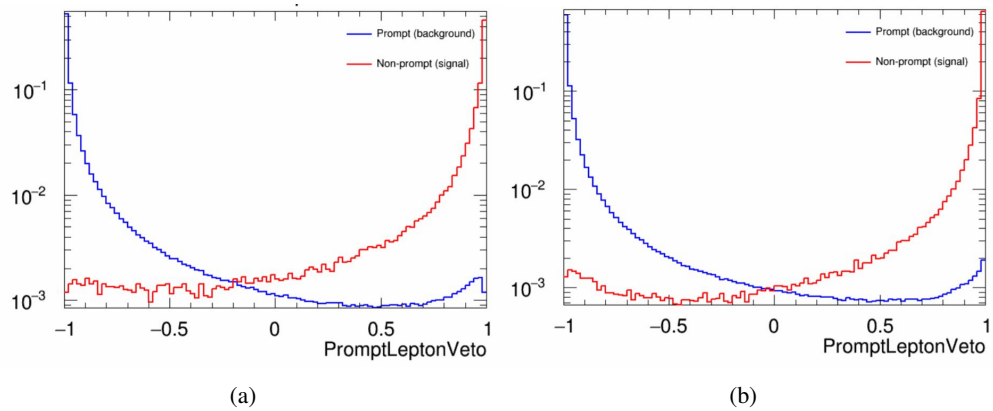


Figure A.1: Distribution of the PLV BDT discriminant for (a) electrons and (b) muons

732 The ROC curve for the BDT response, compared to the standard `FixedCutTight` WP, is shown  
 733 in figure A, which shows a clear improvement when using this alternate training.

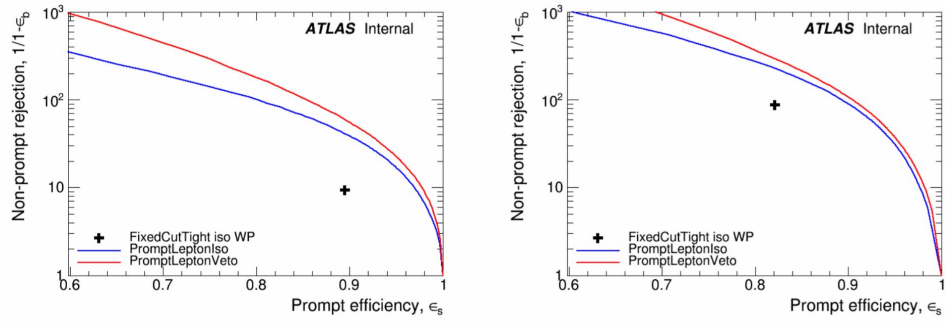


Figure A.2: ROC curves for the PLV as well as the performance of the standard FixedCutTight WP for (left) electrons and (right) muons

734 A cutoff value of -0.7 for electrons and -0.5 for muons are chosen as the WPs for this MVA, based  
 735 on an optimisation of  $S/\sqrt{B}$  performed in the preselection regions of the  $t\bar{t}H$  – ML analysis,  
 736 which have a signature similar to that of this analysis.

737 The efficiency of the tight PromptLeptonIso working point is measured using the tag and probe  
 738 method with  $Z \rightarrow \ell^+ \ell^-$  events. Such calibration are performed by analysers from this analysis in  
 739 communication with the Egamma and Muon combined performance groups. The scale factor are  
 740 approximately 0.92 for  $10 < p_T < 15$  GeV, and averaging at 0.98 to 0.99 for higher  $p_T$  leptons.  
 741 An extra systematic is applied to muons within  $\Delta R < 0.6$  of a calorimeter jet, since there is a  
 742 strong dependence on the scale factor due to the presence of these jets. For electrons, the dominant  
 743 systematics is coming from pile-up dependence. Overall the systematics are a maximum of 3% at  
 744 low  $p_T$  and decreasing at a function of  $p_T$ .

## 745 **B Machine Learning Models**

746 The following section provides details of the various MVAs as well as a few studies performed in  
 747 support of this analysis, exploring alternate decisions and strategies.

### 748 **B.1 Higgs Reconstruction Model Details**

#### 749 **B.1.1 b-jet Identification Features - 2ISS**

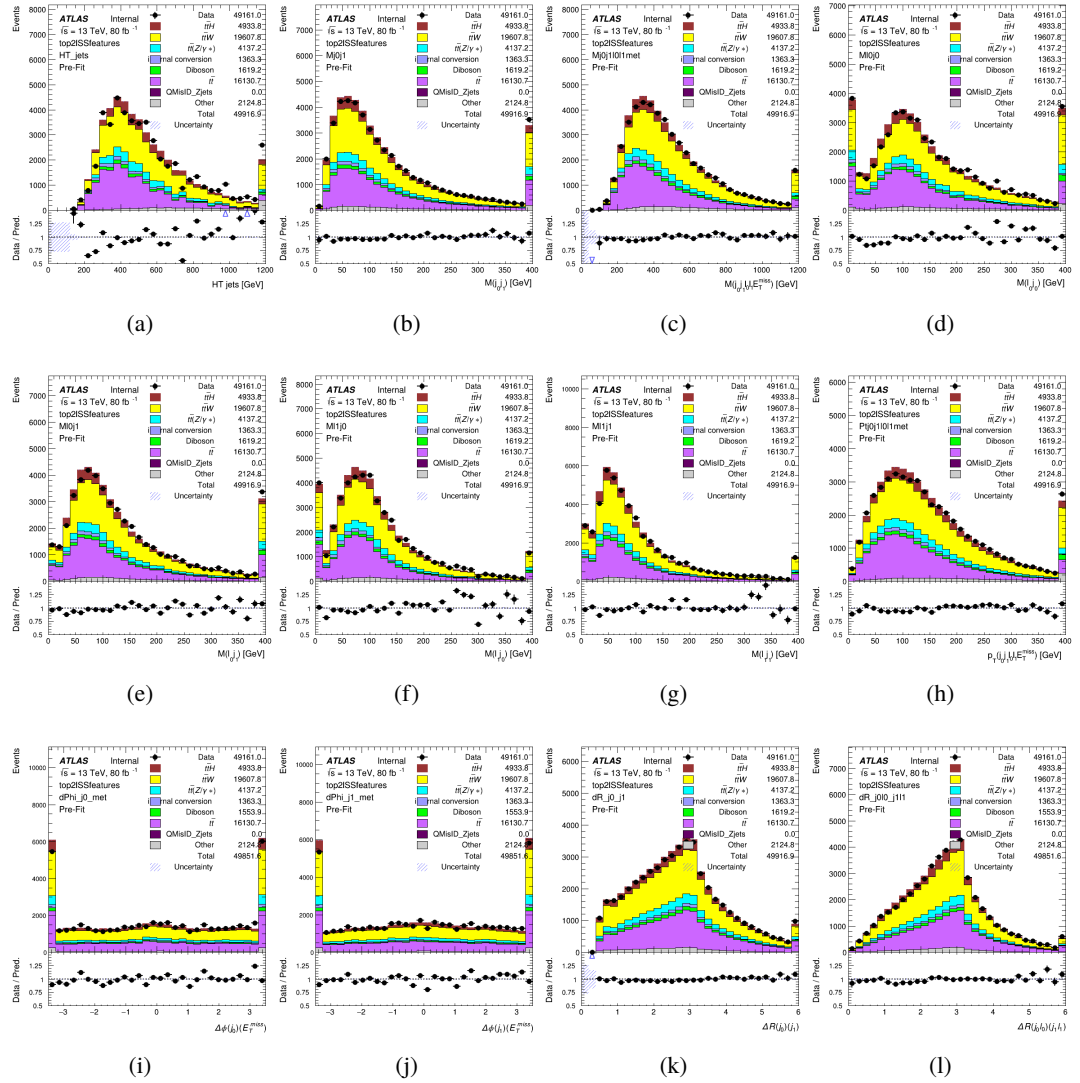


Figure B.1: Input features for top2lSS

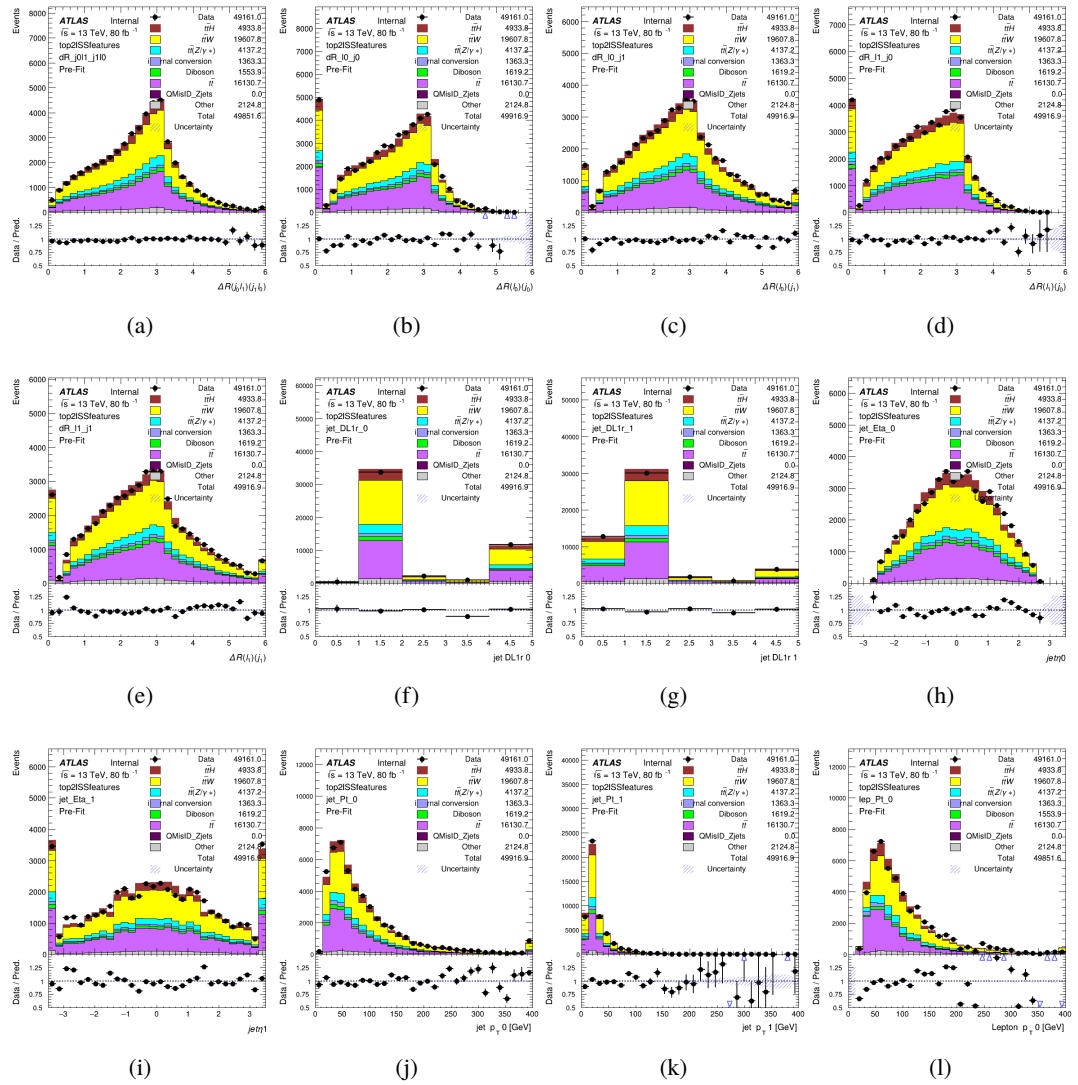


Figure B.2: Input features for top2lSS

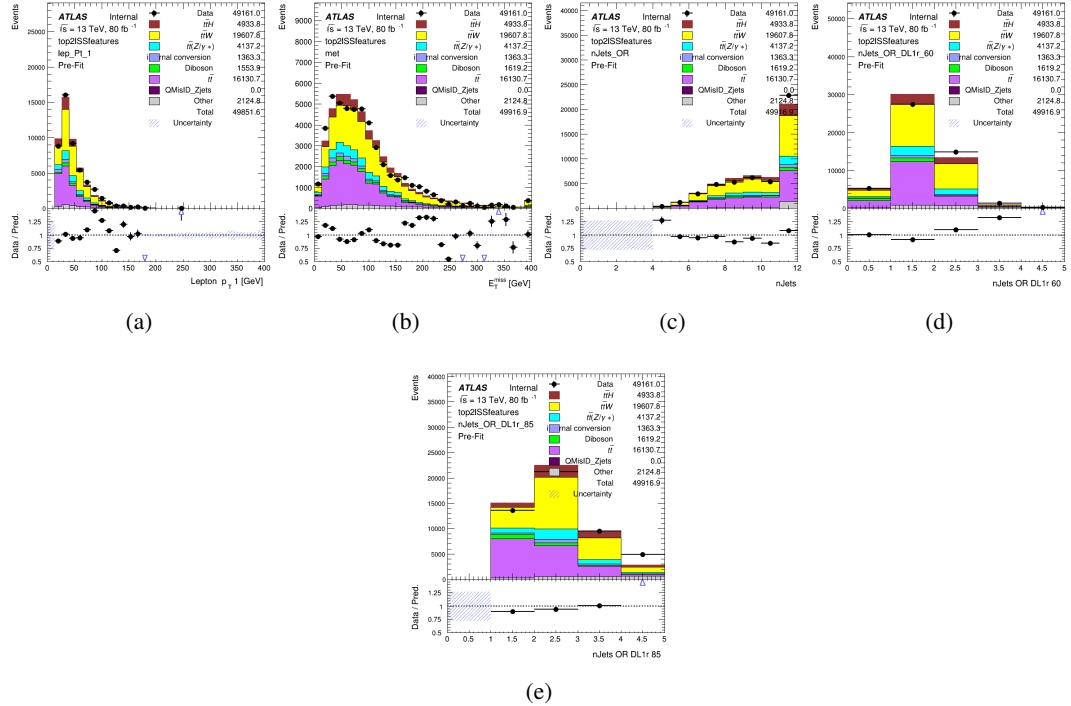


Figure B.3: Input features for top2ISS

750 **B.1.2 b-jet Identification Features - 3l**

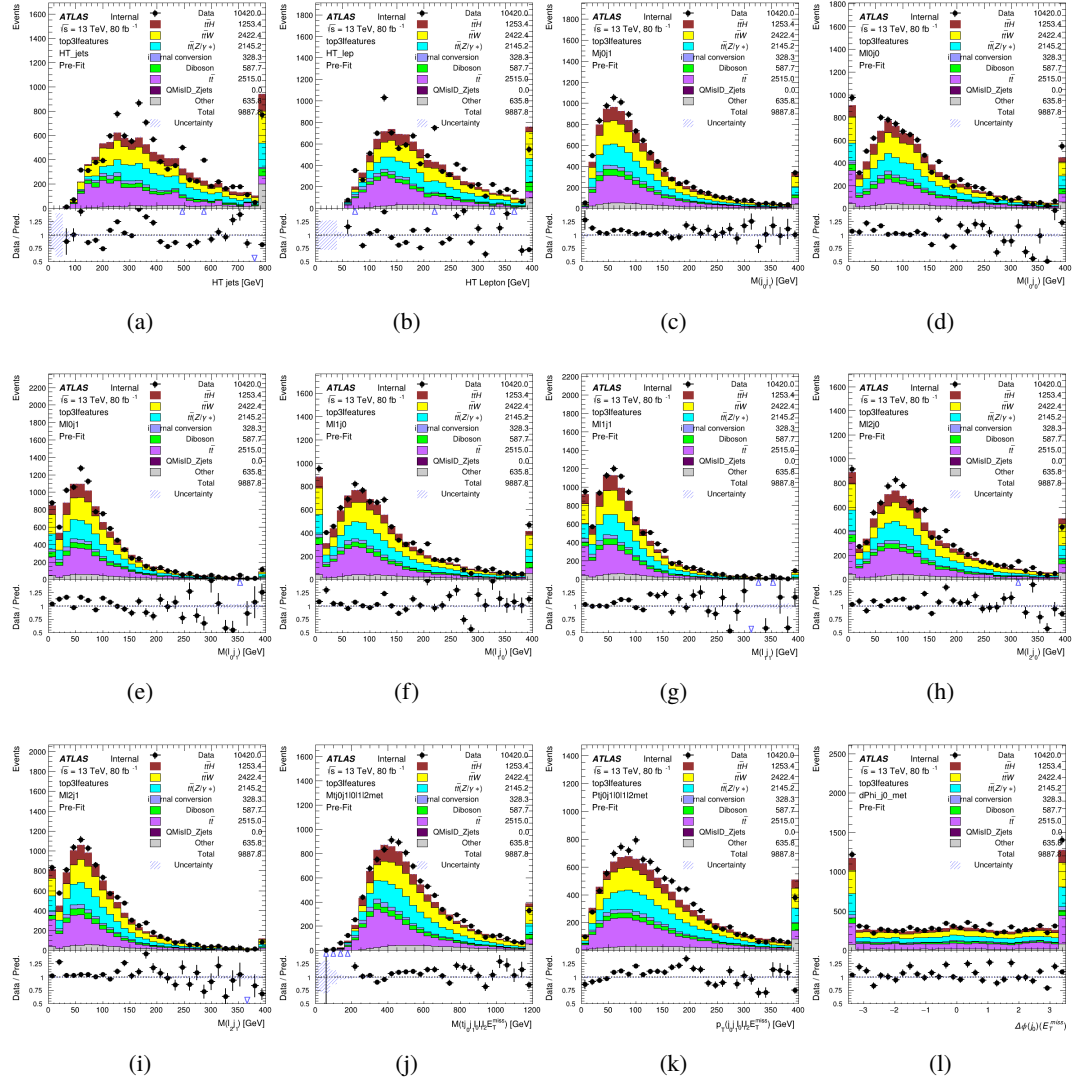


Figure B.4: Input features for top31

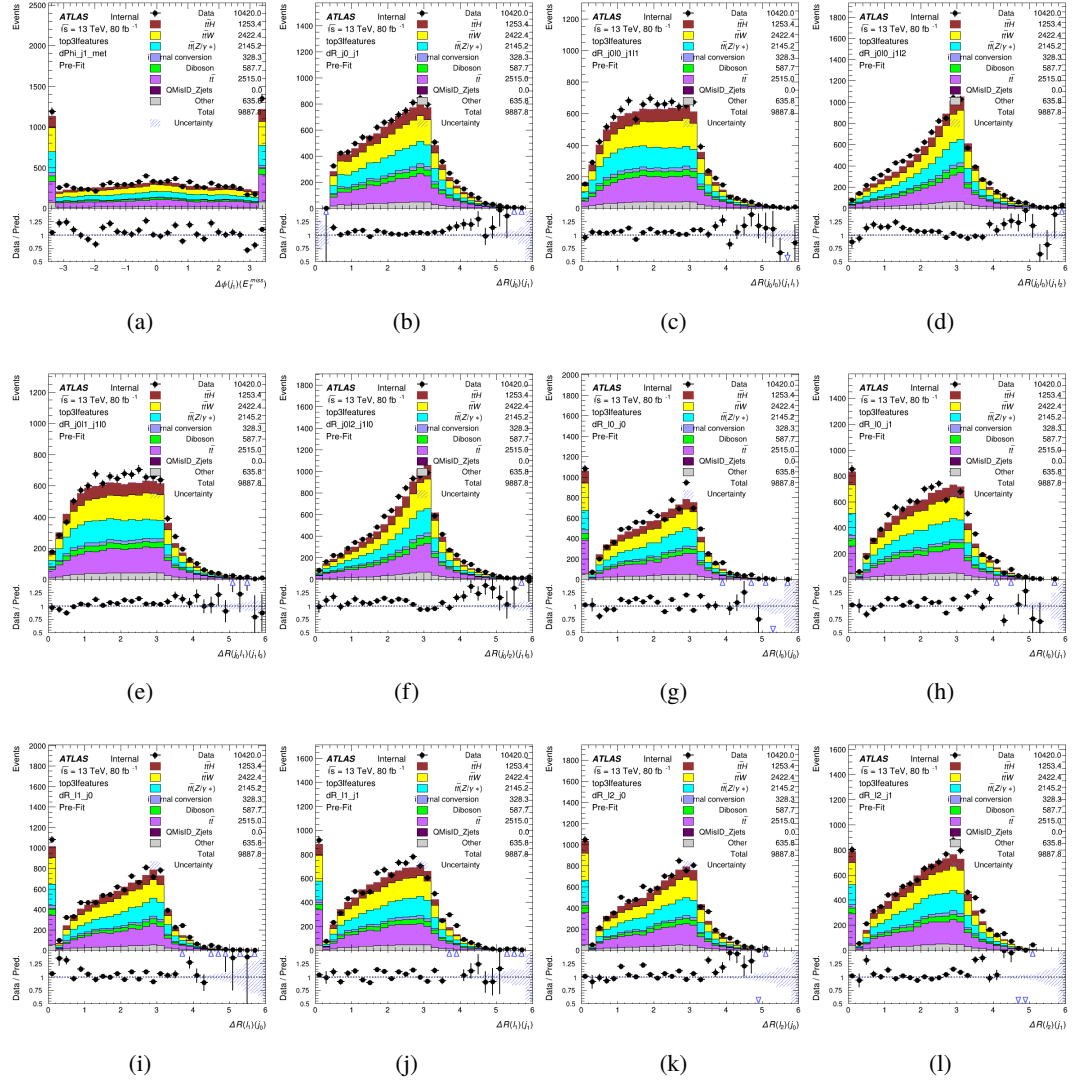


Figure B.5: Input features for top31

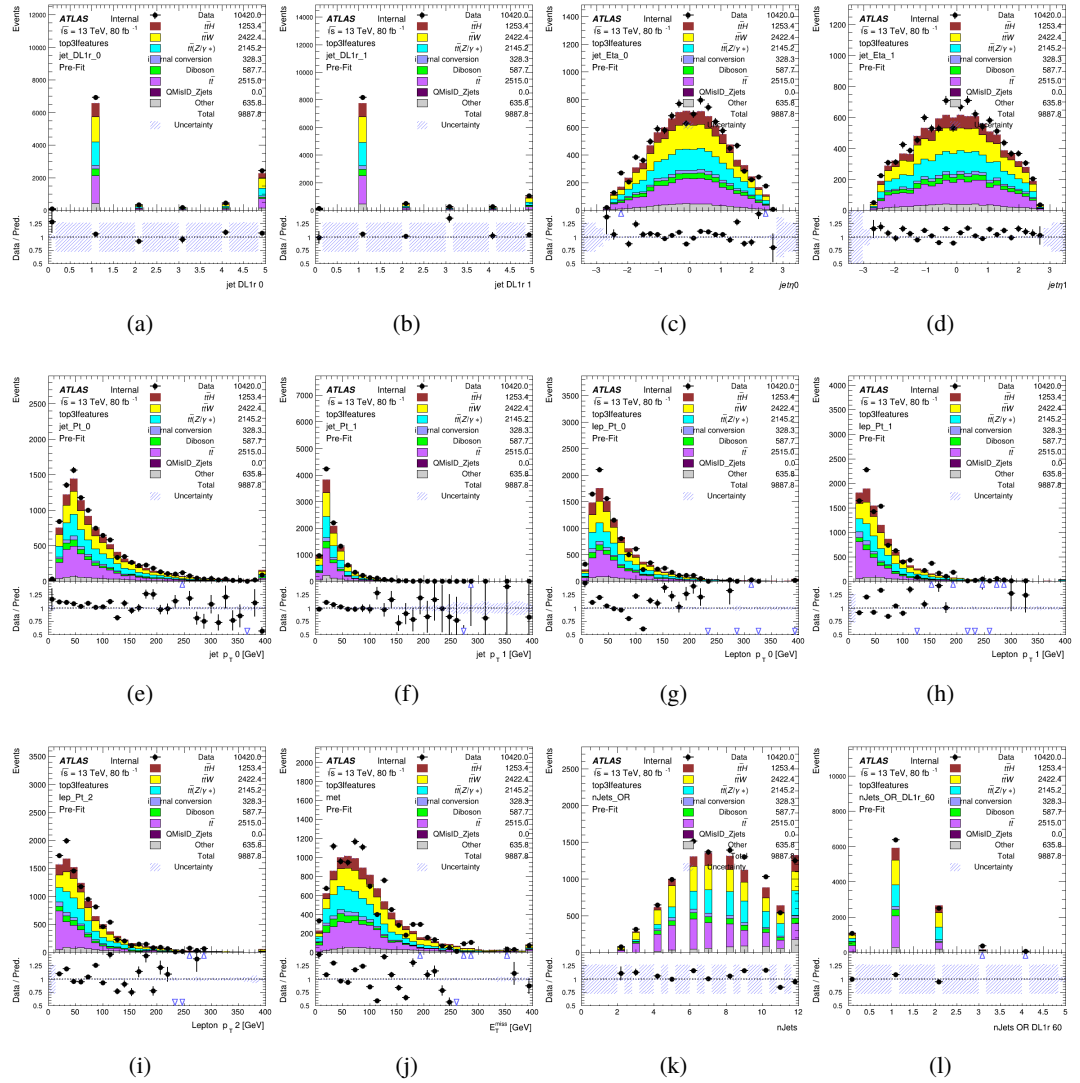
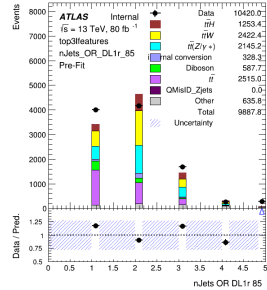


Figure B.6: Input features for top31



(a)

Figure B.7: Input features for top3l

751 **B.1.3 Higgs Reconstruction Features - 2lSS**

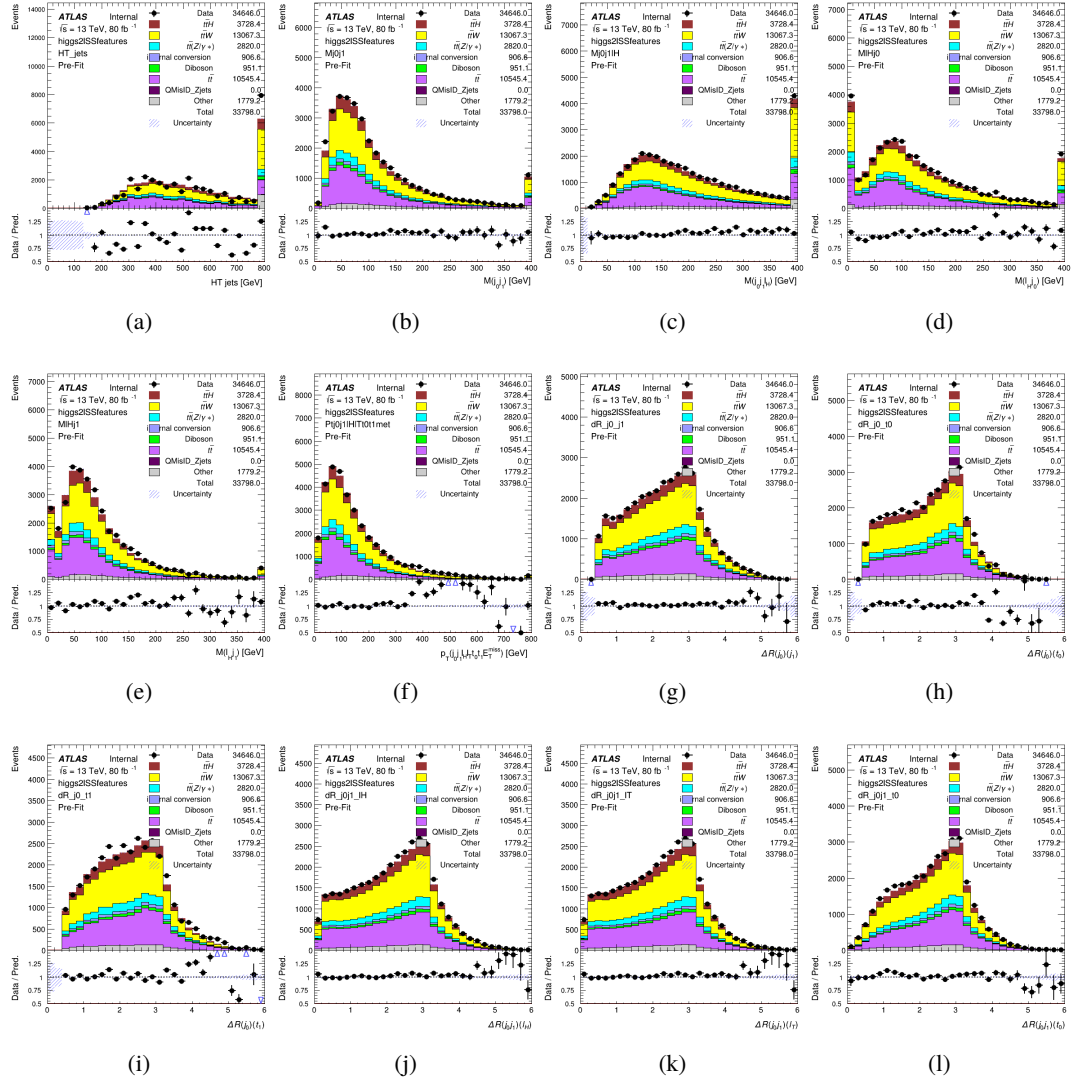


Figure B.8: Input features for higgs2ISST

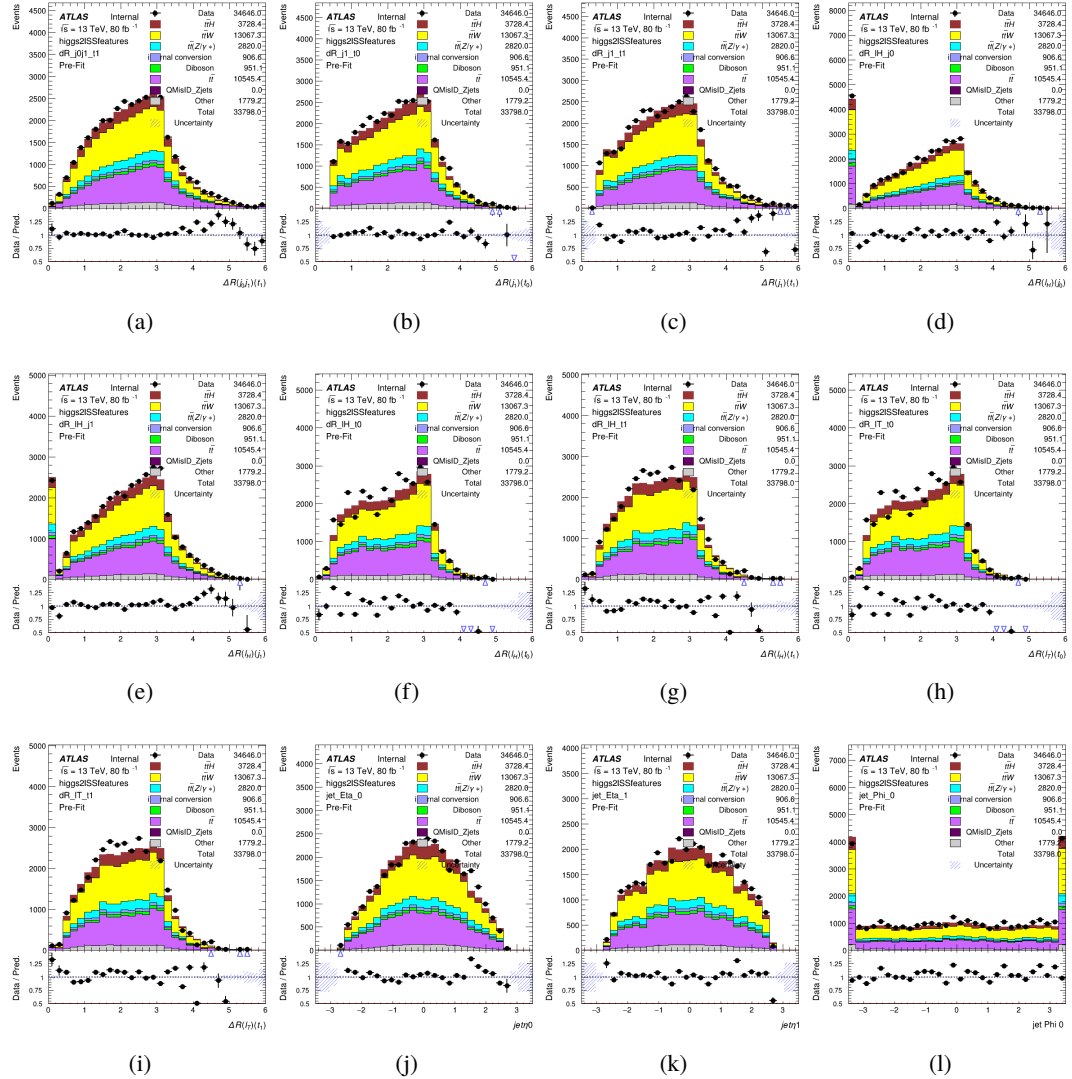


Figure B.9: Input features for higgs2lSS

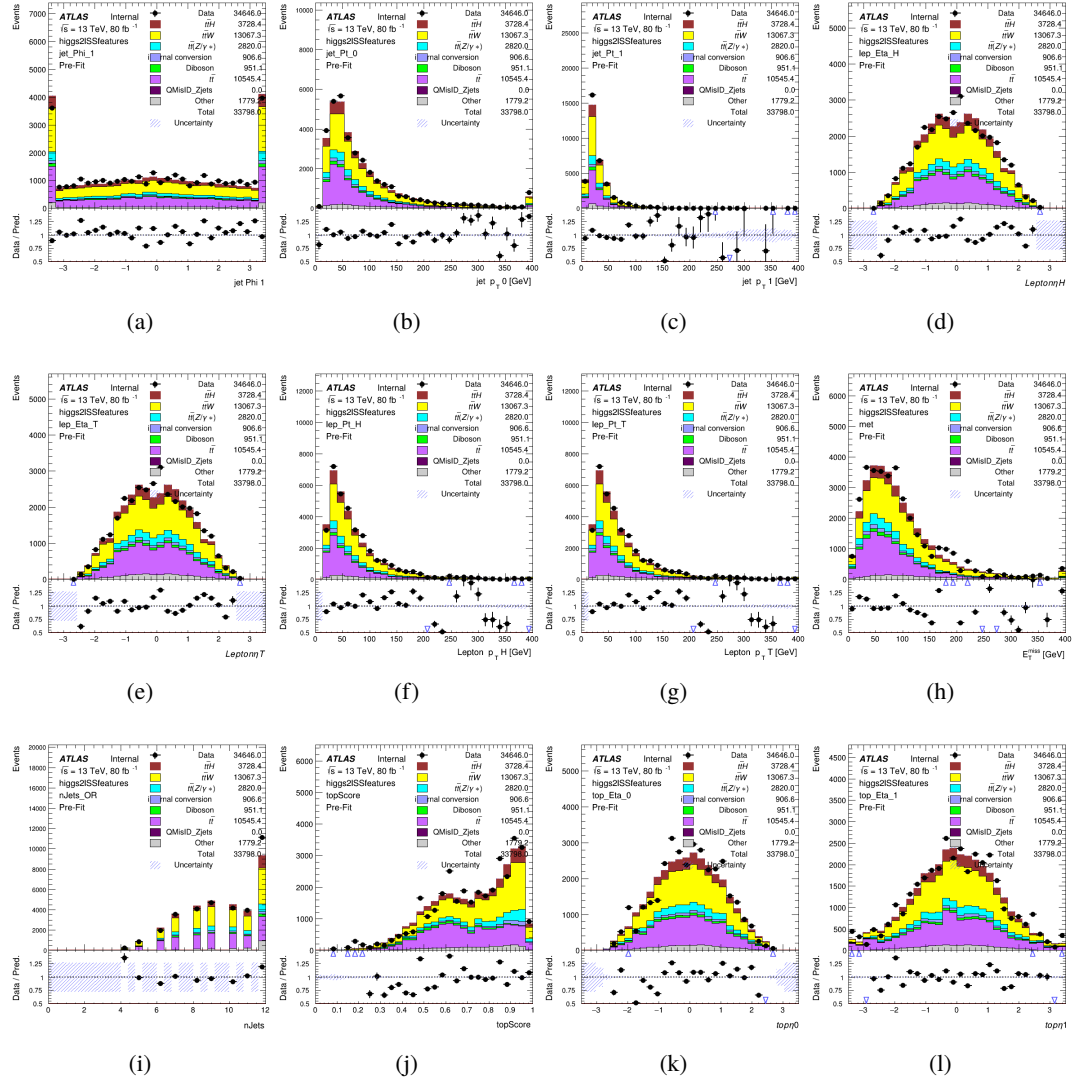


Figure B.10: Input features for higgs2lSS

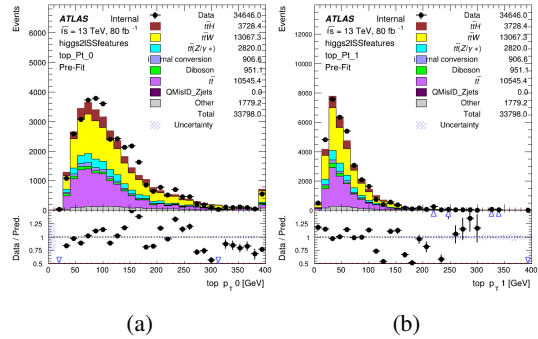


Figure B.11: Input features for higgs2lSS

752 **B.1.4 Higgs Reconstruction Features - 3lS**

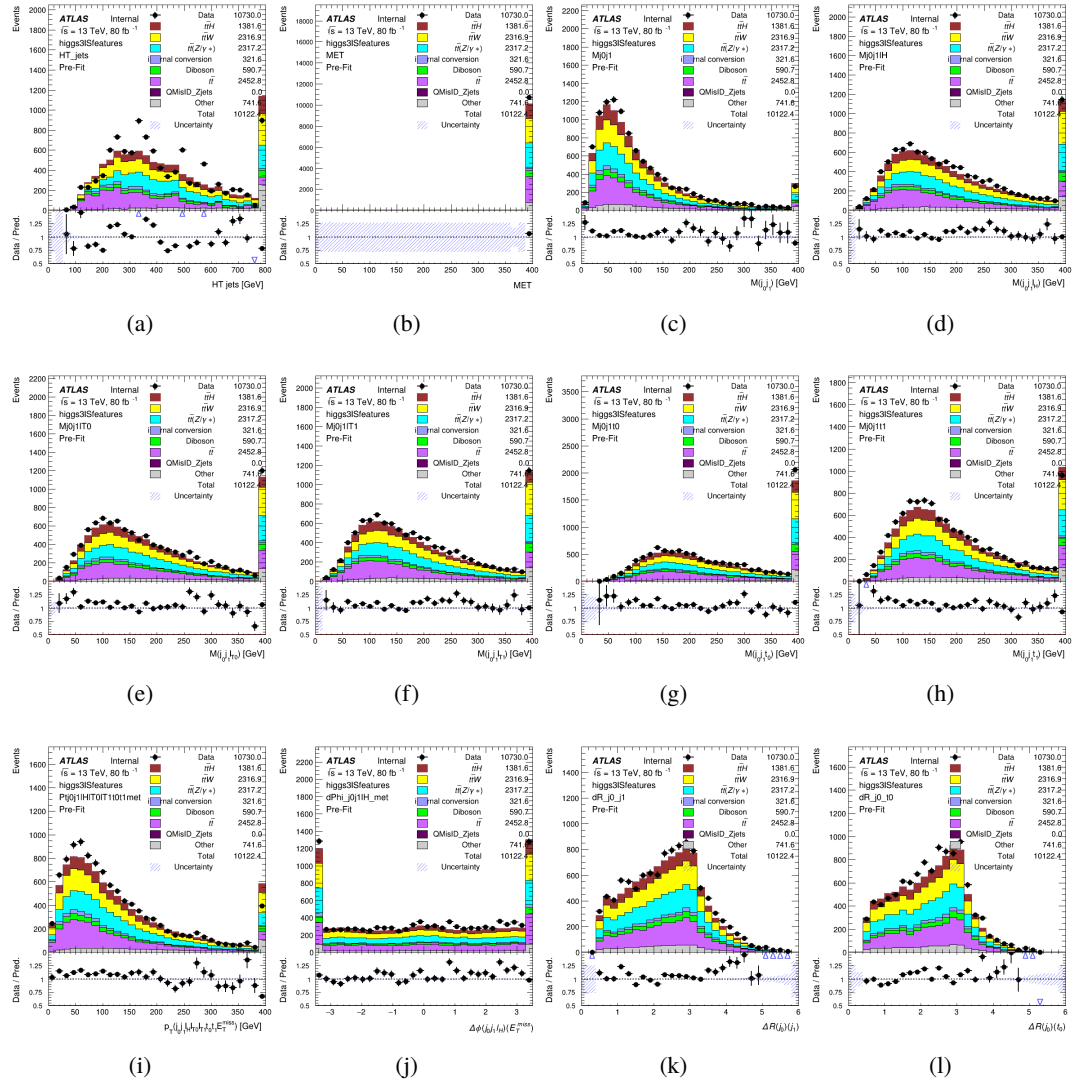


Figure B.12: Input features for higgs3IS

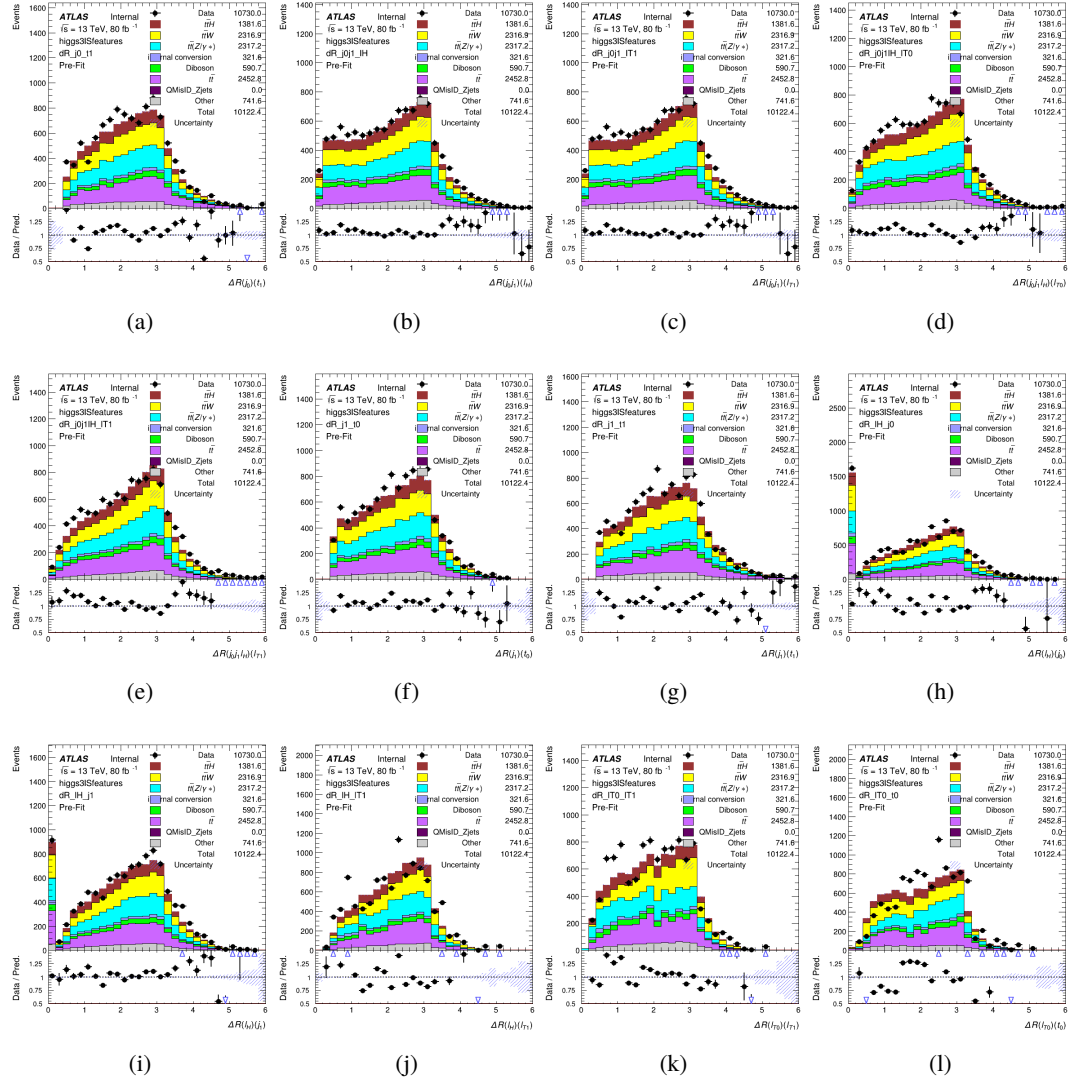


Figure B.13: Input features for higgs3lS

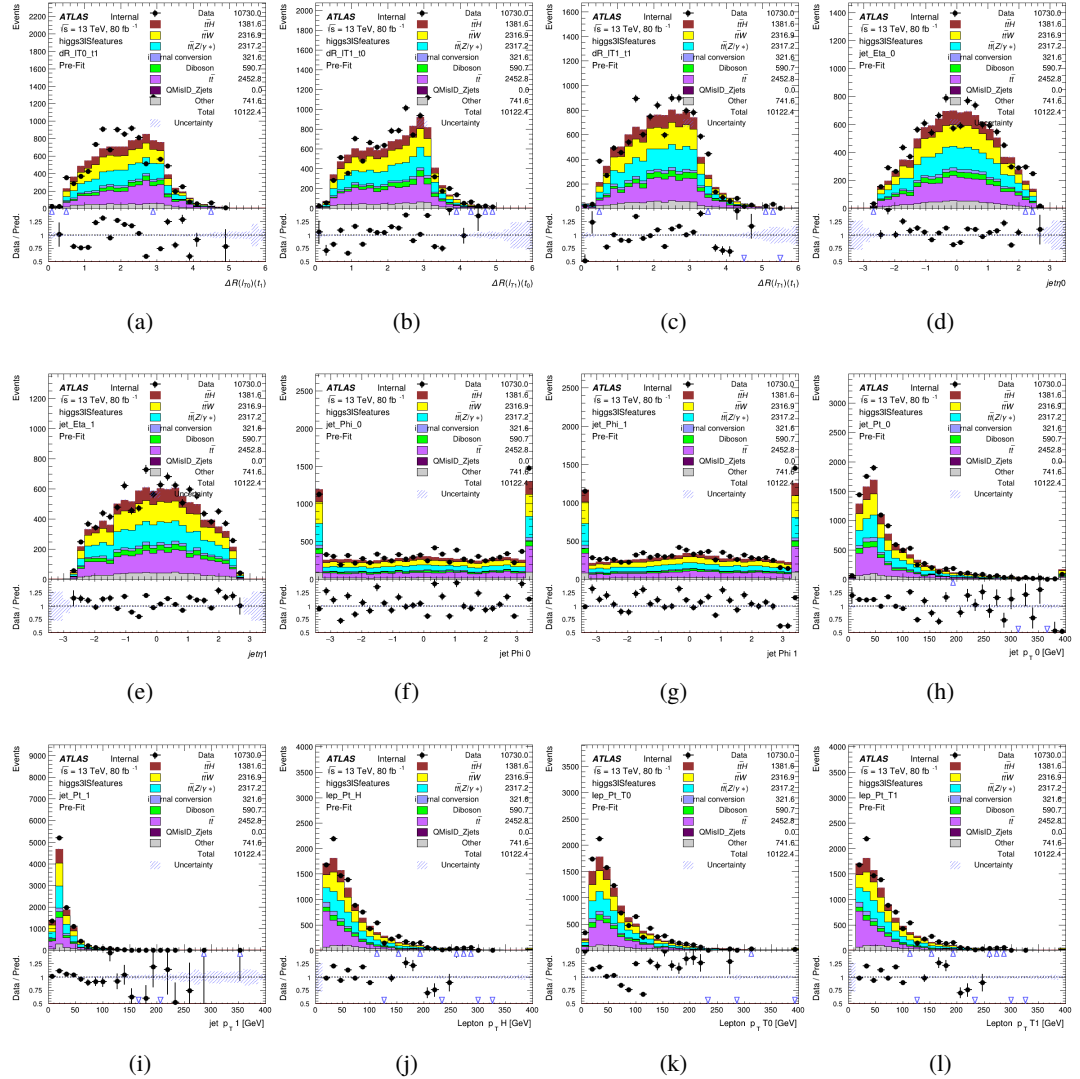


Figure B.14: Input features for higgs3IS

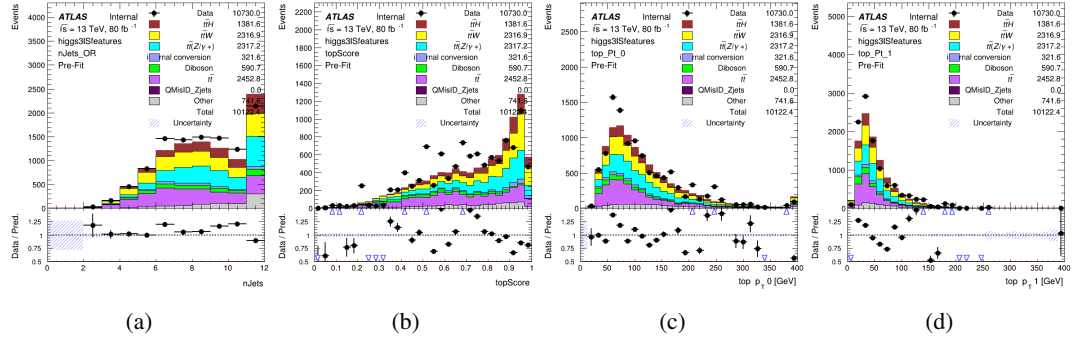


Figure B.15: Input features for higgs3IS

753 **B.1.5 Higgs Reconstruction Features - 3lF**

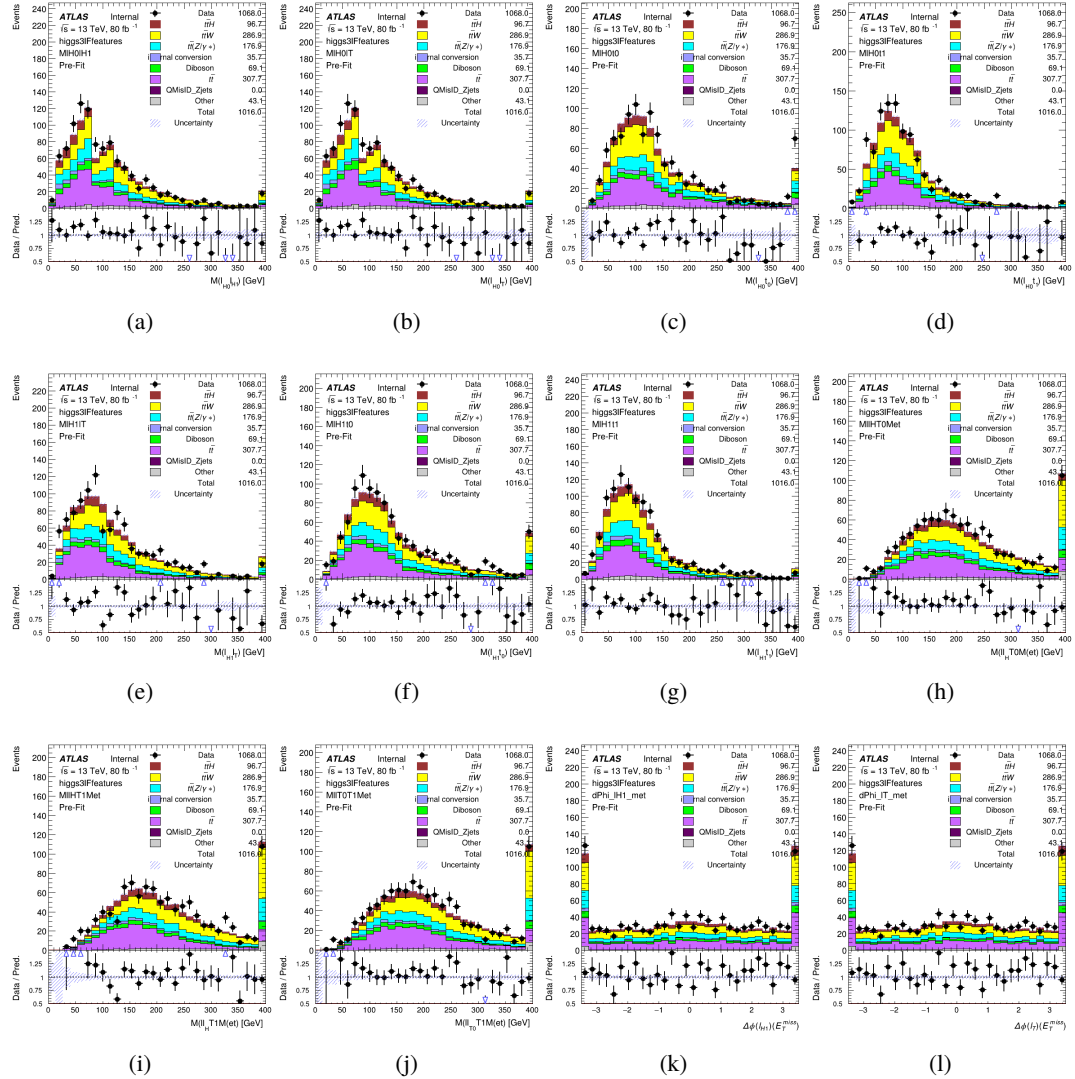


Figure B.16: Input features for higgs3IF

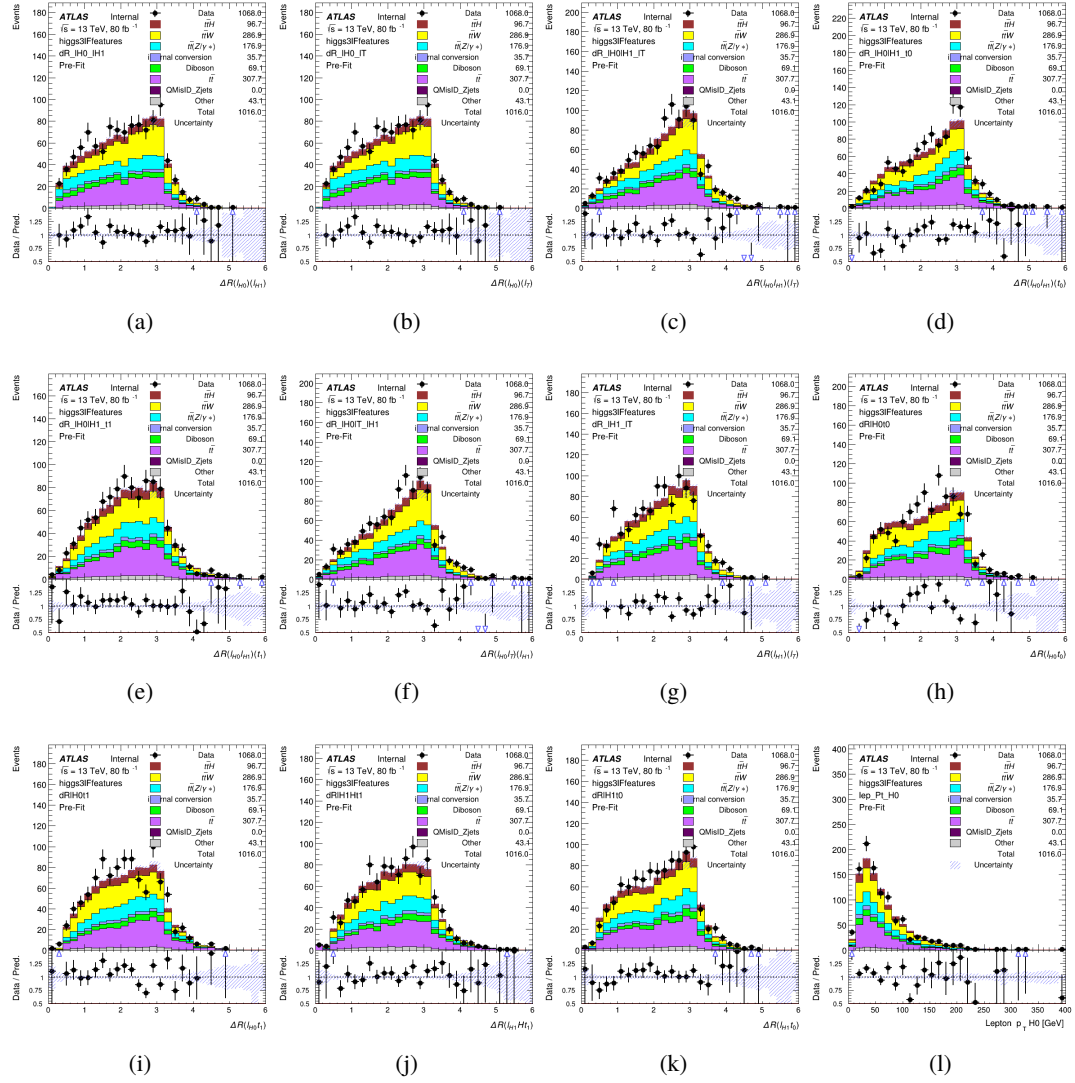


Figure B.17: Input features for higgs3IF

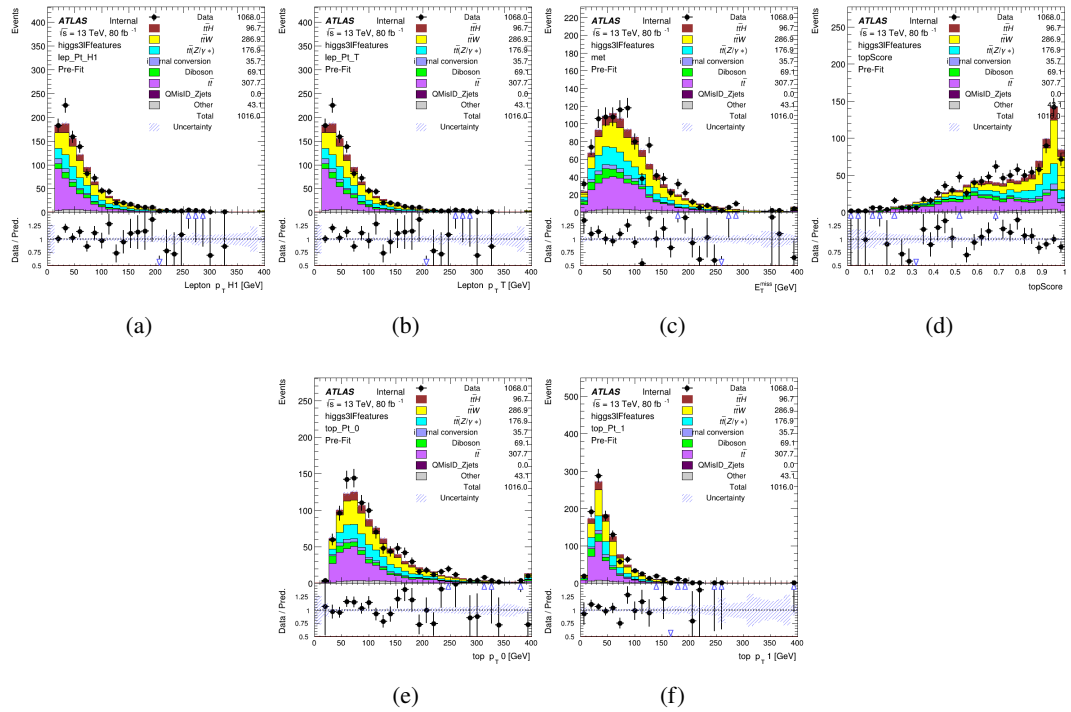


Figure B.18: Input features for higgs3lF

754 **B.2 Background Rejection MVA Details**

755 **B.2.1 Background Rejection MVA Features - 2lSS**

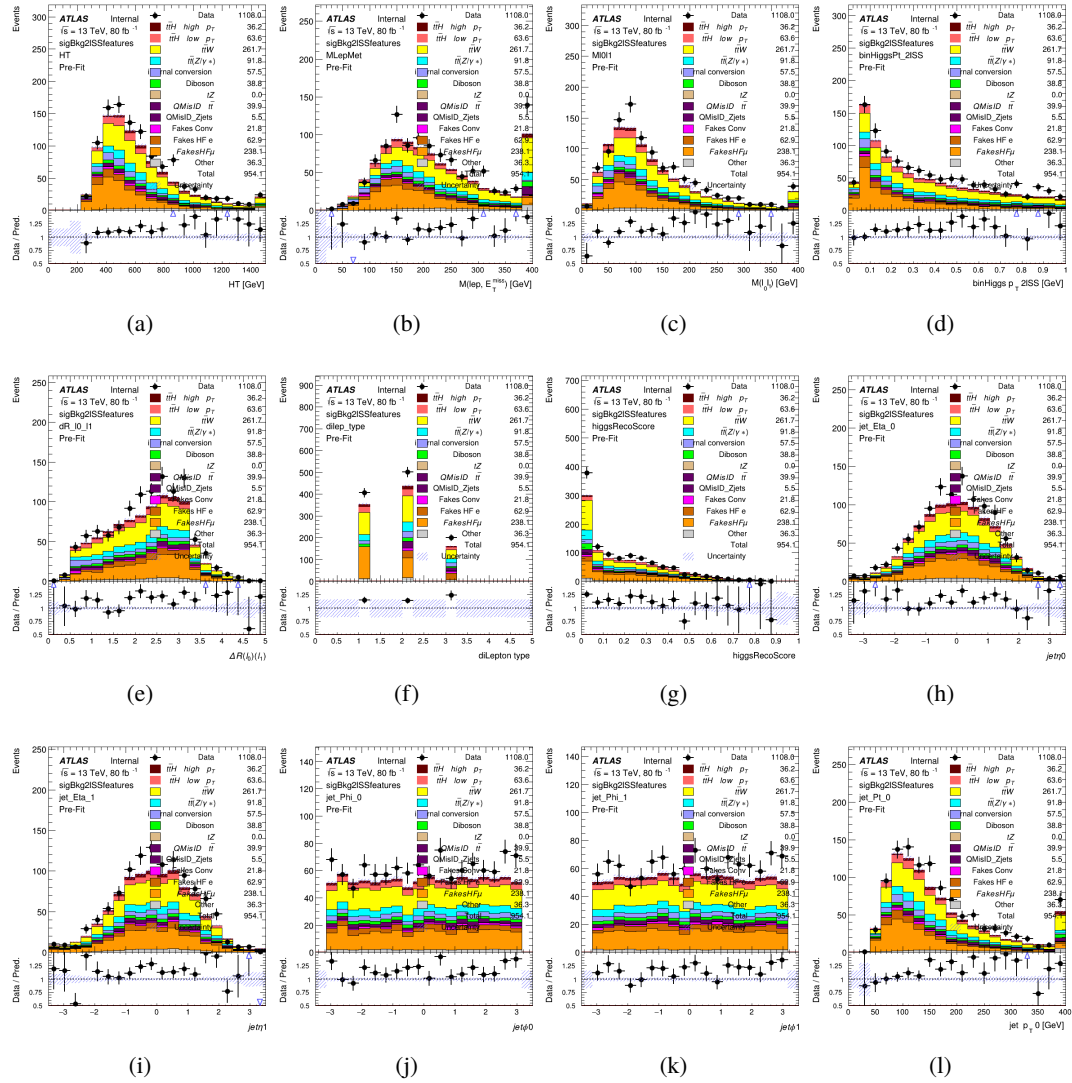


Figure B.19: Input features for sigBkg2ISS

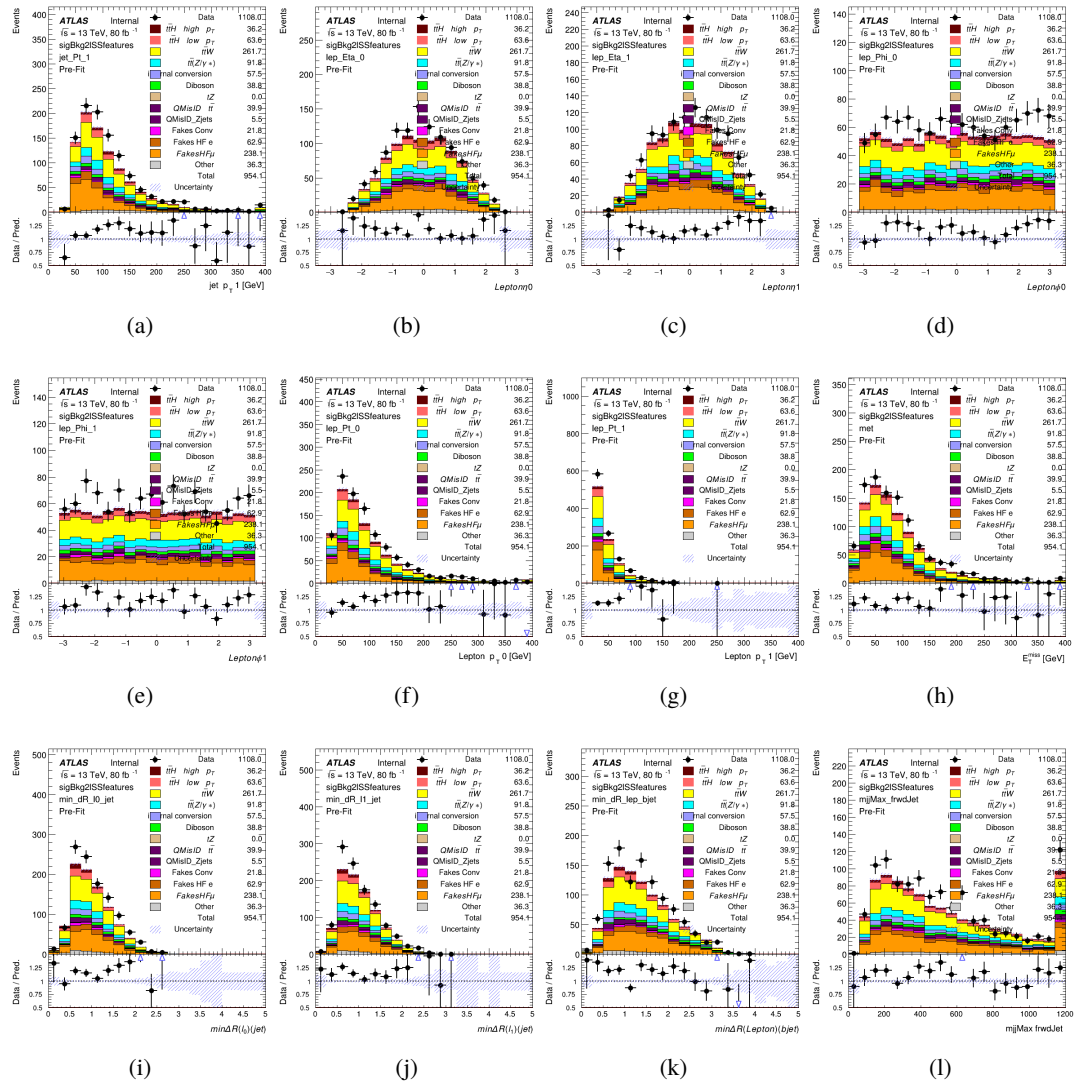


Figure B.20: Input features for sigBkg2lSS

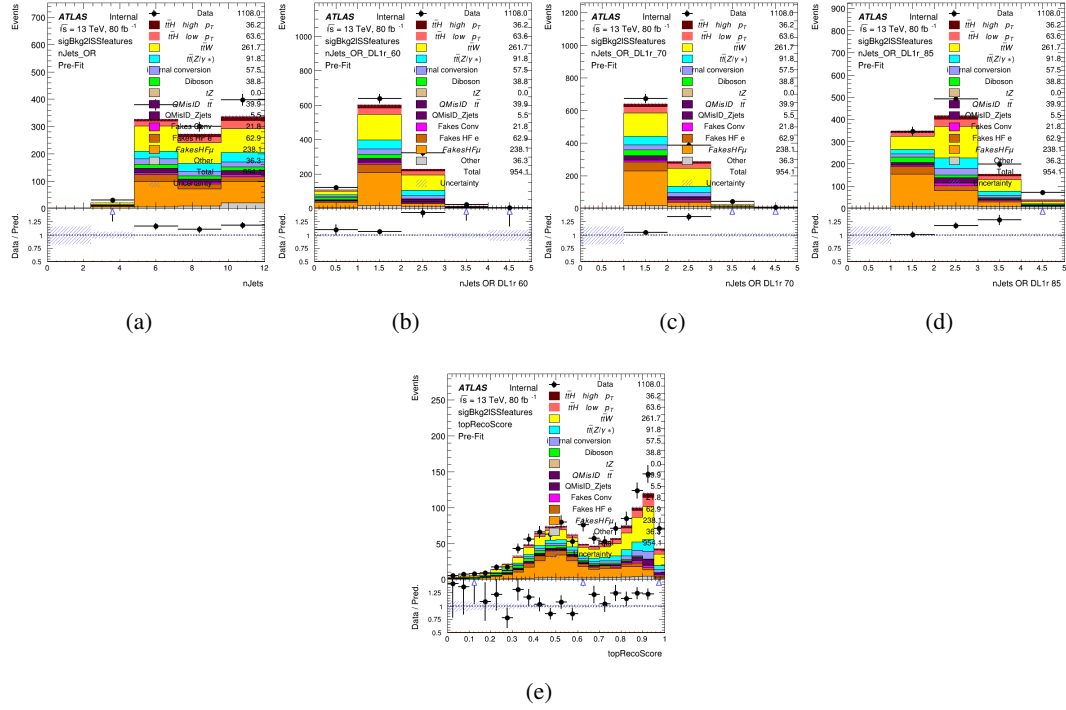


Figure B.21: Input features for sigBkg2lSS

756 **B.2.2 Background Rejection MVA Features - 3l**

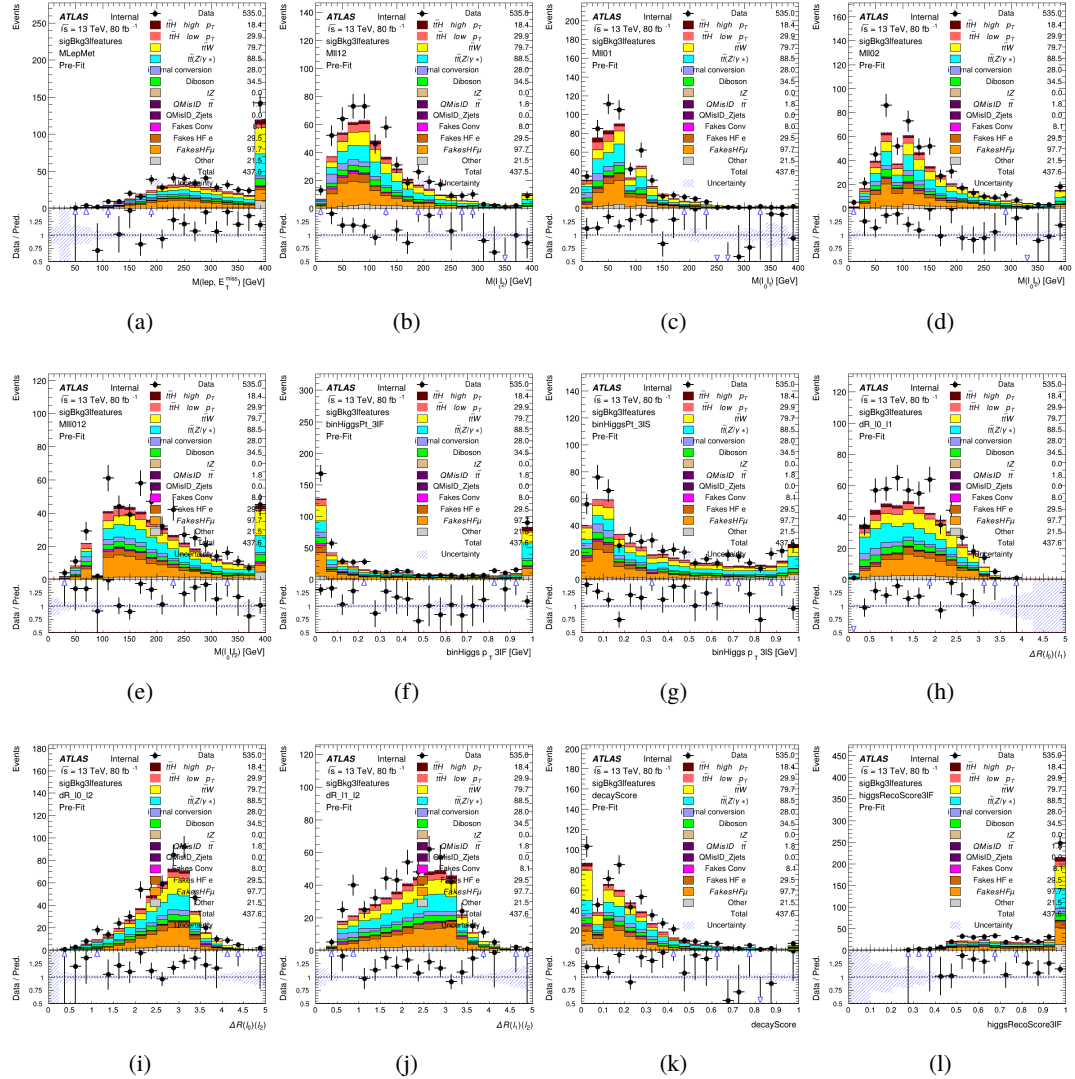


Figure B.22: Input features for sigBkg3l

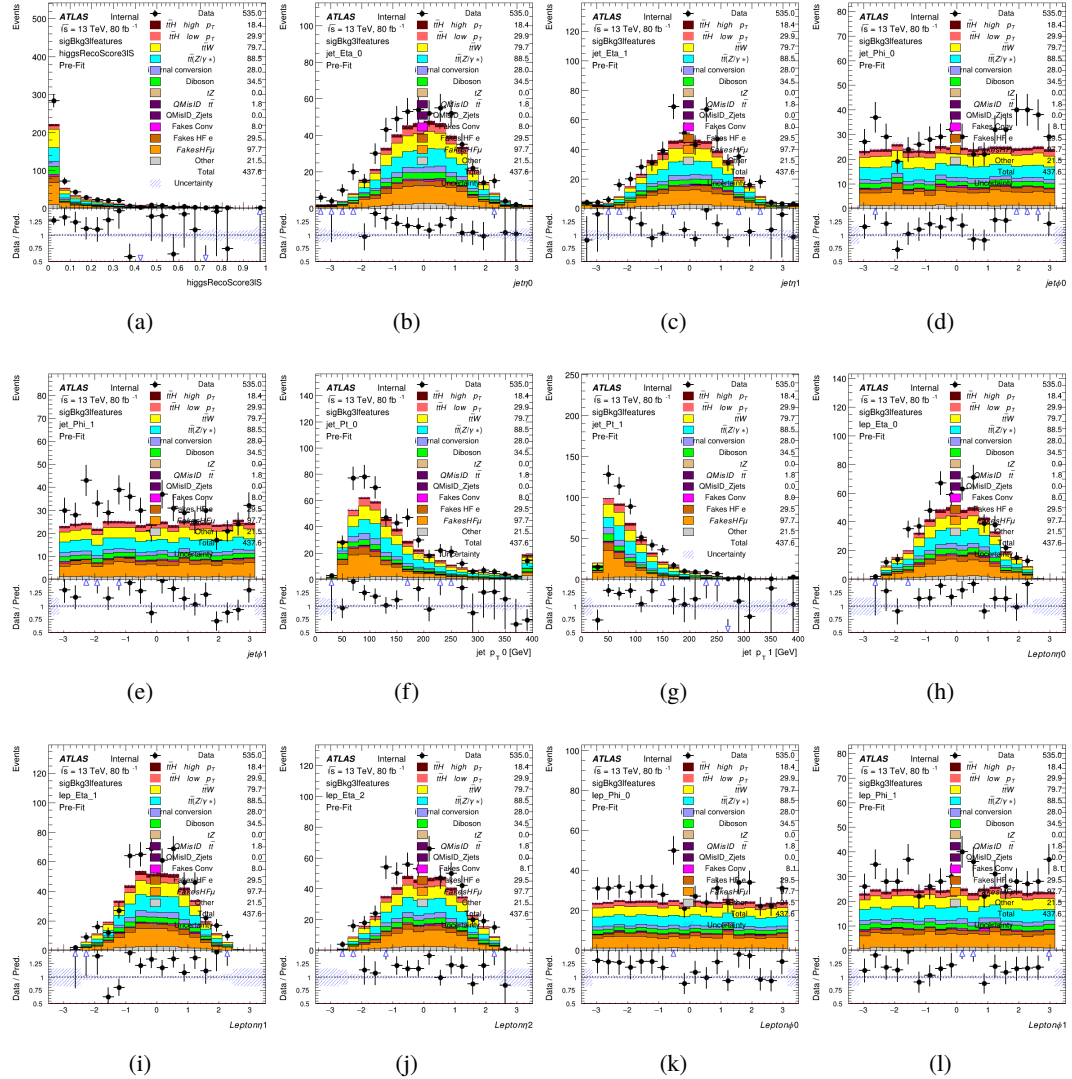
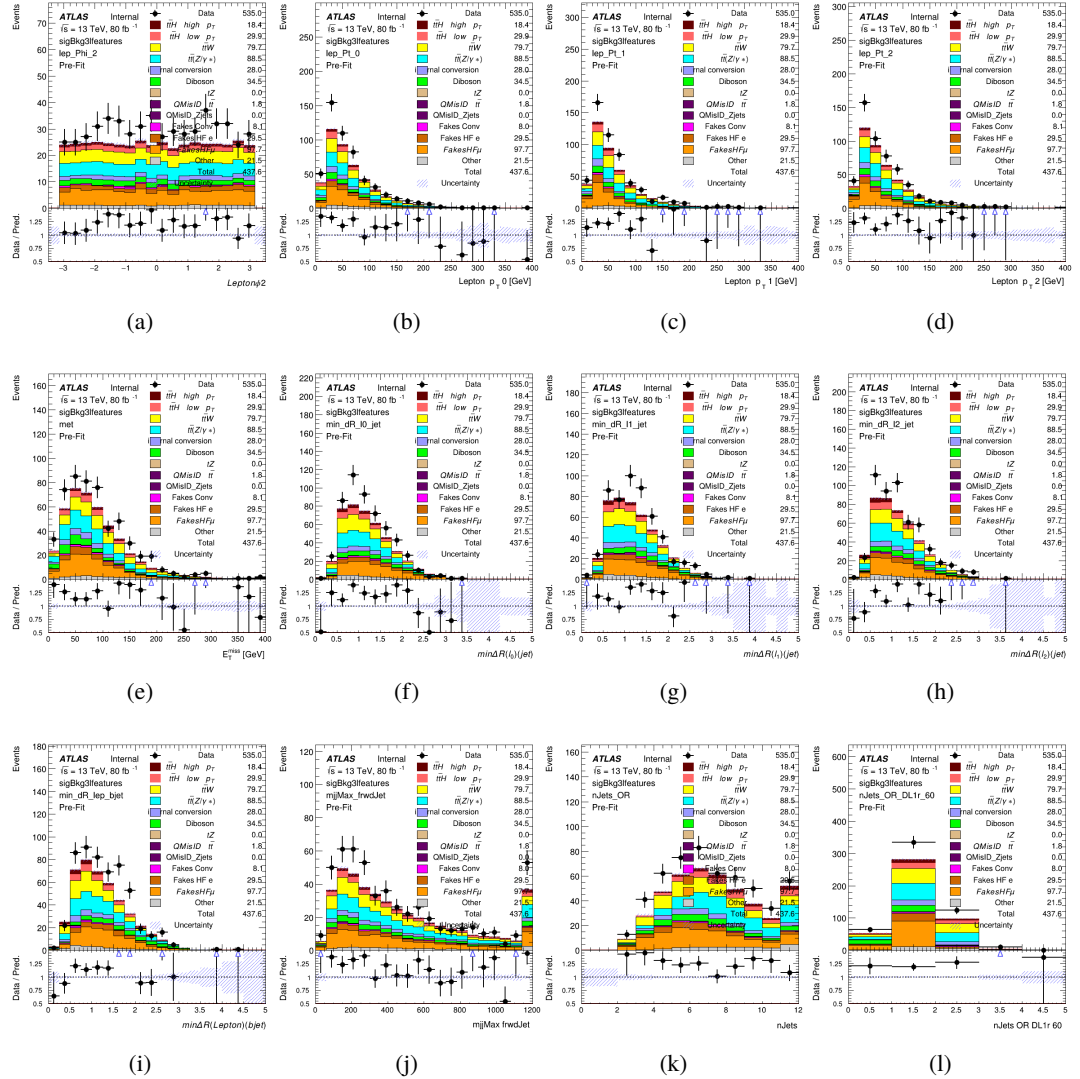
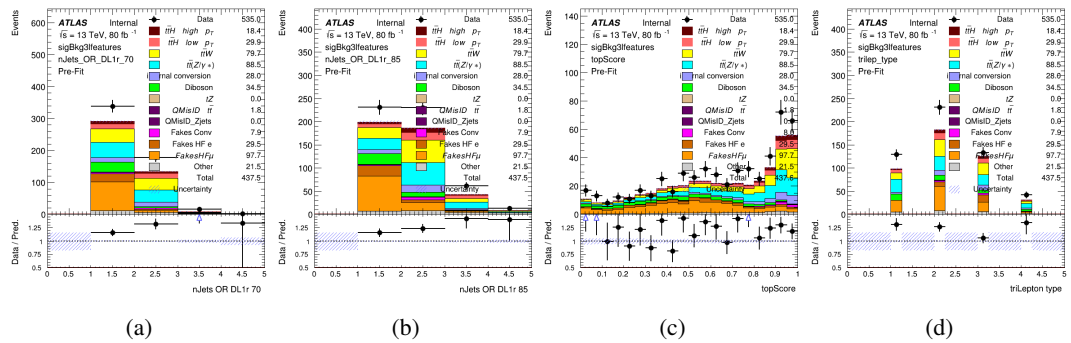


Figure B.23: Input features for sigBkg3l

Figure B.24: Input features for `sigBkg3l`

Figure B.25: Input features for `sigBkg3l`

757 **B.3 Truth Level Studies**

758 Attempts to identify the decay products of the Higgs are motivated by the ability to reconstruct  
 759 the Higgs momentum based on their kinematics. In order to demonstrate that this is case, the  
 760 kinematics of reconstructed objects that are truth matched to the Higgs decay are used as inputs  
 761 to a neural network which is designed to predict the momentum of the Higgs. This is done in  
 762 the 2lSS channel, as it proves to be the most challenging for  $p_T$  reconstruction.

763 Only leptons and jets which are truth matched to the Higgs are used as inputs for the model;  
 764 events where the lepton and both jets are not reconstructed are not included. The model uses the  
 765 same feature set and network architecture as the  $p_T$  prediction model used in the main analysis, as  
 766 described in Section 5.5.1.

767 The results of the model are summarized below:

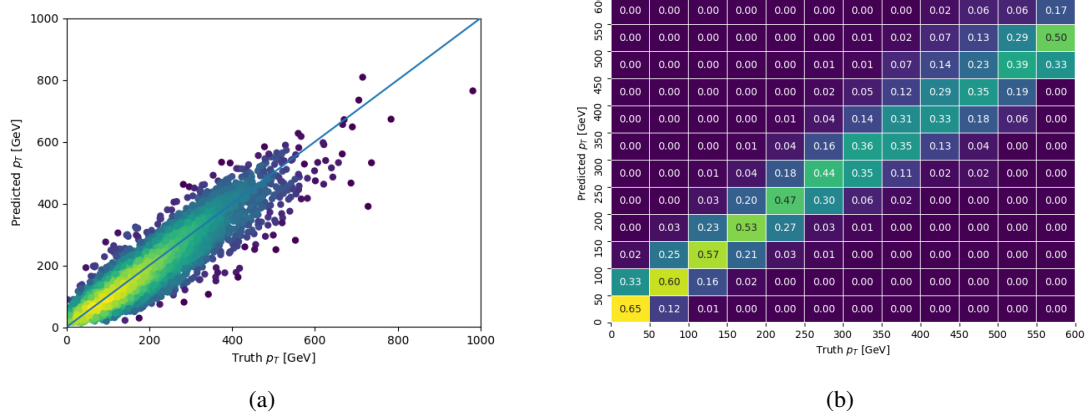


Figure B.26: The regressed Higgs momentum spectrum as a function of the truth  $p_T$  for 2lSS  $t\bar{t}H$  events  
 in (a) a scatterplot, where the color of each point represents the log of the point density, based on Gaussian  
 Kernel Density Estimation, and (b) a histogram where each column has been normalized to one.

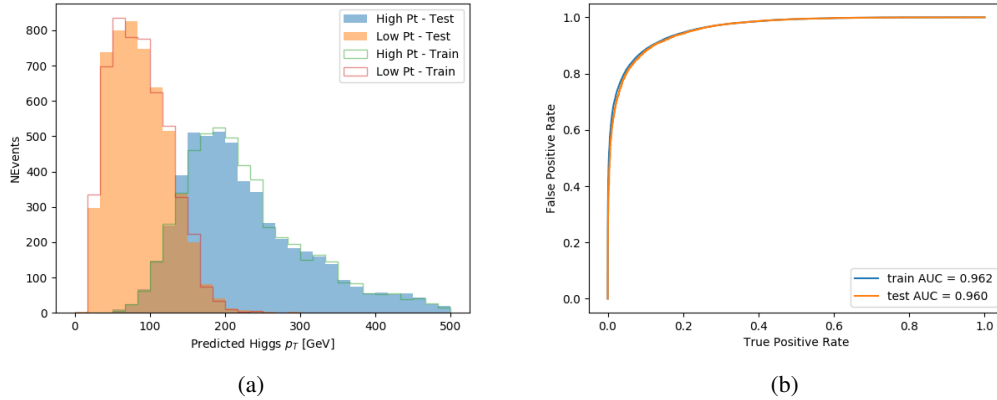


Figure B.27: (a) shows the reconstructed Higgs  $p_T$  for 2lSS events with truth  $p_T > 150$  GeV and  $< 150$  GeV, while (b) shows the ROC curve for those two sets of events.

768 Based on the performance of the model, as shown Figures B.26 and B.27, the Higgs momentum  
 769 can be reconstructed with fairly high precision when its decay products are correctly identified.

#### 770 **B.4 Alternate b-jet Identification Algorithm**

771 The nominal analysis reconstructs the b-jets by considering different combinations of jets, and  
 772 asking a neural network to determine whether each combination consists of b-jets from top quark  
 773 decays. An alternate approach would be to give the neural network about all of the jets in an event  
 774 at once, and train it to select which two are most likely to be the b-jets from top decay. It was  
 775 hypothesized that this could perform better than considering each combination independently, as  
 776 the neural network could consider the event as a whole. While this is not found to be the case,  
 777 these studies are documented here as a point of interest and comparison.

778 For these studies, the kinematics of the 10 highest  $p_T$  jets in each event are used for training. This  
 779 includes the vast majority of truth b-jets. Specifically the  $p_T$ ,  $\eta$ ,  $\phi$ ,  $E$ , and DL1r score of each jet  
 780 are used. For events with fewer than 10 jets, these values are substituted with 0. The  $p_T$ ,  $\eta$ ,  $\phi$ ,  
 781 and  $E$  of the leptons and  $E_T^{\text{miss}}$  are included as well. Categorical cross entropy is used as the loss  
 782 function.

Table 37: Accuracy of the NN in identifying b-jets from tops in 2lSS events for the alternate categorical method compared to the nominal method.

Channel	Categorical	Nominal
2lSS	70.6%	73.9%
3l	76.1%	79.8%

783 **B.5 Binary Classification of the Higgs  $p_T$**

784 A two bin fit of the Higgs momentum is used because statistics are insufficient for any finer  
 785 resolution. This means separating high and low  $p_T$  events is sufficient for this analysis. As such,  
 786 rather than attempting the reconstruct the full Higgs  $p_T$  spectrum, a binary classification approach  
 787 is explored.

788 A model is built to determine whether  $t\bar{t}H$  events include a high  $p_T$  ( $>150$  GeV) or low  $p_T$  ( $<150$   
 789 GeV) Higgs Boson. While this is now a classification model, it uses the same input features  
 790 described in section 5.5. Binary crossentropy is used as the loss function.

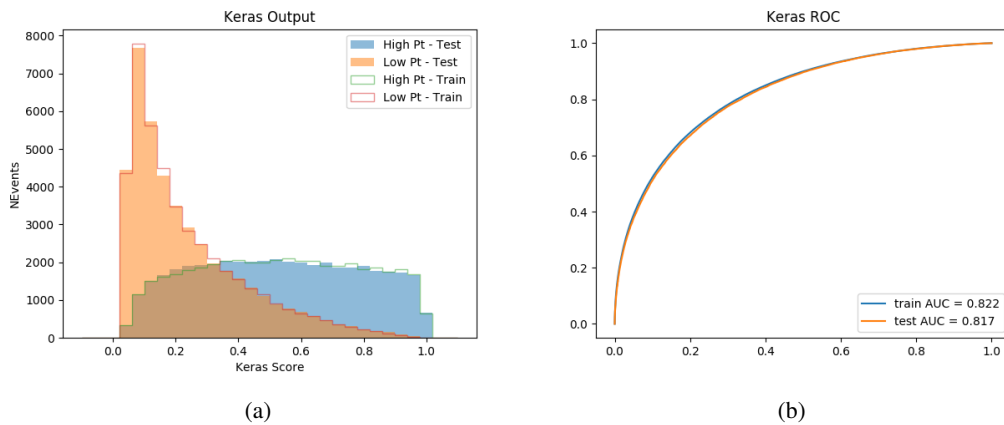


Figure B.28: Output distribution of the NN score for the binary high/low  $p_T$  separation model in the 2lSS channel.

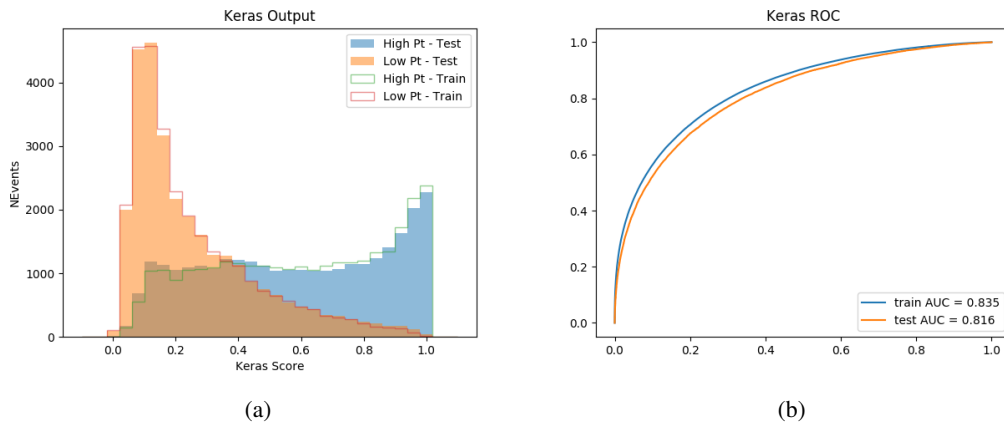


Figure B.29: Output distribution of the NN score for the binary high/low  $p_T$  separation model in the 3lS channel.

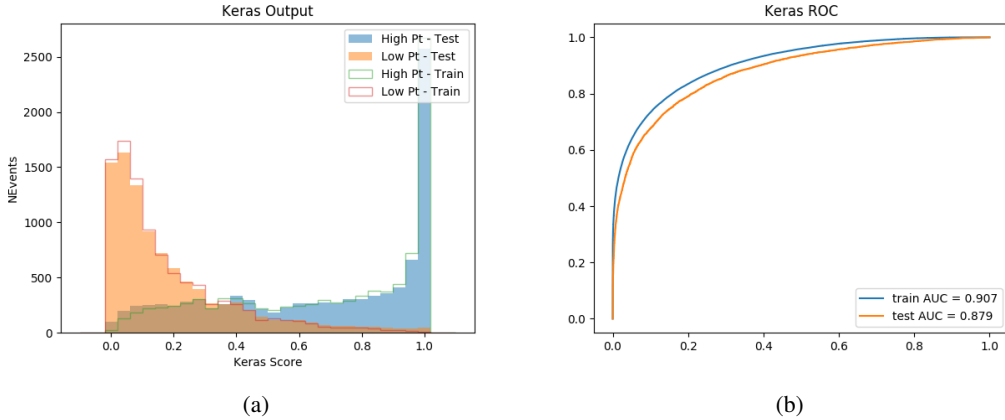


Figure B.30: Output distribution of the NN score for the binary high/low  $p_T$  separation model in the 3lS channel.

## 791 B.6 Impact of Alternative Jet Selection

792 A relatively low  $p_T$  threshold of 15 GeV is used to determine jet candidates, as the jets originating  
 793 from the Higgs decay are found to fall between 15 and 25 GeV a large fraction of the time. The  
 794 impact of different jet  $p_T$  cuts on our ability to reconstruct the Higgs  $p_T$  is explored here.

795 The models are retrained in the 2lSS channel with the same parameters as those used in the  
 796 nominal analysis, but the jet  $p_T$  threshold is altered. The performance of the Higgs  $p_T$  prediction  
 797 models for jet  $p_T$  cuts of 20 and 25 GeV are shown below.

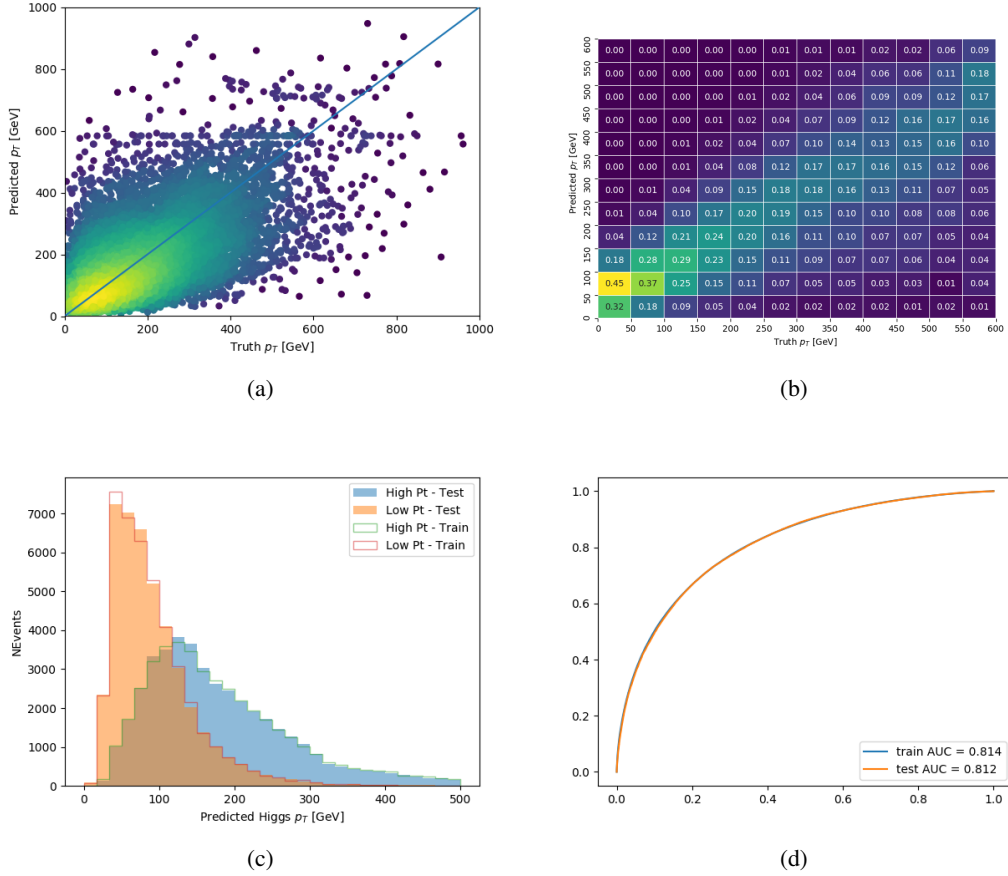
**Jet  $p_T > 20$  GeV**

Figure B.31: Output of the model designed to predict the Higgs momentum in the 2LSS channel, with the jet  $p_T$  cutoff used is raised to 20 GeV.

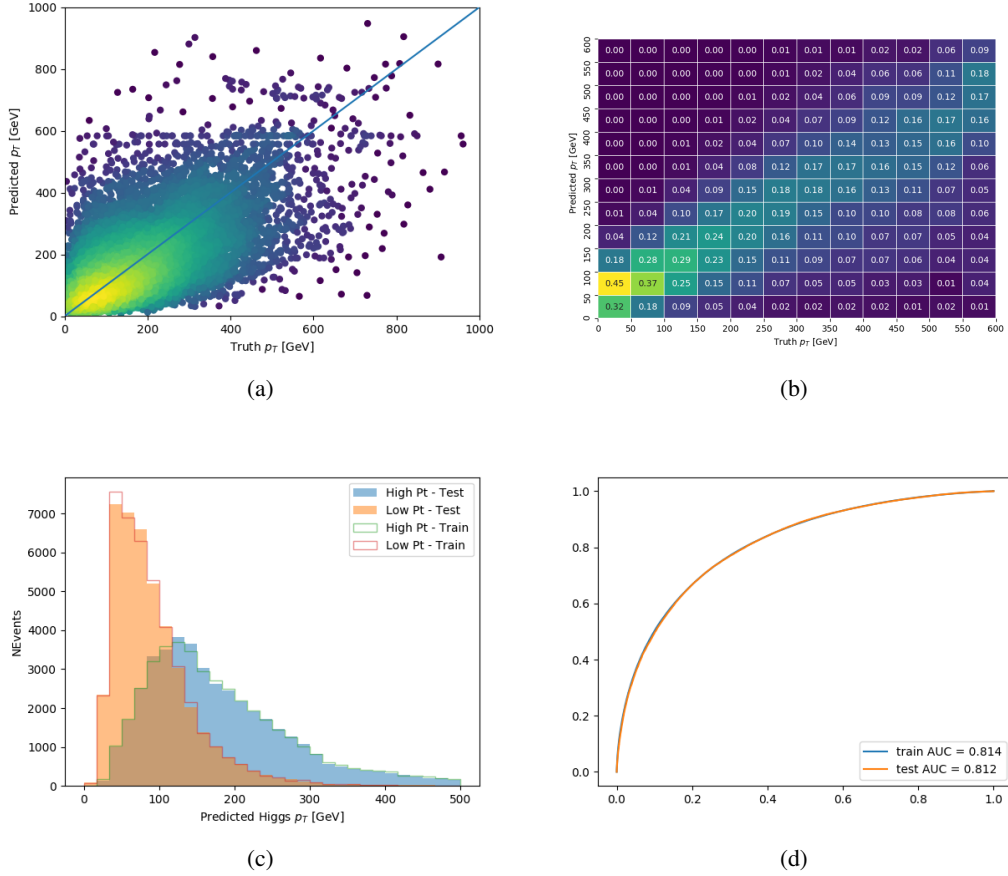
**Jet  $p_T > 25 \text{ GeV}$** 

Figure B.32: Output of the model designed to predict the Higgs momentum in the 2LSS channel, with the jet  $p_T$  cutoff used is raised to 25 GeV.